UNIVERSITY OF BIRMINGHAM

GROWTH AND PASSIVATION OF HALIDE PEROVSKITE

By

JINGWEI XIU

Supervisors: Prof. Peter Slater and Prof. Zhubing He

A thesis submitted to the University of Birmingham for the degree of

DOCTOR OF PHILOSOPHY

School of Chemistry

College of Engineering and Physical Sciences

University of Birmingham

August 2022

Abstract

The all-inorganic halide perovskite ($CsPbI_3$) holds promise for photovoltaic applications but suffers from a detrimental phase transformation to a non-perovskite phase *δ*-$CsPbI_3$ at low-temperature. The synthesis and stabilization routes to this and other all-inorganic halide perovskites are still not ideal, requiring uneconomical elimination of humidity, toxic solvent or high-temperature quenching.

The all-solid-state synthesis method is a kind of green method to avoid the use of expensive and hazardous solvents. We have studied the influence of inorganic element doping and find that, on the one hand, the incorporation of other metal ions such as Bi^{3+} and Mn^{2+} makes little contribution to the stabilization of $CsPbI_3$; on the other hand, these ions seems to aid the formation of yellow phase at lower temperature and accelerate the decomposition of yellow phase into CsI and PbO at high temperature. Br^- doping is able to stabilize $CsPbI_3$ in air only for a few minutes to an hour, which lead to some observation of cubic phase in the PXRD pattern. Interestingly, a cubic phase dominant black powder can be obtained by the synergic contribution of Br^- and MA^+/FA^+ cations.

We also studied the synthesis of $CsPbI_3$ in air atmosphere at room temperature by solvent method. Water/moisture is commonly meticulously avoided due the fact that it can accelerate the detrimental degradation of the perovskite. In our work, we used an alternative approach of engineering an in situ degradation process to form a dual-functional PbI(OH) protective covering and succeeded in performing the first room-temperature synthesis of *γ*-$CsPbI_3$ under ambient

humidity. The vastly improved stability benefits from both lattice anchoring and physical coverage of *γ*-$CsPbI_3$ by an ultra-thin PbI(OH) layer. The resultant *γ*-$CsPbI_3$ is stable for more than 2 months under ambient conditions (25 °C, RH 30 - 60%).

Anti-solvent assistanted crystallization (ASAC) is one the most commonly used methods for the deposition of high-quality perovskite solar cells, where anti-solvents are working to modulate the nucleation process of perovskite films by removing the host solvents, such as *N,N*-Dimethylformamide (DMF), Dimethyl sulfoxide (DMSO), *γ*-butyrrolactone (GBL). Their toxicity become a concern during the commercialization process of perovskite solar cells. Various green anti-solvents have appeared in recent years, aiming to reduce the hazardous pollution to human and environment during large-scale industrial production. However, limited green solvents, such acetic ether, anisole and so on, are proven to be efficient to reduce the dependence to the widely used toxic chlorobenzene (CB) and toluene (Tol). One of the most essential reasons is that the green anti-solvent couldn't satisfy the strict requirement of the self-nuclei process in high-quality perovskite films. To overcome this obstacle and establish more choices for green anti-solvents, we reduce the dependence of perovskite films to self-nuclei process, by adding perovskite $CsPbI_3$ NCs as artificial seeds. When $CsPbI_3$ NCs are added along with the alkane anti-solvents, the NCs could compensate the self-nuclei deficit and result in a high crystalline and dense film for high-efficiency perovskite solar cell.

Acknowledgement

As a student of the Joint PhD Training Program offered by the University of Birmingham (UoB) and Southern University of Science and Technology (SUSTech), I would like to express my heartfelt gratitude to my supervisors, Prof. Peter Raymond Slater in UoB and Prof. Zhubing He in SUSTech, for their supervision as well as to UoB and SUSTech for their support for my studies in both universities.

Thanks go to Lizzie and Bo for their help to my study.

Thanks go to collaborators Bing Han and Yudong Zhu for their help with Cryo-TEM, Han Gao for the help of material synthesis.

Thanks go to Floor 5 students at UOB, Doris, Abubakar, Mark and Matt, and students at SUSTech, Wei Chen, Zheng Du, Xusheng Zhang, Guocong Chen, Zhaoning Li and Qin Tan, for the help and friendship during my PhD.

I'd also like to thank my family for their support and encouraging.

Table of Content

1. Introduction

1.1 Metal halide perovskite

1.1.1 Structure

Metal organic halide perovskites have been developed very quickly in the past 20 years in terms of their flexible structure, prominent basic property, and versatile applications.[1-6] They are emerging as a class of star semiconductors with attractive properties and wide application in different areas, such as photovoltaic, light-emitting diode, photo-detector and X-ray detector.[7-16] Among them, halide perovskites are mostly famous for their application in solar cells, and the solar energy conversion efficiency of perovskite solar is increasing very quickly and reaching the latest record of 25.5% in a short period, which is close to that of a single-crystal silicon solar cell.[17-19]

The word 'perovskite' related to the mineral substance composed of $CaTiO_3$, which has similar crystal structure assembled by TiO_6 corner linked of octahedra, where Ca^{2+} is in the cavity sites.[20] Metal halide perovskites have a general formula of ABX_3, in which A site cations consist of a class of mono-valent cations, such as Cs^+, and organic cations, such as $MA^+(CH_3NH_3^+)$, $FA^+(NH_2CHNH_2^+)$.[5, 14, 21, 22] Besides, the doping of small organic cations, such as K^+ and Rb^+, as well same large organic cation has also been reported. The B site is occupied by series of divalent metal cations, such as Pb^{2+} and Sn^{2+} and Ge^{2+}.[23-28] Besides, the doping of B site by Ca^{2+}, Sr^{2+}, Cu^{2+}, Co^{2+}, Mn^{2+},Ge^{2+},Bi^{3+} into the B site is also very popular for the engineering

of halide perovskites in previous work.[29-34] X anions mainly consist of a halide anion such as F^-, Cl^-, $Br^-$and I^-.[35-37]

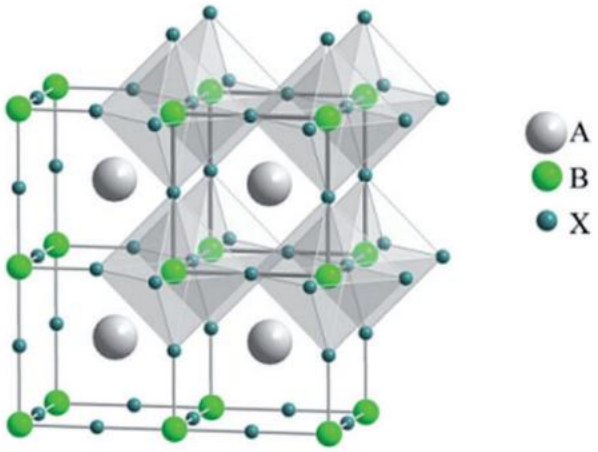

Fig 1.1 The structure of perovskite in the formula of ABX_3[38].

The structure of these halide perovskite is composed of $[BX_6]^{4-}$ octahedra which are corner linked.[39-42] Each divalent metal is coordinated by six halide anions to form $[BX_6]^{4-}$ octahedron as shown in fig 1.1. The A cation is in the void of the octahedral 3D network. Metal organic perovskite adopts a range of cell symmetries from cubic, tetragonal to orthorhombic, according to the distortion degree of $[BX_6]^{4-}$, which is closely related to the variation of temperature.[2, 39, 43] Usually, it tends to adopt a high-symmetry phase (cubic and tetragonal) at high temperature and low-symmetry phase at low temperature.[4, 44] It is noted that the favorable temperature to maintain the cubic structure is different for different perovskites.

$$t = \frac{r_A + r_X}{\sqrt{2(r_B + r_X)}} \qquad \textbf{Equation1.1}$$

The Goldschmidt tolerance factor *t*, as shown in equation 1,has been widely adopted to assess whether perovskites with different components can form a high-symmetry phase.[41, 45-47] In the equation of the tolerance factor, the ionic radius of atoms or molecules of A, B and anion X, are named by r_A, r_B and r_X, respectively. When $t > 1$, it means the radius of cation A is too large to stay in the framework; when $t < 0.8$, it means the radius of cation A is too small to support the framework. In both situations, the $[BX_6]^{4-}$ octahedron 3d network will be finally distorted into an unwanted non-perovskite phase, which is normally called the yellow phase. If $0.8 < t < 1$, a high-symmetry perovskite phase is generally adopted. This rule can direct people for the engineering of components in halide perovskite to obtain a series of A site, B site or X site mixed halide perovskites. The mixed perovskites play a very important role in the development of the perovskite solar cells. In a mixed perovskite, where A, B and X consist of more than one kind of atom, this rule is also working well. Almost all the certified cells in NREL with record efficiency contained a mixture of A-site cation or X-site, or both at the beginning of its development.[1] The component engineering not only can influence the stability of perovskite, but also can be used for the modification of the band gap and light absorption in the perovskite. These will be further discussed in the following section on mixed perovskites.

1.1.2 Optical-electron property

A continuous energy band is widely adopted to describe and analyze the solid state physics in materials or devices.[48-50] A featured energy band of semiconductors includes two bands. The upper one is named the conduction band, while the lower one is named the valence band. There is a band gap, E_g, between the valence band

and conduction band, where the existence of holes and electrons are not allowed in a perfect crystal. All the electrons are located in the valence band at the temperature of 0 K. Normally, the conduction band will be partially occupied by electrons at room temperature for a semiconductor, while it is still empty for insulators because the band gap is too large. Some electrons will be excited into the conduction band by the thermal energy and produce holes which have opposite charge in the valence band. Both the holes and electrons would contribute to the current flow. E_c and E_v are defined to be the energy level of conduction band minimum (VBM) and valence band maximum (VBM), respectively.

The concept of the conduction band and valence band are addressed in quantum mechanics. Valence electrons of one atom, or those usually found in the outermost band of the ground state orbitals, are capable of being shared with other atoms. In covalent bonds, valence electrons of multiple atoms share their orbitals. The original orbitals of the valence electrons blur together, creating a valence band in the molecule with discrete energy levels. Unlike the valence band, the conduction band rarely contains electrons. But in excited states, electrons will move into the conduction band. The bottom edge of conduction band in $CsPbI_3$ is mainly related to the orbitals 6p of Pb atom. The distribution of electron in the conduction band of $CsPbI_3$ follows the role of Fermi Dirac Distribution, $f(\varepsilon) = \{1/[\exp((E - E_f)/kT) + 1]\}$, where where $f(\varepsilon)$ is the occupation probability of a state of energy ε, k is Boltzmann's constant, E_f is the chemical potential or Femi level, and T is the temperature in Kelvin. As we can see from the equation above, when T trends to be 0 K, $f(\varepsilon)$ trends to be 0, which means there is no electron in the conduction band of $CsPbI_3$. As T increases, electrons have changes to be excited to conduction band. The equation above also reveals that, state

in conduction band with higher energy E, results to smaller $f(\varepsilon)$. Therefore, the state of energy at the bottom of conduction band, which is mainly related to the orbitals 6p of Pb atom has higher change to be occupied.

The band gap of halide perovskites varies from 1.2 eV to 2.8 eV depending on the choice of different components.[51, 52] To understand the origin of light absorption in perovskite, the electronic structure of $MAPbI_3$ has been analyzed by Density Functional Theory (DFT) and First-principle Theory-based Calculations, which shows the VBM and the CBM are mainly decided by the interaction of Pb^{2+} and I^- as shown in fig 1.2.[53, 54] Therefore, the interaction of the B site and X site dominates the band gap of halide perovskites, while A site cations have minor direct influence to the state of the band edge. However, It can influence the interaction of Pb-I in the perovskite by the contracting, expanding or distorting of the Pb-I framework, because the A site cations are located in the void between Pb-I octahedral 3D frameworks and interacting with the inorganic framework by van der waals interaction.[55] Therefore, in lead-based perovskite, the modulation of its band gap can be summarized into A site engineering and X site engineering.

Firstly, we are going to discuss the influence of the A site on the band gap of the perovskite. Cs^+, MA^+ and FA^+ are the most frequently used and studied cations. Among them, Cs^+ has the smallest effective ionic radius of 188 pm, which is expected to induce a contraction of lattice. As a result, Cs based perovskites exhibit the largest band gap E_g of 1.7 eV.[56] $MAPbI_3$ has a middle band gap of 1.60 eV, while the band gap of $FAPbI_3$ can be reduced to 1.53 eV due to the expansion of the Pb-I frameworks caused by the increasing size of FA^+.[55]

Secondly, with regard to the influence of the halide to the band gap, this acts in in a direct way, since, as we mentioned that the VBM and CBM is mainly decided by the interaction between lead and halide. Studies show that the band gap of the perovskite with different X follows the rule of $Eg_I < Eg_{Br} < Eg_{cl}$. It is found that the substitution of small halogens with large one would increase the VBM of perovskite, where the VBM shifts to a lower ionisation potential due to the high lying halide p states of the heavier halogens because VBM is mainly resulted from the hybridization of the orbitals I-5p and Pb-6s, while the CBM shows small variations during the substitution because CBM is mainly related to the orbitals 6p of Pb atom.[40] Taking $MAPbX_3$ ($X=Cl^-$, Br^-, I^-) for example, their wavelength of photo-luminescence ranges from 390 nm to 790 nm by the mixing of element in X site.[57]

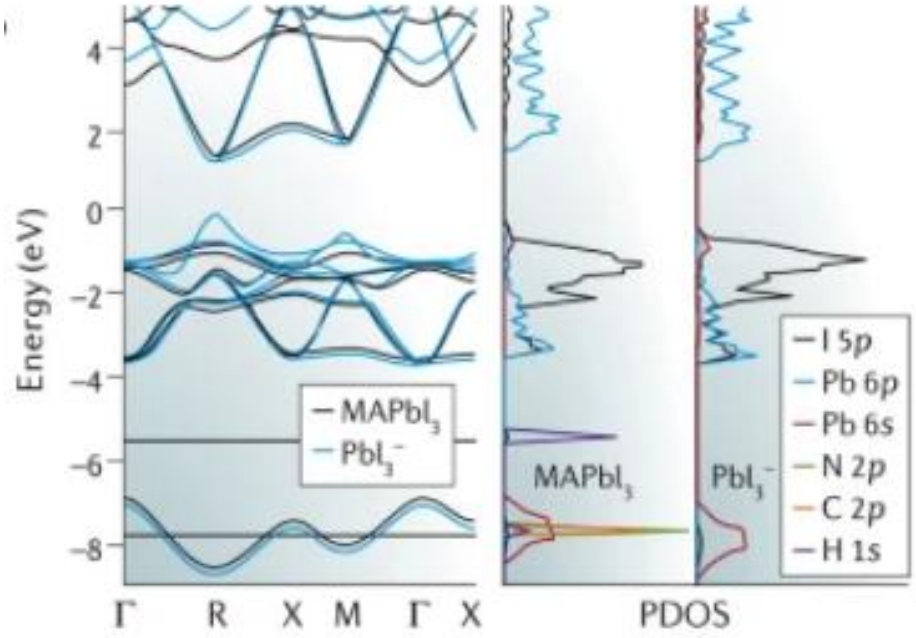

Fig 1.2 Band gap structures of the cubic inorganic framework PbI_3^- and cubic $MAPbI_3$ by DFT method.[53]

1.1.3 Application

Owing to the excellent optical-electronic property of perovskite materials, it has been applied into various fields, such as optical and energy areas. Halide perovskite materials play an important role in the field of solar cell in the past 20 years. Commercial solar cell nowadays in the market are mainly made of single-crystalline silicon. However, single-crystalline silicon solar cell has high-cost fabrication process. Halide perovskite are emerging as star materials with both the merits of low-cost fabrication process and high solar conversion efficiency. Because of the high absorption efficiency of perovskite to visible light, the conversion efficiency of single-junction perovskite solar cell has been catching up with that of single-crystalline silicon solar cell over the last 20 years. The wide band gap perovskite, such as $CsPbI_3$, can also be combined with a narrow band gap material, such as silicon and organic semiconductors to establish a tandem solar cell to further increase the utilization of solar energy. Application in light emitted diode is another hot area for halide perovskites because of their tunable band gap and good illuminating property. In addition, perovskite has also been widely studied in the field of photo-catalysis, x-ray detection, laser and so on.[58-62]

1.2 $CsPbI_3$

1.2.1 Advantages of inorganic perovskite

Organic halide perovskite or hybrid halide perovskites have a problem of thermal stability.[63] For example, bulk $MAPbI_3$ decomposes at a temperature above 200 ^oC, while the performance of perovskite films becomes worse because of their high

surface to volume ratio of small grains as well as inherent instability.[64] It has been proven that the organic-inorganic halide perovskites tends to degrade into PbI_2 gradually as the temperature increases to 85 ^oC with the direct observation of the color changing from black into yellow. This originates from the volatile nature of MA^+.[65] The incorporation of FA^+ into perovskite can improve this situation to some extent, but it brings in structural instability to humidity at the same time because the larger FA^+ leads to a more hygroscopic perovskite.[64, 66]

All inorganic halide perovskites are inherently more stable because they do not produce volatile decomposition products at high temperature or under illumination. Interestingly, the doping of small amount of Cs^+ into FA^+/MA^+ perovskites can also help to improve their thermal stability hugely.[67] At the same time, the phenomenon of light induced halide segregation, which widely exists in organic inorganic hybrid halide perovskites is minor in all inorganic halide perovskite due to their high ion migration energy barriers compared that of MA^+.[68] In addition to the excellent thermal stability, inorganic perovskite such as $CsPbI_3$ display a good optical band gap of 1.73 eV, which is an ideal valence to configure tandem cells as a top cell combined with either silicon or other low band gap perovskites.[56, 69, 70]

1.2.2 Structure evolution of $CsPbI_3$

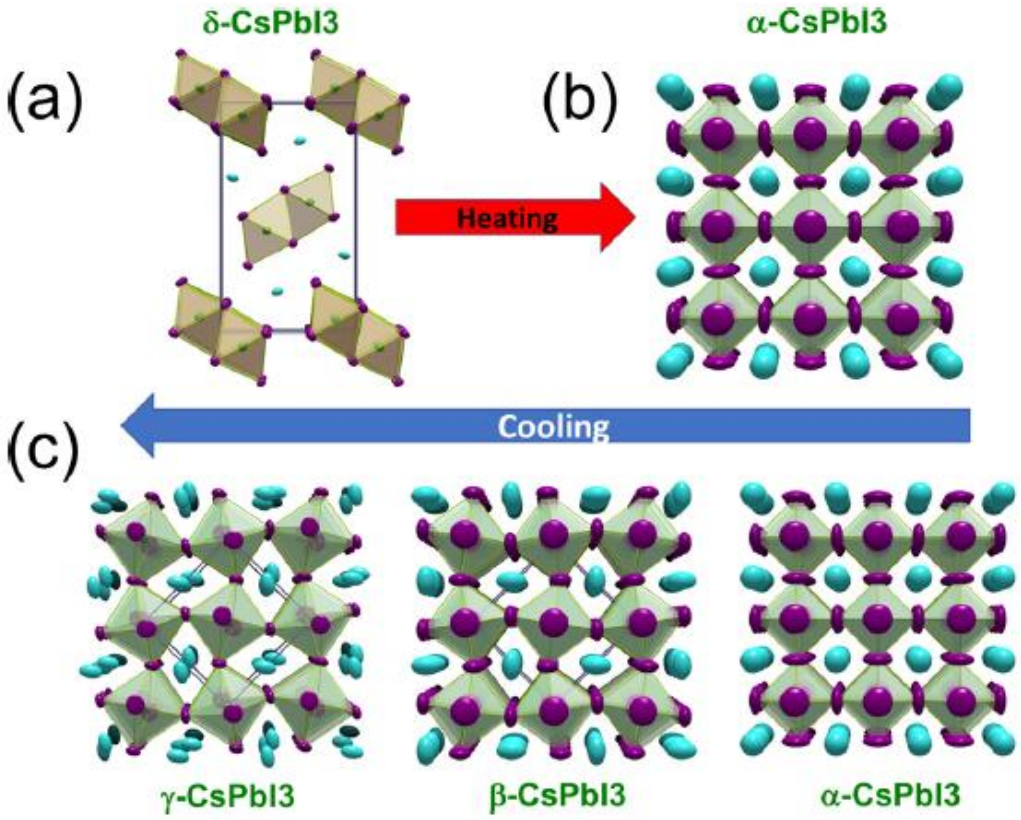

Fig 1.4 Structural phase transitions in $CsPbI_3$ versus temperature.[4]

Although all inorganic perovskites are prominent in terms of thermal stability, they suffer from undesirable phase transformation at room temperature from the black phase, especially for $CsPbI_3$ or I^- rich halide perovskites, to the photo-voltaic inactive yellow phase.[2, 43, 68, 71] It is of crucial importance to have a comprehensive understanding of different phases in all inorganic perovskite. In short, there are four known phases reported in $CsPbI_3$, cubic phase (α phase), tetragonal (β phase), and two kinds of orthorhombic phases, which are black *γ* phase and a non-perovskite yellow δ phase respectively as shown in fig 1.4. *α*, *β* and *γ* phase are stabilized at

different temperature and have *Pm*3*m*, *P*4*/mbm*, and *Pbnm* space groups, respectively. Even's group also gave a detailed description for all the phases versus temperature of $CsPbI_3$ in 2018 as shown in Fig 1.5.[4] The experimental structures were studied using synchrotron X-ray powder diffraction (SXRD). The yellow *δ* phase is the well-known stable phase at room temperature but converts to black α phase after heating above 325 °C. The black α phase is the desired phase with suitable optical band gap and good photo-voltaic activity. However, α phase can only be maintained at high temperature. The cubic phase will convert into the β phase at 260 °C and *γ* phase at 175 °C during the cooling process, accompanied by the decreasing of cell volume.[10] The transformation is thought to be induced by the distortion of Pb-I octahedra, leading to the reduction in symmetry .[72]

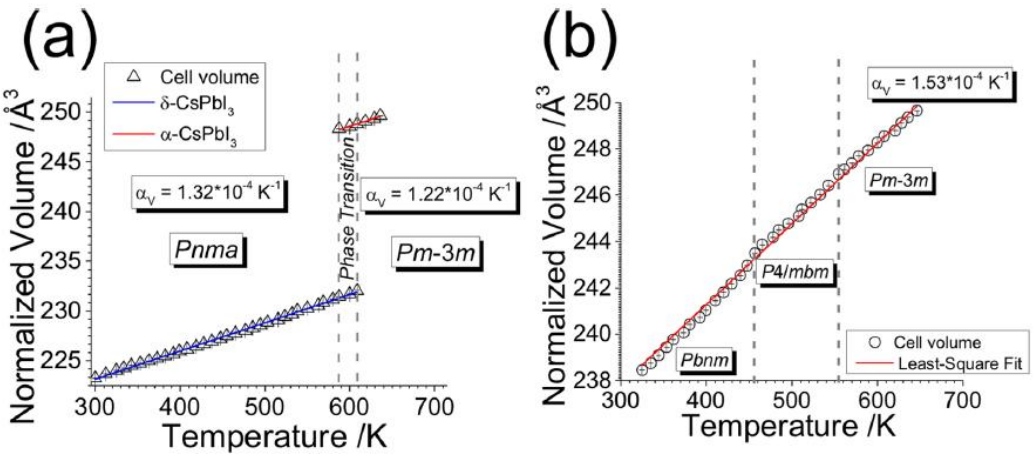

Fig. 1.5 Cell volume variation depends on the temperature a) increasing and b) decreasing.[4]

The transformation from *δ* phase $CsPbI_3$ into *α*-$CsPbI_3$ is accompanied by large changes in cell volume as shown in Fig 1.5, indicating that there are dramatic

re-arrangements of corner connected Pb-I octahedra during the heating process.[4] On the contrary, the cell volume shrinks gradually with decreasing temperature without dramatic changes. This trend reveals that *α*-$CsPbI_3$ converts into β and *γ* phase successfully instead of the δ phase during the cooling process. Although *γ*-$CsPbI_3$ still exists as a meta-stable black phase in room temperature, which converts into *δ* phase $CsPbI_3$ after a few days in a nitrogen atmosphere, it became a crucial part of photo-voltaic application nowadays.[73] At the same time, Snaith's group also found the similar transformation process from *α*-$CsPbI_3$ to *γ*-$CsPbI_3$.[74] They reported that rapid cooling of α-$CsPbI_3$ in an inert atmosphere resulted in black *γ*-$CsPbI_3$, which could convert into the cubic phase again by heating to 583 K. The structural information of *γ*-$CsPbI_3$ obtained by Rietveld refinement of these patterns is consistent with the results reported by Even's group.[4] In their report, the authors further found that slow cooling of *α*-$CsPbI_3$ would result into *δ*-$CsPbI_3$ instead of *γ*-$CsPbI_3$ at room temperature.

1.2.3 Challenges for $CsPbI_3$

Firstly, it is urgent to find methods to suppress the phase transformation from the cubic phase to the yellow phase when the temperature decreases. Until now, most of the reported black $CsPbI_3$ powder at room temperature are most likely to be orthorhombic *γ*-$CsPbI_3$, in which there is a slight increase in band gap caused by the distortion of Pb-I octahedra.[73] Moreover, *γ*-$CsPbI_3$ is also a meta-stable phase, which converts gradually into *δ*-$CsPbI_3$.[75, 76]

Secondly, the universal method to obtain α-$CsPbI_3$ is heating $CsPbI_3$ over 300 °C, which not only consumes lots of energy but also limits the wide application of perovskite, such as in flexible devices. Therefore, it is meaningful to reduce the phase transformation temperature to obtain cubic phase.

Thirdly, the black phase perovskite is very sensitive to the ambient environment, such as humidity and oxygen, which has a great influence on the performance of PSCs. The polar property of H_2O molecules promotes the movement of ions in the halide perovskite and accelerates the degradation as shown in fig 1.6.[77, 78]

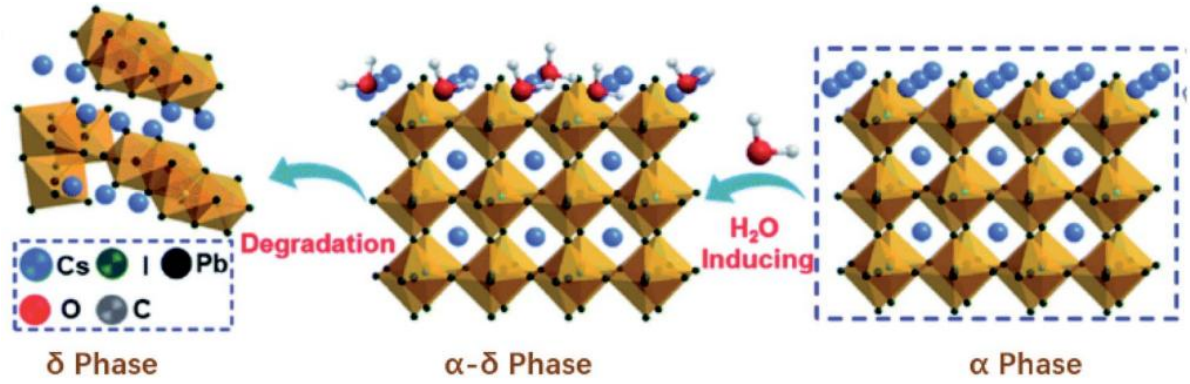

Fig 1.6 The $CsPbI_3$ degradation process from α to *δ*-phase.[78]

1.2.4 Strategies to stabilize $CsPbI_3$

Various strategies have been tried to stabilize the black cubic phase perovskite: (a) reduction of size into quantum dot (QD). The high surface energy in $CsPbI_3$ quantum dots help to stabilize the black phase at room temperature. Luther's group reported that *α*-$CsPbI_3$ QDs are stable as the black phase for months in ambient air in 2016.[79] However, the intrinsic stability of black phase $CsPbI_3$ is still not fully understood and the requirement of shape in quantum dot limits its wide application in many areas, such as high efficiency perovskite solar cells. (b) HI has been widely used as an additive to stabilize the black phase at room temperature. It can also help to reduce

the phase transformation temperature from yellow phase to black phase to around 100 ^{o}C.[73] Snaith's group claimed in 2015 that the incorporation of HI can reduce the grain size and it is possible that the slightly strained crystal lattice benefits for the stabilization of *α*-$CsPbI_3$.[80] However, there is no convincing explanation for this mechanism. Recently, the HI-stabilized black phase $CsPbI_3$ was proven to be *γ*-$CsPbI_3$ instead of *α*-$CsPbI_3$ by Snaith's group.[74] Hu's independent work in 2008 also confirmed the formation of *γ*-$CsPbI_3$.[73] However, Kanatzidis's group proposed a different opinion afterward.[81] They announced the HI-phase is actually an organic inorganic hybrid perovskite $Cs_{1-x}DMA_xPbI_3$, x = 0.2 to 0.5) (DMA =dimethylammonium, $(CH_3)_2NH_2^+$). The MDA^+ is thought to be slowly hydrolyzed from DMF in precursor, while the addition of HI accelerates this degradation process. Finally, the *α*-$Cs_{1-x}DMA_xPbI_3$ is sometimes confused as $CsPbI_3$ because there is minimal different in their PXRD patterns. (c) Excessive CsI is used to stabilize black phase $CsPbI_3$. Through variation in stoichiometry investigation, α-$CsPbI_3$ was successfully obtained with excess CsI in an air atmosphere by Chen's group.[82] The transformation temperature is also reduced to 110 ^{o}C. Park's group also report the enhancement of stability of Cs^+-rich $CsPbI_2Br$.[83] However, the exact mechanism is still unclear and more similar work needs to be done to confirm this phenomenon. (d) Metal ion doping is one of the most promising strategies to stabilize cubic phase $CsPbI_3$ at room temperature, which provides an approach to improve the undesired Goldschmidt tolerance factor (t). In other words, either larger A-site ions and/or smaller B-site and X-site substitution ions allow the Goldschmidt tolerance factor values more favorable for cubic perovskite formation. A closely packed atom arrangement is expected to

stabilize the cubic cesium-lead halide perovskites at room temperature.[84] e) external coverage by polymer or inorganic materials.

1.3 Perovskite solar cell

1.3.1 Progress of perovskite solar cell

Metal halide perovskites have been targeted as future generation materials in the field of solar cell since early 2005. The efficiency of solar energy conversion has increased rapidly from 3.7% to 25.7% in a short period. The fast increasing of efficiency, which is close to single-crystalline silicon solar cell, as well as the low-cost fabricating process of perovskite solar cell is challenging the dominance of the commercial single-crystalline solar cell.

Efforts to boost the efficiency of perovskite are summarized into 3 parts, which are the engineering of light absorption of perovskite bulk film, engineering of carrier transport layers, and passivation of interfaces between different layers. The light absorption engineering is mainly working on modifying the components of the perovskite layer to improve both their stability and ensure suitable band gap. Carrier transport layers are essential parts of the perovskite solar cells, which play the role of the extracting the carrier out of perovskite; a larger amount of works are targeted at exploring new kind of high efficiency transport layers and the modification of existing transport layer materials; interface passivation is an indispensable process for high efficiency solar cell, because a large number of defects have been proven to be exist at the interfaces of different layers during the fabrication.

1.3.2 Device Structure

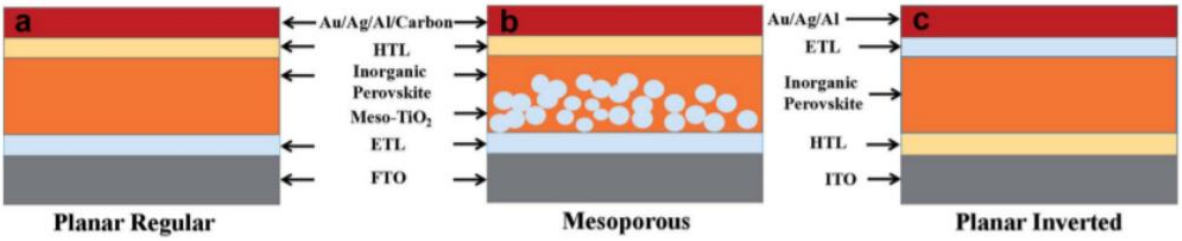

Fig 1.7 Device structure of perovskite solar cell.

Perovskite solar cell devices consist of following parts: transparent conductive substrates, hole/electron transport layers, perovskite active layers and back electrodes.[10, 85, 86]

Planar structure is one of the most popular device forms used in perovskite solar cell. According to the stacking order of different layers, the devices are divided into planar regular (n-i-p) and planar inverted structure as shown in fig 1.7. The n–i–p device stack generally consists of a transparent conductive oxide (TCO), electron transport layer (ETL, n-type semiconductor materials), perovskite absorber layer, hole transport layer (HTL, p-type semiconductor materials), back contact electrode as shown in fig 17a. In addition, mesoporous structure is used sometimes with an additional porous n-type layer on the electron transport layer to enhance the interaction between the perovskite layer and electron transport layer as shown in fig 1.7b.[87] The p-i-n device stack consists of similar layers in a n-i-p device with inverted order of HTL and ETL as shown in fig 17c.

Transparent conductive substrates are used to support the deposition of other functional layers and allow the illumination of light into the device, as well as to collect carriers generated from perovskite. The most commonly used transparent conductive

substrates both in lab study and commercial production is transparent conductive oxide (TCO) glass, such as Indium Tin Oxide (ITO) , Indium Zinc Oxide (IZO), Fluorine Doped Tin Oxide (FTO) with the benefits of their low-cost, stability and high transparency to visible light.[88]

Charge transport layers play the role of facilitating holes and electrons on both sides of the perovskite film. Electrons and holes are allowed to transport though the electron transport layer and hole transport layer respectively, to reach external circuit. Popular hole transport materials used in perovskites include nickle oxide (NiO_x), cuprous thiocyanate(CuSCN), Poly(3,4-ethylenedioxythiophene)/poly(styrenesulfonate) (PEDOT), Poly[bis(4-phenyl)(2,4,6-triMethylphenyl)amine] (PTAA), and so on, while the electron transport layers are mainly based on stannic oxide (SnO_2), titanium dioxide (TiO_2), [6,6]-phenyl-C61-butyric acid methyl ester (PCBM), fullerene (C60), and so on. [89-97]

Back electrodes in perovskite solar cell is responsible for the collection of charges generated. Therefore, Al, Cu, Ag, Au, carbon and so on, are commonly used for the back electrode of the perovskite cell. Price, stability, conductivity, work function need to be considered for the choice of the best electrode materials. In some particular situations, i.e. transparent perovskite solar cell, transparent conductive substrates, such as ITO or IZO would be used to replace traditional metal or carbon back electrodes.

1.4 Project objective

The all-inorganic halide perovskite ($CsPbI_3$) holds promise for photovoltaic applications but suffers from a detrimental phase transformation to a non-perovskite

phase δ-$CsPbI_3$ at low-temperature. The synthesis and stabilization routes to this and other all-inorganic halide perovskites are still not ideal, requiring uneconomical elimination of humidity, toxic solvents, or high-temperature quenching. In this project, we will systemically study all-solid-state synthesis method and doping strategy for the preparation of $CsPbI_3$. We will also examine the synthesis of $CsPbI_3$ by the solution method. Water/moisture is commonly meticulously avoided due the fact that it can accelerate the detrimental degradation of the perovskite. We propose an alternative approach of engineering an in-situ degradation process to stabilize $CsPbI_3$. Anti-solvent assisted crystallization (ASAC) is one the most commonly used methods for the deposition of high-quality perovskite solar cells, where anti-solvents are working to modulate the nucleation process of perovskite films by removing the host solvents, such as *N,N*-Dimethylformamide (DMF), Dimethyl sulfoxide (DMSO), γ-butyrrolactone (GBL). Their toxicity becomes a concern during the commercialization process of perovskite solar cells. Various green anti-solvents appear in recent years, aiming to reduce the hazard pollution to human and environment during large-scale industrial production, while most of them are not sufficient to build high-quality films for further applications. To overcome this obstacle and establish more choices for green anti-solvents, we will try to overcome their dependence to self-nuclei process, by adding perovskite $CsPbI_3$ nanocrystals as artificial seeds along with green anti-solvents during the preparation of perovskite films.

2. Experimental

2.1 Materials

The following materials were used.
Caesium carbonate (Cs_2CO_3, Energy Chemical, 99.9%), Lead iodide (PbI_2, TCI, 99.99%), Octadecene (ODE, Aladdin, 90%), Oleic acid (OAc, Energy Chemical, 90%), Oleylamine (OLA, Energy Chemical, 90%), Caesium bromide (CsBr, Alfa Aesar, 99.999%), Lead(II) iodide (PbI_2, TCI, 99%), lead(II) bromide ($PbBr_2$,TCI, 99%), Formamidinium bromide (FABr, GreatCell Solar ,99%), formamidinium iodide (FAI, GreatCell Solar, 99%) and Phenethylammonium iodide (PEAI, TCI, 99%). Nitrate hexahydrate (99.999%, Sigma-Aldrich).

Anhydrous isopropanol (IPA, 99.8%) was purchased from Energy Chemical. Methanol (99.8%) and ethanol (99.8%) were purchased from Alfa Aesar. Anhydrous solvents including *N*,*N*-dimethyl formamide (DMF), dimethyl sulfoxide (DMSO) and chlorobenzene (CB), were purchased from Sigma-Aldrich. Hexane, octane and decane were purchased from (Energy Chemical, extra dry 97%),

2.2 Materials Characterization

2.2.1 X-ray Powder Diffraction

X-ray powder diffraction (XRD) patterns were obtained using a Bruker ECO D8 series. Perovskite powder was pressed flatly on single-crystalline silicon substrate for collection of x-ray diffraction detail. Perovskite films on ITO were measured directly.

X-ray powder diffraction is a primary technology to identify the structure of crystalline materials. It can be used for calculating unit cell parameters of a substance, and for the analysis of impurity phases in products, as well as more detailed structural

information. This kind of equipment is generally composed of three basic parts, which are X-ray generator, sample holder, and X-ray detector. X-ray beam is generated by the sealed X-ray tube, where both unwanted white radiation and the characteristic X-ray radiation are emitted when the accelerated electrons hit the anode. The spectrum of generated characteristic X-ray radiation mainly consists of $K_{\alpha 1}$ and $K_{\alpha 2}$, while K_{β} radiation is suppressed because majority of XRD experiments require a monochromatic radiation.

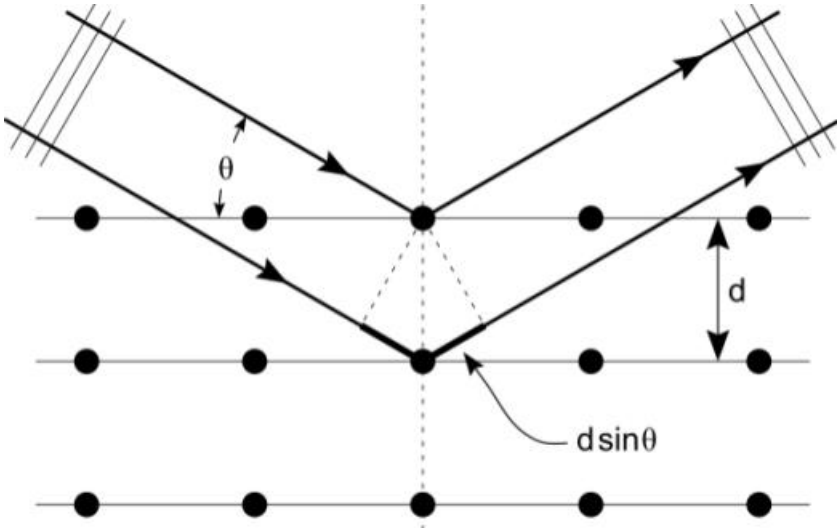

Fig 2.1 The illustration of Bragg's rule. The 'second' wave travels to an extra distance equal to 2dsinθ, and hence for constructive interference. This much equal an integral number of wavelength.

The samples need to be well ground and pressed flatly on the holder for tests. The diffracted X-ray will be detected by the detector. Scanning though a range of 2-theta will be conducted by the motion of arms automatically to obtain diffraction patterns. The physical foundation to resolve the structure information of crystalline material by x-ray diffraction is Bragg's law: $\lambda = 2d\sin\theta$ as shown in fig 2.1. When the wavelength λ of the radiation is close to the atom spacing, it will be scattered by lattice planes with

spacing d. To realize constructive interfere of scarred radiation, 2dsinθ needs to be equal to nλ, where n is the diffraction order.

The accurate structure of sample could be possibly solved from high-quality XRD pattern with the method of Rietveld Analysis. A crystallographic model was created firstly with certain parameters, such as unit cell and shape, atom position, fractional occupancies and independent thermal parameters. The parameters will be tuned by least-squares method until the simulated pattern is matched with experimental patterns. During this process, factors such as background information, peak position and peaks shape were all considered. A difference profile between calculated and experimental pattern is always used to indicate the rationality of refinement.

X-ray diffraction (XRD) data were collected using a Bruker D8 X-ray diffractometer (CuKα radiation 1.5418 Å). The patterns were recorded over the 2θ range 10° to 50° with a 0.02° step size in ambient environment at 20 ^{o}C - 25 ^{o}C with RH 40% - 70%.. Structure refinement was carried out using the XRD data with the GSAS suite of Rietveld refinement software.

2.2.2 Grazing-Incidence Wide-Angle X-ray Scattering

Thin perovskite films have small volume and therefore traditional XRD is not suitable in this scenario. The grazing-incidence wide-angle X-ray scattering (GIWAXS) is conducted with a very shallow incident angle so that the beam can transport though a significantly long path of thin film. High-brightness synchrotron radiation is commonly applied for GIWAXS increase the scattering intensity and signal to noise ratio. The

scattered beam **q** after interacting with sample is detected by a 2D detect. **q** consists of q_x, q_y and q_z in different directions, where q_{xy} and q_z are normally defined as in plane and out of plan direction as shown in fig 2.2. The scattered patterns of samples with random orientation is series of rings, and the intensities of the rings can reflect their crystallinity. Preferred orientation in the samples would result into the intensity fluctuation in a ring. Therefore, it can be used to study the in-plan (edge on) or out of plane (face-on) information of film samples as shown in in fig 2.2.

Our GIWAXS studies were performed at the BL14B1 beam line of Shanghai Synchrotron Radiation Facility (SSRF), Shanghai, China, with beam energy of 10 keV (λ = 1.24 Å) and a grazing-incidence angles of 1.0° .

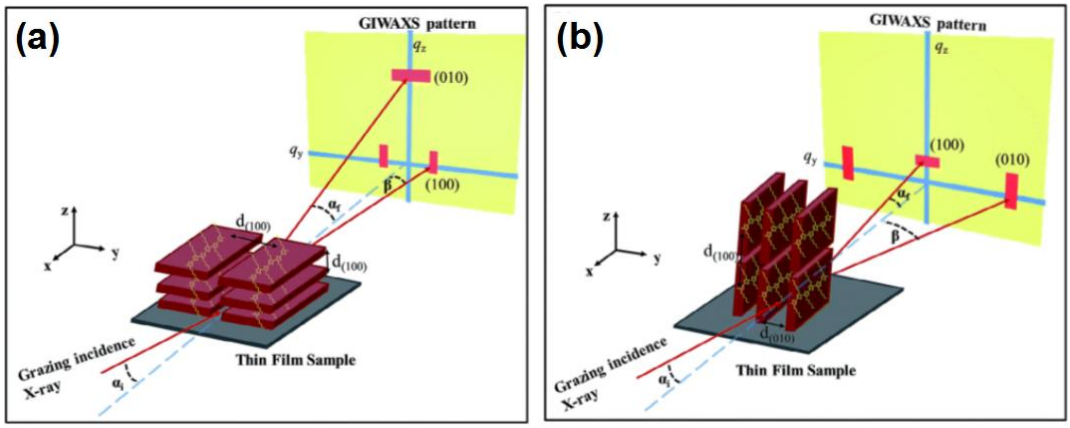

Fig 2.2 Demonstration of face-on and edge-on orientation of GIWAXS pattern.

2.2.3 Scanning Electron Microscopy

Scanning electron microscopy (SEM) was commonly used for the study of the morphology of samples. It works based on the signal produced by the interaction between the electron beams and electron in samples. Secondary electrons, which usually have low energy, are generated from the atoms of specimen within a few

nanometre below the surface, though inelastic scattering interactions. Therefore, secondary electrons are mostly popular for topography analysis. Morphology and elemental studies of perovskite film are most common and essential technology for perovskites.

SEM images were obtained by a TESCAN MIRA3 under 10 KV. 10 nm Au was sputtered on the samples by ISC150 ion sputter coater from SuPro Instrument LTD before measurements.

2.2.4 Transmission Electronic Microscope

A transmission electronic microscope (TEM) FEI Helios Nanolab 600i was used for the characterization of structure, elemental information, and morphology of the inorganic perovskite. It consists of the following parts of electron source, series of lenses, specimen holder and detector. The electron beam is focused by a series of lenses on samples. When the samples are crystalline, the diffraction pattern can be collected by the detector to analyse the structure. The transmitted beams after interaction with the samples also include elemental information of the specimen and can be detected by energy-dispersive spectrometer (EDS). Cryo-electron microscopy (Croy-EM) is a powerful tool to detect the structure of electron-sensitive organic-inorganic hybrid perovskites. It can protect the sample from the damaging high-energy electron beams by conducting the experiment at low temperature.

TEM has strict requirements for the preparation of samples. The samples need to be thin enough to allow the electron beam passing through. For the powder of $CsPbI_3$ in this project, it was dispersed in ethanol and dropped on copper net with supporting carbon film followed by drying at 100 ^{o}C for 10 min. For the study of the perovskite film

by TEM, the film was also spin-coated on the Cu holder with ultra-thin carbon supporting film directly for observation. Cryo-EM was carried out on a double Cs-corrected TEM (Titan Themis 60-300kV) performed by a Gatan cooling holder at the liquid nitrogen temperature. Using this Cryo-EM method, the samples can be cooled down to about -175 ℃. The dose rate for each Cryo-TEM image is controlled to below ~10 e $Å^{-2}$ S^{-1} for high resolution images and 1.5 e $Å^{-2}$ S^{-1} for the low magnification images, correspondingly.

2.2.5 Atomic Force Microscope

An Atomic Force Microscope (AFM) was used to analyse the roughness of the perovskite films, which has a great influence on the carrier transporting at the surfaces. It typically has a cantilever with tiny tip, a piezoelectric element (typically made of a ceramic material), and a laser detector feedback system. The detecting method of AFM relies on monitoring the force between two gathering atoms from tiny tip and top surface of sample, respectively. The accurate motion of tip in the z direction is controlled by piezoelectric part. The increasing of force leads to the motion of the cantilever, where the tip is fixed on. The detector will monitor the motion of the cantilever by detecting the reflected laser.

The measurements were conducted with MFP-3D-Stand Alone (Asylum Research Abingdon-on-Thames, UK) to investigate surface morphology. The measurements were carried out in ambient environment at 20 ^{o}C - 25 ^{o}C with RH 40% - 70%. AFM images with size of 3 x 3 um^2 and 512 x 512 pixel were recorded with tapping mode.

2.2.6 Photoluminescence

Photo luminescence (PL) is the light emitting from the sample after it is excited by a photon with higher energy. An electron is excited to a higher energy level by the photon and triggers various relaxation process. The excited electron fills the vacancy in the valence band and emits a photon. PL can be used for the analysis of the impurity and crystallinity of the perovskite in terms of the shift and intensity of the PL peaks. Time-resolved photo luminescence (TRPL) is a technology to measure the lifetime of photoelectron, which is the decay time of photo-luminescence after the excitation by laser pulse. TRPL is a convenient approach to detect the trapping states in the perovskite, which reflects the lifetime of the photo-electron.

The measurements were conducted with a spectrofluorometer (FS5, Edinburgh instruments), with a 405 nm pulsed laser and 150 W Xenon lamp as excitation sources. 405 nm pulsed laser was used for PL measurements. The PL measurements were conducted in ambient environment at 20 ^{o}C - 25 ^{o}C with RH 40% - 70%. The measurements were scanned from 600 nm to 1000 nm with a scan step of 2 nm. 150 W Xenon lamp was used for TRPL measurements. The samples were excited by light with fixed wavelength, such as 650 nm for $CsPbI_3$ and 780 nm for mixed-cations perovskite. The TRPL decay within 2 microsecond range was recorded.

2.2.7 UV-visible absorption spectroscopy

Different compounds usually exhibit different colors, which is because each substance can only absorb visible light with specific wavelength according to their components and structure. UV-visible spectrometry is used to measure the absorption or reflection of light from the spectrum range from ultra-violent light to full visible light. UV-vis

spectroscopy can be treated as complementary to the PL spectrum we discussed before. For perovskite materials, they have a tunable band gap based on the substitution of halide in the X position. Therefore UV-vis is an important characterization method for perovskites with different absorption. The UV-vis spectrum can also be used to calculate the optical band gap of the materials, which is a crucial factor for solar cells.

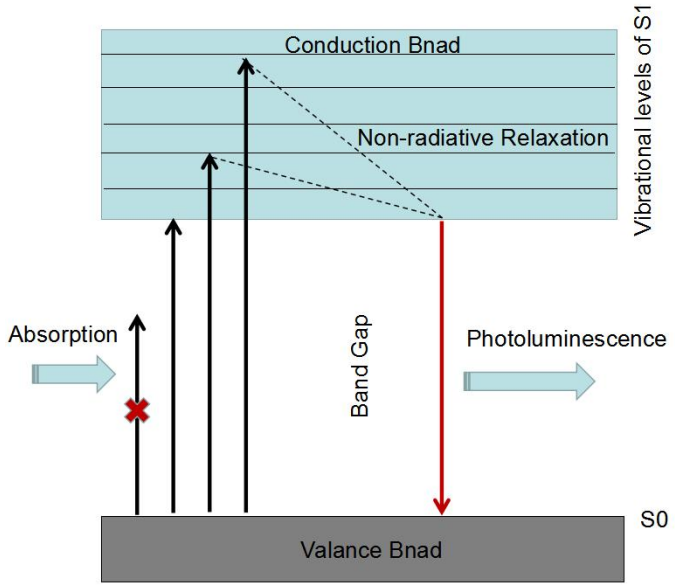

Fig 2.1 Energy diagram showing the absorption and photoluminescence processes.

As we can see from fig 2.1, electrons would be excited from ground state S0 to excites state S1 when the energy of incident photon ($h\nu$) is larger than the band gap of semiconductor. After absorption, the vibrationally excited S1 molecule relaxes back to the lowest vibrational level of S1 prior to photoluminescence by non-radiative relaxation. In terms of cubic phase $CsPbI_3$ with the band gap of 1.7 eV, its absorption spectrum covers almost all the visible light (780 - 400 nm), which results in a dark

color of $CsPbI_3$. The experimental emitting wavelength **λ** of $CsPbI_3$ is located around 705 nm, which can also be approximated by band gap Eg, **λ** = 1240/Eg.

The measurements were conducted on a LAMBDA 750 UV-visible-NIR spectrophotometer with spectrum range of 200 ~ 1500 nm. Samples were coated on glass substrates for measurements. The measurements were conducted in ambient environment at 20 ^oC - 25 ^oC with RH 40% - 70% and a scan step of 2 nm.

2.2.8 Fourier Transform Infrared Spectroscopy

Fourier Transform Infrared Spectroscopy (FTIR) was performed using an Agilent Technologies Cary 630 FTIR spectrometer with wavelength range of 4000 - 400 cm^{-1}. The maximum output power of semiconductor laser for excitation of samples is 0.5 mW. It works by performing a Fourier Transform (FT) on the interferogram of sample signal , which is collected using a interferometer. The perovskite films were spin-coated on KBr single-crystalline window chips instead of for measurements, because the absorption of ITO is strong when the wavenumber is above 1200 cm^{-1}. In this project, the intensity of featured vibration of S=O in DMSO and C=N vibration from FA^+ were measured to estimate the amount of DMSO residual in perovskite films. The measurements were conducted in ambient environment at 20 ^oC - 25 ^oC and 40% - 70% RH with a scan step of 1 cm^{-1}.

2.3 Device characterization

2.3.1 Power conversion efficiency measurement

The tests were conducted in an ambient environment at 20 ^oC - 25 ^oC and 40% - 70% RH. Devices were connected to a Keithley 2400 source meter and illuminated by an

Oriel Sol3A solar simulator with AM 1.5G spectrum. The intensity of light was calibrated to 100 mW/cm^2 by a standard KG-5 Si Diode. The illuminating area of the solar cell was 0.08 cm^2 realized by the covering of an optical aperture mask on the solar cell. Both reverse scan and forward scan, with a step of 10 mV from -0.2 V to 1.25 V, were recorded. The efficiency of the device is calculated by $\eta = J_{sc} * V_{oc} * FF$, where Jsc is the short-circuit current density, Voc is the open-circuit voltage and FF is the fill factor.

2.3.2 Maximum power point tracking

Maximum power point (MPP) tracking was used to evaluate the stability of the perovskite solar cells. The solar cells were sealed in N_2 atmosphere. The tests were conducted in an atmosphere at 20^{o}C - 25^{o}C and 40% - 70% RH. The MPP tracking was conducted on a homemade system with LED as light source. Changes of efficiencies along with the time at maximum power point were recorded for analysis.

2.3.3 External Quantum Efficiency

External Quantum Efficiency (EQE) refers to the ratio of the number of holes and electrons produced in a solar cell to the number of photons in incident light, which can reflect the energy conversion efficiency of the device. EQE measurement in this project was conducted in air atmosphere with an Enli-Tech instrument (Taiwan), which consists of a light source, a monochromator and a potentiostat.

2.3.4 Electrochemical impedance spectrum

The recording of electrochemical impedance spectrum (EIS) was used to calculate the series resistance (R_s) and charge transfer resistance (R_{tr}) of the perovskite solar

cell. The measurements were conducted on the Zahner Zennium electrochemical workstation in the dark with 5 mV alternating current sinusoidal voltage applied. The scan frequency was varied from 100 mHz-1MHz.

EIS is a emerging tool to study perovskite solar cell, because of the sandwich device structure and complex process in perovskite, i.e. ionic emigration. Impedance is used to describe complex circuits, which has nonlinear current-voltage relationship. EIS spectrum is obtain by applying a small AC potential, monitoring the current and recording the phase shift and amplitude changes over a range of frequency. The impedance is plotted as a Nyquist plot, which displays real and imaginary component. The variation of current along with frequency provide a change to separate the processes with different time scale in mixed conductor.

3. Synthesis of $CsPI_3$ by solid state reaction

3.1 Introduction

Dopant engineering has been systemically studied in solution processed halide perovskites. During the past 3 years, researchers have tried many kinds of metal ions to change the inherent stability of cubic $CsPbI_3$ at room temperature. They can be simply classified into: main group metal doping, transition metal doping, alkaline-earth and rare-earth ion metal doping.[98] Bismuth, which has slightly smaller radius than Pb^{2+} (Pb^{2+}: 1.19 Å and Bi^{3+}:1.03 Å), is one of the most thoroughly investigated elements. Bakr's group reported the successful incorporation of Bi^{3+} into single crystals of $MAPbBr_3$, triggering the obvious change of color.[99] In 2017, Zhang's group demonstrated the stabilization of *α*-$CsPbI_3$ with Bi^{3+}.[100] They revealed that the best doping concentration of Bi^{3+} is between 4% and 5%. Lower doping content cannot suppress the yellow phase efficiently while too high doping content would lead to side phase such as $Cs_3Bi_2Br_9$. The obtained α-$CsPbI_3$ was found to be stable in air for more than 168 hours. Mai's group found that the addition of $InCl_3$ can lead to the transformation of black *γ*-$CsPbI_2Br$ into *α*-$CsPbI_2Br$.[101] The authors explain that the incorporation of In^{3+} and Cl^- increases the tolerance factor and thus stabilizes α phase.

Transition metal doping is another popular way to enhance the stability of $CsPbI_3$ at room-temperature. There are plenty of works studying the doping effects of Mn^{2+}. Manna's group found that the introduction of Mn^{2+} can enhance the stability of $CsPbI_3$ in air from a few days to one month.[102] The successful incorporation of Mn^{2+} was proven by the shift of peaks in the PXRD pattern. Moreover, Donega's group

demonstrated the partial cation exchange in colloidal $CsPbBr_3$ NCs, resulting in doped $CsPb_{1-x}M_xBr_3$ QDs (M= Sn^{2+}, Cd^{2+}, and Zn^{2+};0< x ≤ 0.1).[103]

Rare-earth ions, such as Sm^{3+}, Eu^{3+}, Tb^{3+}, Dy^{3+}, Er^{3+}, and Yb^{3+} have been doped into $CsPbCl_3$ NCs by hot-injection method.[104] However, until now, only Eu^{3+} has been reported to lead to the stabilization of the black phase of $CsPbI_3$ in an ambient environment as reported by Miyasaka's group in 2018.[105] More importantly, the inclusion of Eu^{3+} decreases the phase transformation to 85 ^oC. The shift of PXRD peaks supported the successful doping of metal ions. However, for the doping of alkaline-earth metals, most of the works focus on the improvement of device performance by modifying the defects or layer interface instead of tuning the cell parameter. This is out of the scope of this project and so is not discussed further.

3.2 Design and results

The all-solid-state synthesis method is a kind of green method to avoid the use of expensive and hazardous solvents. However, research in the synthesis of $CsPbI_3$ by solid chemistry is still limited until now. Yellow $CsPbI_3$ is always obtained by solid chemistry in an air atmosphere by grinding CsI and PbI_2 powder together at ambient environment followed by heat treatments in a furnace in a fume cupboard. In this work, we have studied the influence of element doping and find that, on the one hand, the incorporation of other metal ions such as Bi^{3+} and Mn^{2+} makes little contribution to the stabilization of $CsPbI_3$; on the other hand, these ions seem to aid the formation of yellow phase at lower temperature and accelerate the decomposition of yellow phase into CsI and PbO at high temperature. Br^- doping can stabilize $CsPbI_3$ in air for a few minutes, which leads to very weak signals of cubic phase in PXRD pattern. Finally, a

cubic phase dominant black powder is obtained by the synergistic doping of organic cations and halide.

3.3 Synthesis

Synthesis of $CsPbI_3$ by solid chemistry was conducted in a furnace in a fume cupboard. The operation was conducted in air atmosphere with no control of humidity. The synthesis process involves weighing target reagents with an analytical balance. Stoichiometric amount of doping agent is mixed together in a mortar and pestle by hand to get a homogeneous mixture. Unlike the reaction within solution, the solid reactions are mainly occurring at the interface of particles by ionic diffusion. Therefore, a well ground mixture, to reduce the grain size, has a crucial influence on the next step of reaction. The mixture is then put into a furnace at different temperatures to react.

3.4 Characterization and Discussion

3.4.1 B site doping

Partially replacing the Pb^{2+} with other cations has the potential to not only improve their electronic and optical property, but also to reduce the usage of toxic Pb^{2+}. There is a wide range of cations available to attempt the substitution of Pb^{2+}.In this work, the partial replacement of Pb^{2+} was conducted with Ca^{2+}, Sr^{2+}, Cu^{2+}, Co^{2+}, Mn^{2+}, Mg^{2+}, Bi^{3+} and Sn^{4+}. The strategies used was to take the rules such as tolerance factors, stoichiometric proportions, and charge balance into consideration when we design the composition.

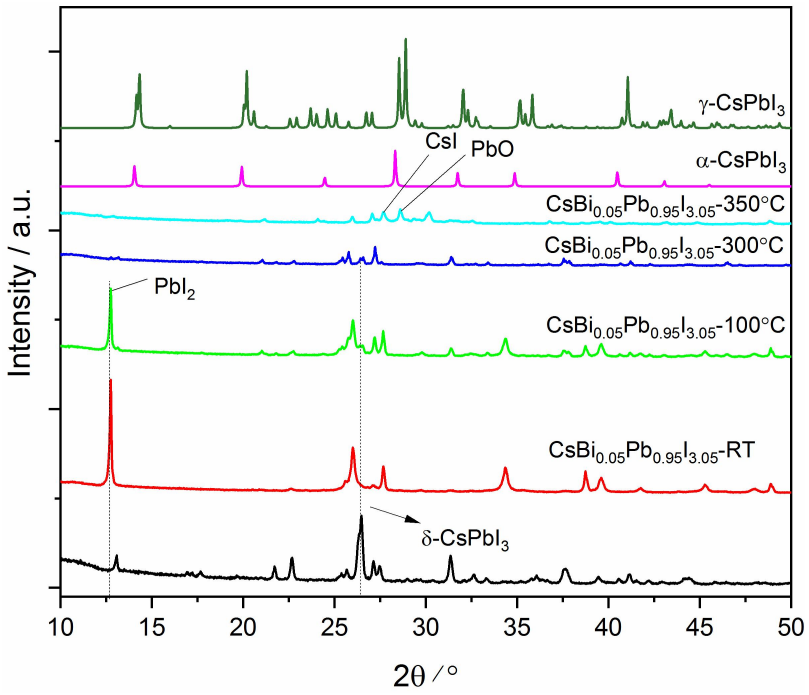

Fig. 3.1 PXRD pattern of Bi^{3+} doped samples prepared at different temperatures. For comparison, the XRD pattern for δ-$CsPbI_3$, α-$CPbI_3$ and γ-$CPbI_3$ are also shown. (CuKα radiation 1.5418 Å)

The incorporation of Bi^{3+} was implemented by substituting 5/10% PbI_2 with BiI_3, as shown in Reaction Scheme 1:

$$CsI + 0.95PbI_2 + 0.05BiI_3 \rightarrow CsPb_{0.95}Bi_{0.05}I_{3.05} \qquad \textbf{Reaction Scheme 1}$$

The BiI_3 doped samples were heated at 100°C, 300 °C and 350 °C respectively. The XRD patterns for these samples as shown in fig 3.1, proves the formation of the yellow phase $CsPbI_3$ at 300 °C similar to the undoped system. Moreover, no peak shift can be observed in XRD pattern for these Bi-doped samples compared with pure yellow phase $CsPbI_3$, indicating the failure of Bi^{3+} doping. Moreover, there is a strong

signal of PbI_2 (revealed at $2\theta=12.7^o$) in the samples prepared at room temperature. As the temperature increases, yellow phase $CsPbI_3$ begin to form and becomes the dominant component at 300 ^oC. The color of these samples are yellow, which is coincident with non-photoactive phase. The colors change to red when the temperature increases to 350 ^oC. The sharp peak at 27.7 ^{o} and broad peak at 28.7 ^{o} are assigned to CsI and PbO, respectively. This result shows that yellow phase $CsPbI_3$ decompose into PbO and CsI in the presence of O_2 at 350 ^oC.

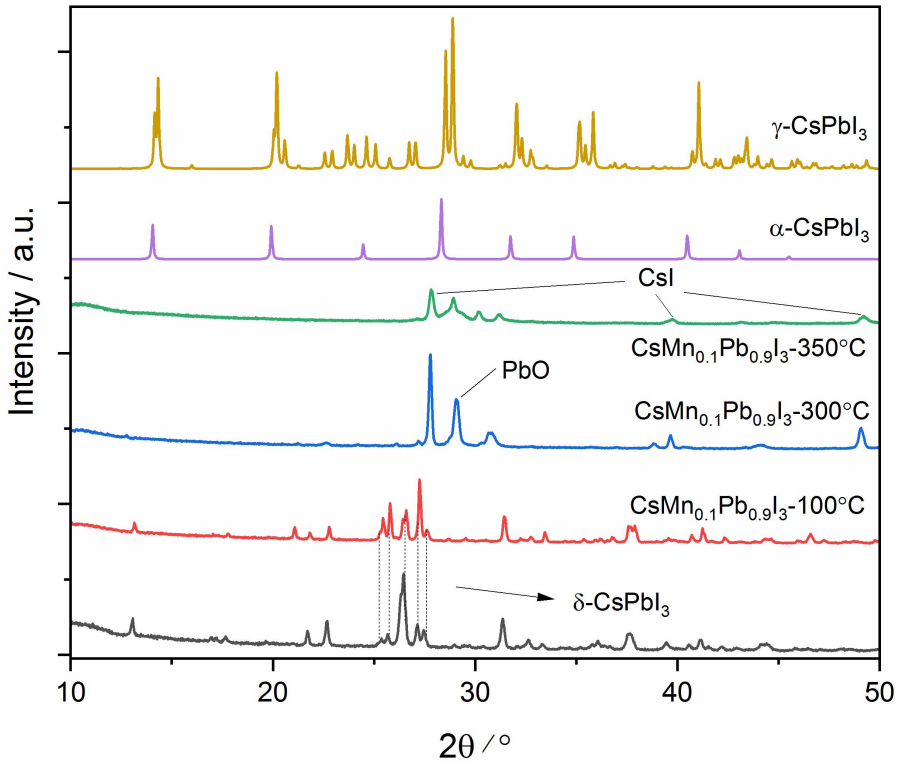

Fig. 3.2 PXRD pattern of Mn^{2+} doped $CsPbI_3$ prepared at different temperatures. For comparison, the XRD pattern for δ-$CsPbI_3$, α-$CPbI_3$ and γ-$CPbI_3$ are also shown. (CuKα radiation 1.5418 Å)

The attempted incorporation of Mn^{2+} followed the same route for Bi^{3+} doping as shown in Reaction Scheme 2.

$$CsI + 0.95PbI_2 + 0.05MnI_2 \rightarrow CsPb_{0.95}Mn_{0.05}I_3$$ **Reaction Scheme 2**

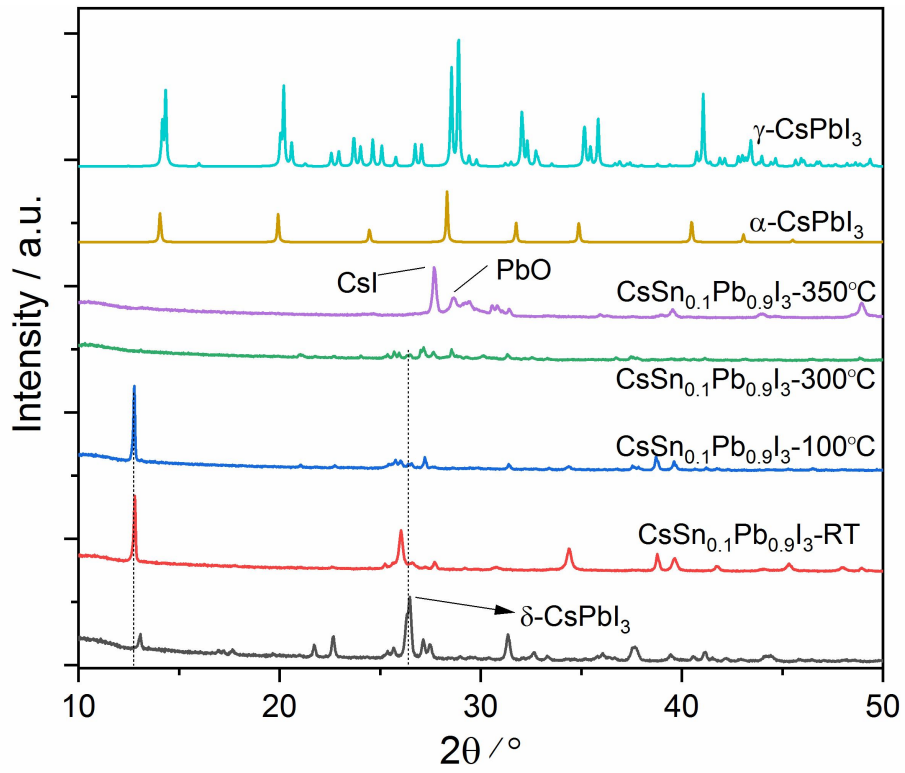

Fig. 3.3 PXRD pattern of Sn^{4+} doped $CsPbI_3$ prepared at different temperatures. For comparison, the XRD pattern for δ-$CsPbI_3$, α-$CPbI_3$ and γ-$CPbI_3$ are also shown. (CuKα radiation 1.5418 Å)

It is found that the addition of MnI_2 not only reduced the formation temperature of the yellow phase $CsPbI_3$, but also reduced its thermal stability. As we can see from the XRD pattern in fig. 3.2, the mixture totally transfers into yellow phase $CsPbI_3$ at 100 °C, compared with 300 °C for the Bi^{3+} doped system. However, there is no significant shift on the doping of MnI_2. Moreover, heat treatment at 300 and 350 °C results in the

decomposition of the yellow phase $CsPbI_3$ forming CsI, which is shown by the appearance of peaks at 27.7 °, 39.7 ° and 49.1 °. Signal from PbO also begin to appear at 300 °C.

$Cs_2Sn(IV)I_6$ is a type of vacancy-ordered double perovskite, which is a derivative of halide perovskites with ordered Sn-I octahedral vacancies. It is formed by removing half of the Sn in the formula of $CsSn(II)Sn(II)I_6$ to yield an isolated Sn-I octahedral framework. So, we assume that the incorporation of Sn(IV) into $CsPbI_3$ might produce some vacancies in the frameworks to relax the strain in lattice. Following this hypothesis，10% of the SnI_4 is used to replace PbI_2 as shown in the Reaction Scheme **3:**

$$CsI + 0.9PbI_2 + 0.1SnI_4 \rightarrow CsPb_{0.9}Sn_{0.1}I_{3.3}$$ **Reaction Scheme 3**

(Note although the formula above is normally written as anion excess, it is likely that cation vacancies would form in preference)

The reactants were ground in a mortar and pestle in air and heated at 250 °C, 300 °C, 325 °C respectively. The products were found to be yellow phase $CsPbI_3$ formed at 300 °C before completely decomposing at 325 °C. As shown in Fig. 3.3, the peak at 12.7 ° assigned to PbI_2 at room temperature vanishes at 300 °C, while the peaks belong to yellow phase $CsPbI_3$ appear. However, the yellow phase $CsPbI_3$ has already begun to decompose under this temperature as evidenced by the appearance of peaks assigned to CsI and PbO at 27.7 ° and 28.7 °.

The influence of Sr^{2+} and Ca^{2+} was studied by replacing 25% PbI_2 as shown in fig 3.4 Yellow phase $CsPbI_3$ is formed at room temperature as evidenced by the disappearance of the featured peak of PbI_2 at 12.7° and the appearance of a peak at

13.1° which belongs to yellow phase $CsPbI_3$. The crystallinity of $CsPb_{0.8}Ca_{0.2}I_3$ increases when the temperature increases to 300 °C. In comparison, there are two unknown peaks appears at 24.0° and 28.6° for $CsPb_{0.8}Sr_{0.2}I_3$ at 300 °C. However, both samples are still yellow with the absence of black cubic phase. Thus, the results suggested that the Ca^{2+} and Sr^{2+} doping were unsuccessful.

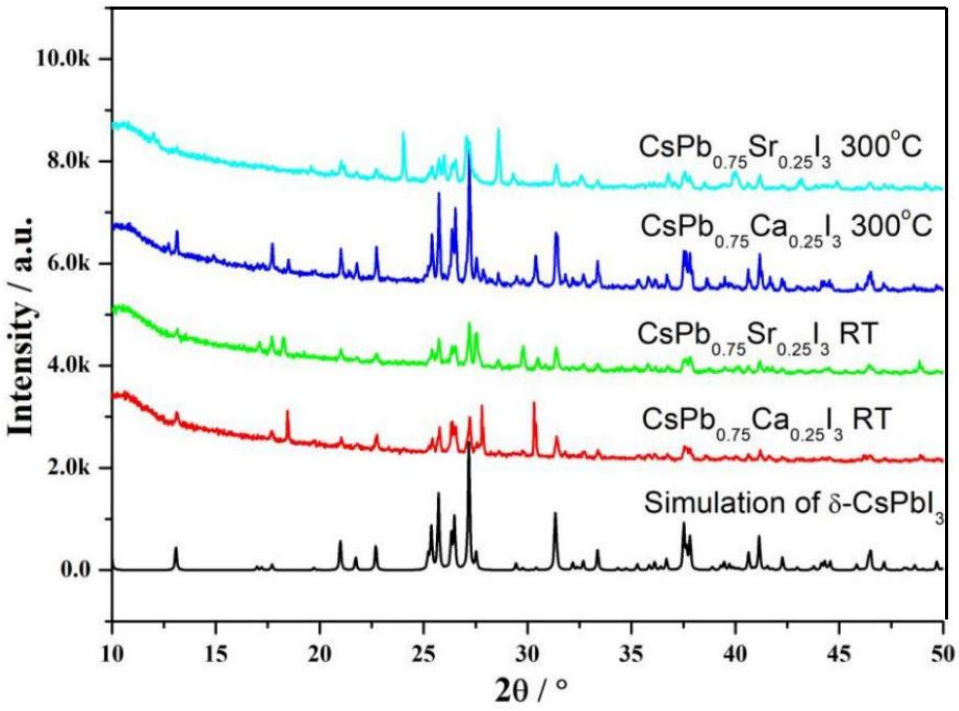

Fig 3.4 PXRD pattern of $CsPb_{0.8}Ca_{0.2}I_3$/$CsPb_{0.8}Sr_{0.2}I_3$ prepared at different temperature. For comparison, the XRD pattern for δ-$CsPbI_3$ is shown. (CuKα radiation 1.5418 Å)

Mg^{2+}/Co^{2+} and Cl^- co-doping were also investigated. 25% PbI_2 were replaced by $MgCl_2$ and $CoCl_2$, respectively. $CsPb_{0.75}Mg_{0.25}I_{2.5}Cl_{0.5}$ prepared at 200 °C is proven to form the yellow phase as shown in fig 3.5 and fig 3.6. Then the sample begins to decompose as the temperature increases. Similarly, $CsPb_{0.75}Co_{0.25}I_{2.5}Cl_{0.5}$ transfers into yellow phase $CsPbI_3$ at low temperature and begins to decompose at 200 °C. This experiment was also therefore unsuccessful.

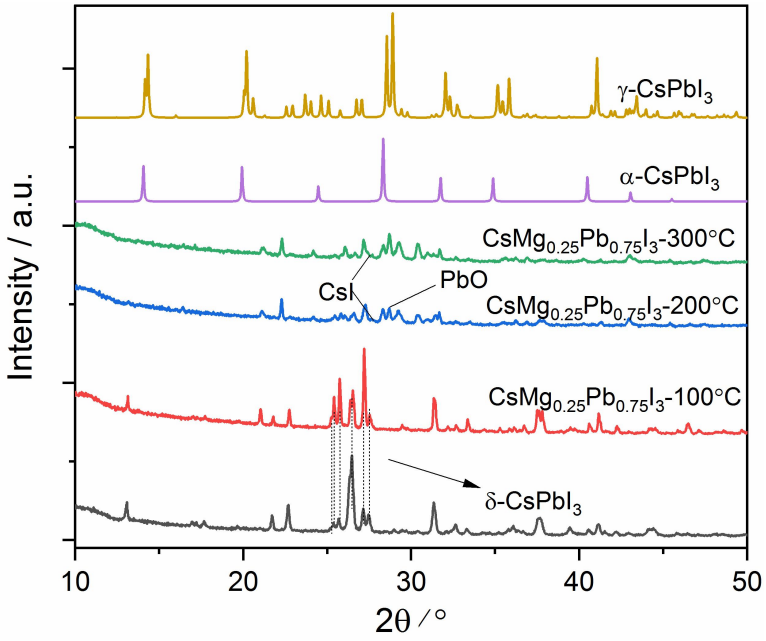

Fig. 3.5 PXRD pattern of $CsPb_{0.75}Mg_{0.25}I_{2.5}Cl_{0.5}$ prepared at different temperature. For comparison, the XRD pattern for δ-$CsPbI_3$, α-$CPbI_3$ and γ-$CPbI_3$ are also shown. (CuKα radiation 1.5418 Å)

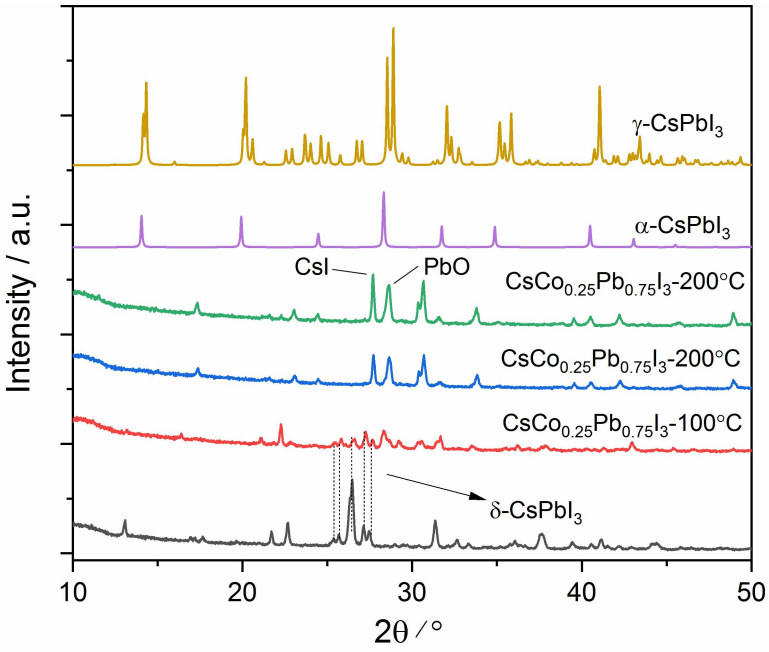

Fig. 3.6 PXRD pattern of $CsPb_{0.75}Co_{0.25}I_{2.5}Cl_{0.5}$ prepared at different temperature. For comparison, the XRD pattern for δ-$CsPbI_3$, α-$CPbI_3$ and γ-$CPbI_3$ are also shown. (CuKα radiation 1.5418 Å)

3.4.2 A site doping

The previously studied B site doping experiments showed limited progress in decreasing of transformation temperature of cubic phase and improvement of its stability with the result that the doping strategies were unsuccessful. The latter part of this work will be focused on A site doping strategies.

3.4.2.1 Excess CsI adding

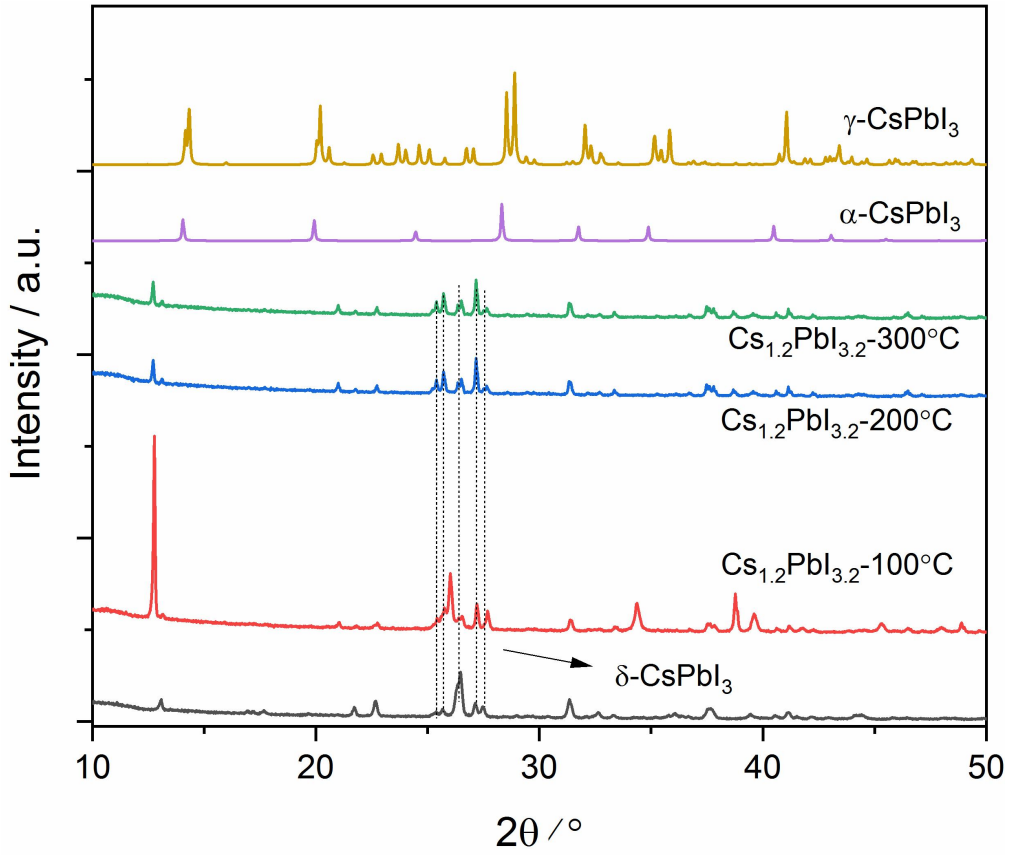

Fig. 3.7 PXRD pattern of $Cs_{1.2}PbI_{3.2}$ prepared at different temperature. For comparison, the XRD pattern for δ-$CsPbI_3$, α-$CPbI_3$ and γ-$CPbI_3$ are also shown. (CuKα radiation 1.5418 Å)

Non-stoichiometric effects, such as excess CsI, has been previously investigated by a solution route and resulted into the formation of black phase $CsPbI_3$ in air with a transformation temperature around 110 °C.[106] In our experiment, we investigated a solid state syntheses route. CsI and PbI_2 with mole ratio of 1.2 was mixed with a mortar and pestle, followed by heating at different temperatures. As can be seen from Fig 3.7, the mixture turns into yellow phase $CsPbI_3$ gradually as temperature increases to 300 °C.

3.4.2.2 Li•H_2O

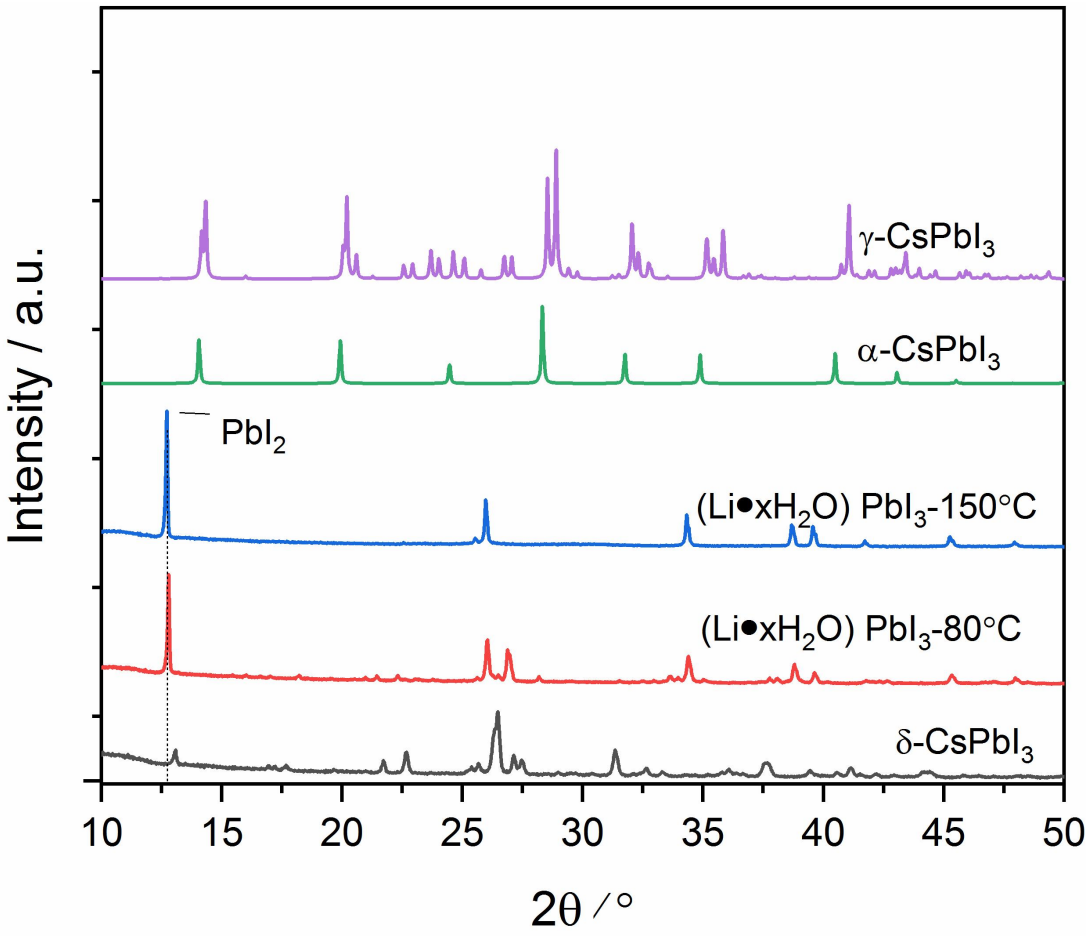

Fig. 3.8 PXRD pattern of (Cs • xH_2O) PbI_3 prepared at different temperature. For comparison, the XRD pattern for δ-$CsPbI_3$, α-$CPbI_3$ and γ-$CPbI_3$ are also shown. (CuKα radiation 1.5418 Å)

In addition to Cs, other alkaline metal, such as Na, Li, Rb, might also be possible to substitute onto the A site. However, none of them can form black phase because of their small size. To fill in the spare space in the A side properly, incorporation of alkaline cation with water molecule at same time might help to stabilize the structure as shown in Reaction Scheme 3:

$$LiI + PbI_2 + H_2O \rightarrow (Li{\bullet}xH_2O)PbI_3$$ **Reaction Scheme 4**

CsI, PbI_2 and LiI (1:1:0.1) were weighed and grounded a few drops of water was added during the grinding process. Considering the thermal stability of coordinated water, the heating temperature was set to be 80 ^oC and 150 ^oC respectively. However, the color of the mixture stayed in yellow all the time, indicating that there is no black phase forming during this process.

The samples were further characterized with XRD as shown in Fig 3.8. The peak that appears at 27 ^{o} for the sample prepared at 80 ^oC is presumed to be caused by a Li-rich phase because of the large residual PbI_2 peak is very strong (reveal at 2θ=12.7).[107] This peak vanishes in sample at 150 ^oC, while the peaks belong to PbI_2 is intensified indicating the decomposition of compound.

2.4.2.3 $BaPbI_2SO_4$ / $BaPbI_2CO_3$

No previous attempt has been paid to the substitution of Cs^+ with Ba^{2+} and so this was also investigated. To satisfy the requirement for charge balance in Ba^{2+} doped $CsPbI_3$,

oxoanion with -2 charge, such as SO_4^{2-} and CO_3^{2-} were chosen. The expected synthesis scheme is displayed in **Reaction Scheme 5 and 6:**

$$BaSO_4 + PbI_2 \rightarrow BaPbI_2SO_4 \qquad \textbf{Reaction Scheme 5}$$

$$BaCO_3 + PbI_2 \rightarrow BaPbI_2CO_3 \qquad \textbf{Reaction Scheme 6}$$

$BaSO_4$ / $BaCO_3$ and PbI_2 were weighed and ground as previously. The mixtures were heated at 250 °C and 300 °C respectively before taking PXRD measurement as shown in fig 3.9 and fig 3.10. All the samples obtained are yellow. The main peaks in the pattern are attributed to PbI_2 (reveal at 2θ=12.7°) indicating that the synthesis has not been successful.

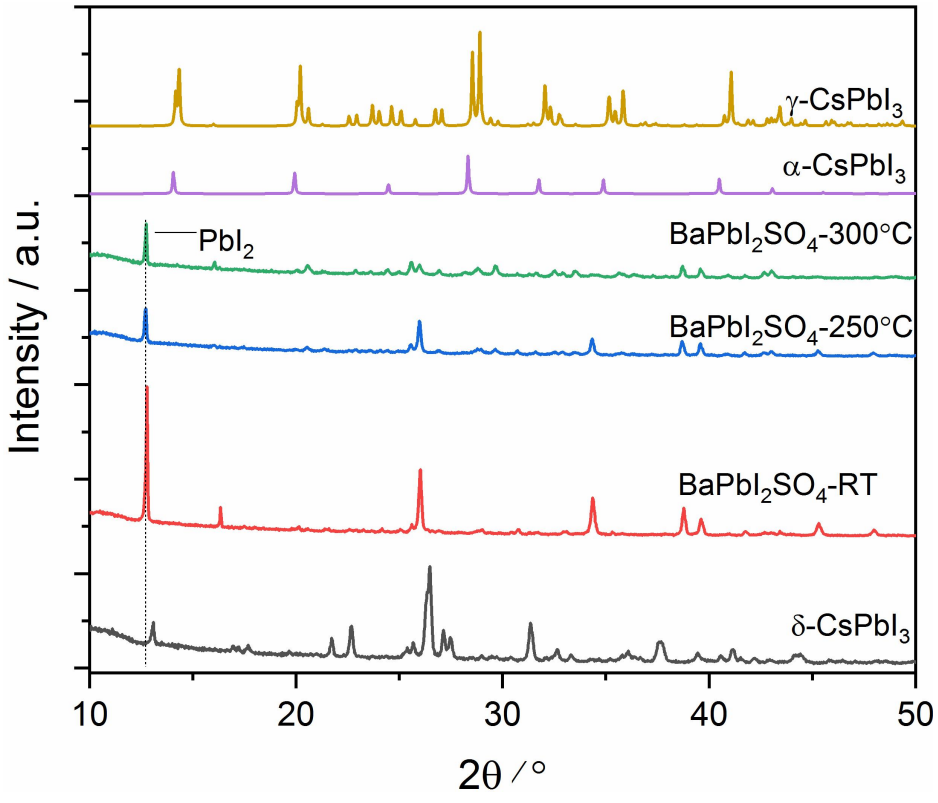

Fig. 3.9 PXRD pattern of $BaPbI_2SO_4$ heated at different temperatures. For comparison, the XRD pattern for δ-$CsPbI_3$, α-$CPbI_3$ and γ-$CPbI_3$ are also shown. (CuKα radiation 1.5418 Å)

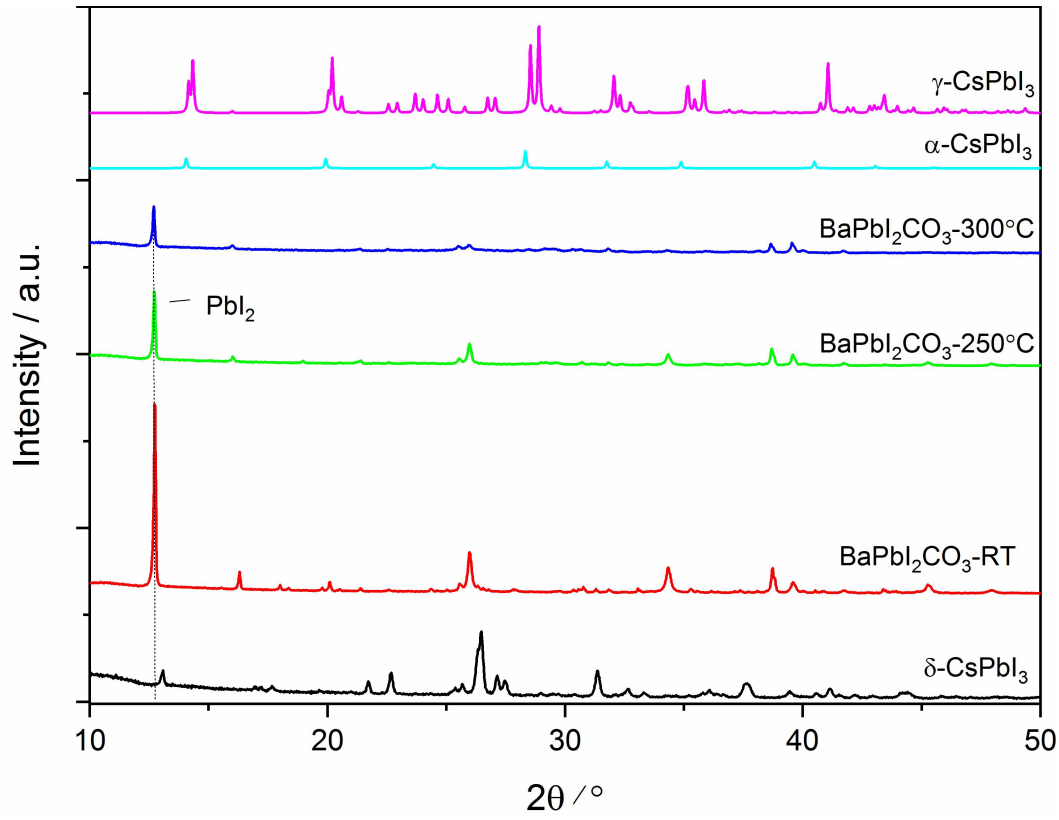

Fig. 3.10 PXRD pattern of $BaPbI_2CO_3$ heated at different temperatures. For comparison, the XRD pattern for δ-$CsPbI_3$, α-$CPbI_3$ and γ-$CPbI_3$ are also shown. (CuKα radiation 1.5418 Å)

3.4.3 X site doping

Doping on the anion site was then investigated. Br^- doping is proven to be an effective strategy to improve the stability in solution processed perovskites.[108] However, their stability has been mainly tested in a N_2 filled glove box, and so while work is needed to determinate whether they can tolerate ambient environment. To investigate it, 20%, 30% 40%, 50% and 100% of CsI was replaced by CsBr, and was milled with PbI_2, leading to a yellow mixture. Then, the samples were heated at 350 °C for 0.5h. When they were taken out from oven, 20% ($CsPbI_{2.8}Br_{0.2}$) doped sample was orange, while

other samples were dark black, indicating the formation of the cubic phase. However, the color of 30% doped sample ($CsPbI_{2.7}Br_{0.3}$) turned yellow in a few minutes.

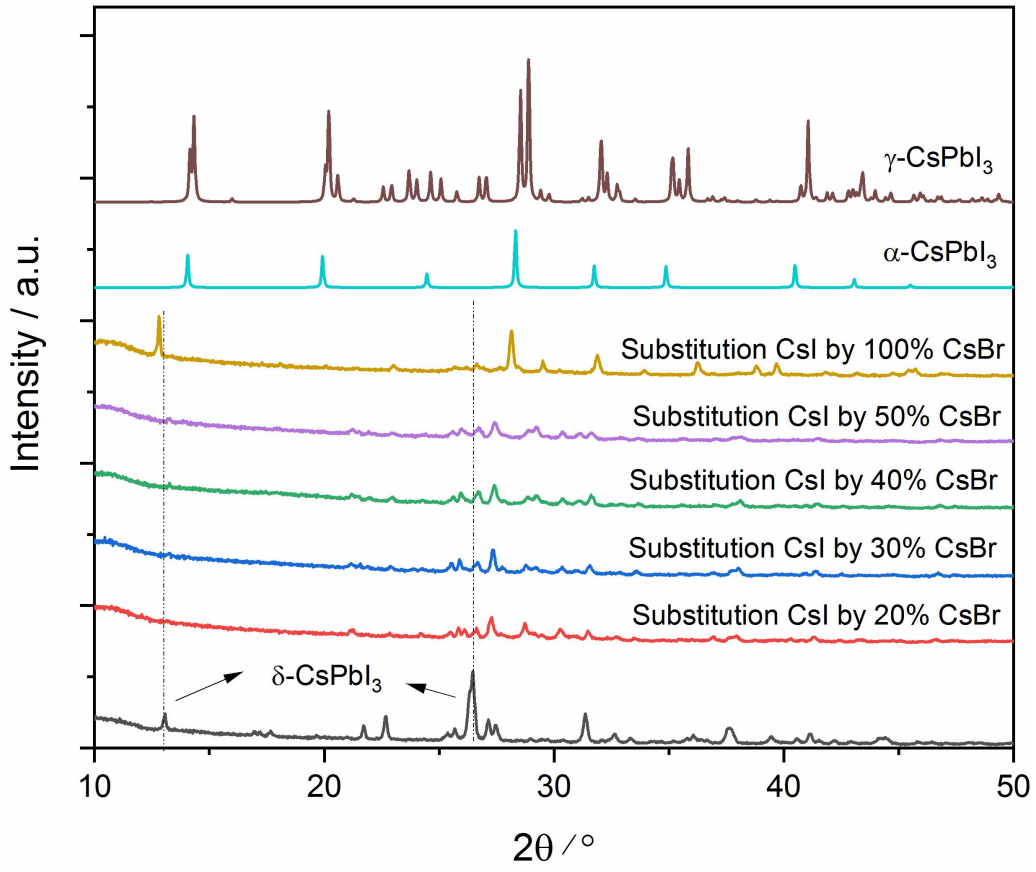

Fig. 3.11 PXRD pattern of $CsPbI_3$ with different amounts of CsI being substituted by CsBr. For comparison, the XRD pattern for δ-$CsPbI_3$, α-$CPbI_3$ and γ-$CPbI_3$ are also shown. (CuKα radiation 1.5418 Å)

The 40%, 50%, 100% doped samples turned from back to yellow again in less than 1 hour. The main peaks of yellow phase $CsPbI_3$ at 27.2 ° shifts to higher angle as doping concentration increases, indicating the successful doping of Br^-. However, the XRD pattern failed to give evidence of black phase because the serious phase transition problem. Thus, doping of CsBr is helpful for the formation of black phase perovskite,

but it isn't robust enough to remain stable in an ambient air environment for a long time because of various degradation factors such as humidity and light.

3.4.4 Organic cation doping on the A site

The doping of organic cations, such as MA^+ and FA^+ can reduce the transformation temperature to a black phase. At the same time, the volatile property of organic cations can have a negative influence on stability. So, low concentrations of organic cation doping might be a good choice to achieve stable black phase perovskite.

3.4.4.1 DMA^+

Dimethylammonium (DMA^+) has a radius size of 2.72 Å, which is similar to that of FA^+. Kanatzidis's group reported the forming of black phase $Cs_{0.7}DMA_{0.3}PbI_3$ using the solvent method in a glove box.[81] Moreover, the black phase transformation temperature is reduced to 100 ^oC. The relatively low doping concentration and moderate black phase transformation temperature makes DMA^+ a promising candidate for stabilizing $CsPbI_3$. Because the role played by solvent is unclear, we conduct the doping of DMA^+ both with and without dimethylformamide (DMF). CsI, DMAI and PbI_2 were weighted out with the ratio of 7:3:10. A few drops of DMF was added during the manual grinding into the mixture during the milling process. Then the samples were treated at 100 ^oC, 200 ^oC and 300 ^oC, respectively. All the samples obtained were yellow, indicating the absence of black phase. This was further confirmed by XRD measurements as shown in fig 3.12. We also tried doping without the use of solvent. The color of the samples remained in yellow after heating up to 350 ^oC.

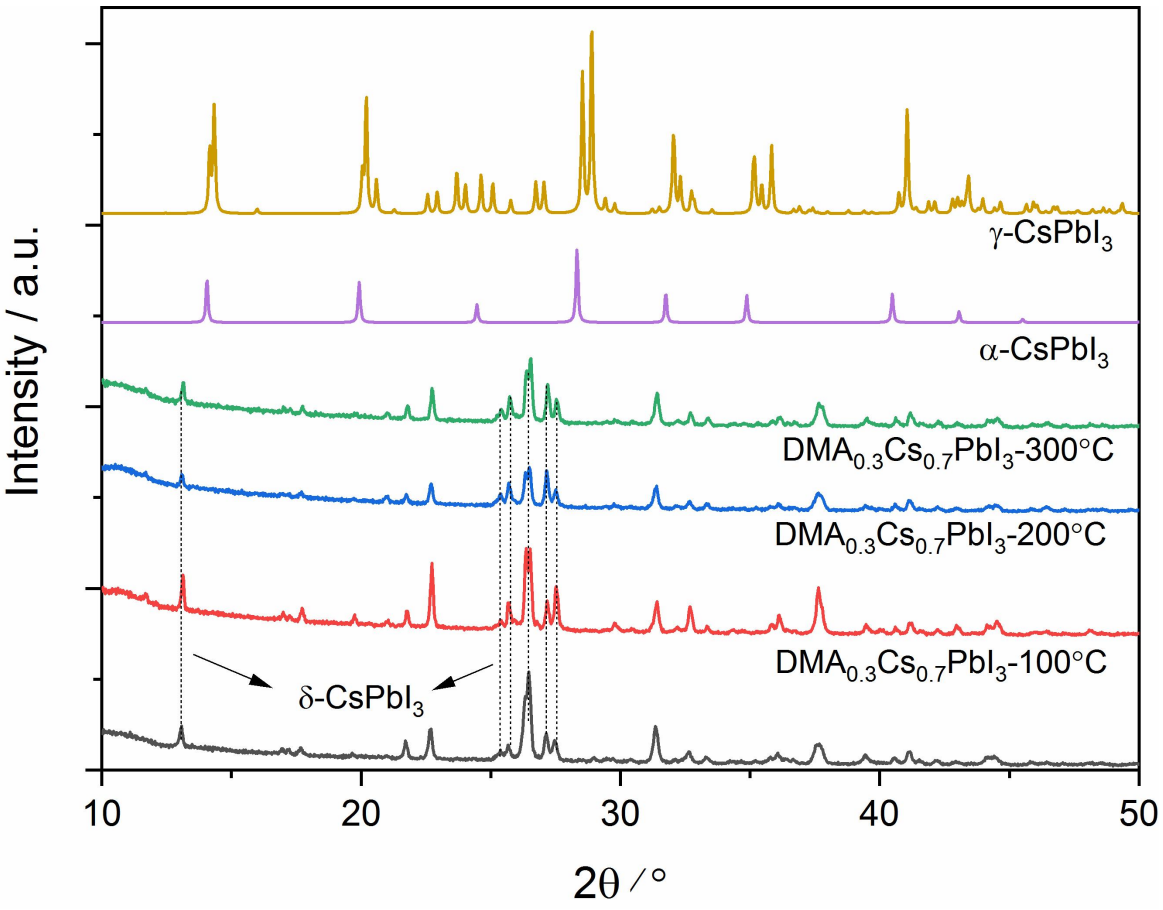

Fig. 3.12 PXRD pattern of $DMA_{0.3}Cs_{0.7}PbI_3$ prepared with DMF at different temperature. For comparison, the XRD pattern for δ-$CsPbI_3$, α-$CPbI_3$ and γ-$CPbI_3$ are also shown. (CuKα radiation 1.5418 Å)

2.4.4.2 EDA^+

Zhao's group reported that the ethylenediamine (EDA^+) cation can prevent the formation of theundesired yellow phase because of the appearance of a small amount of 2D perovskite EDA_2PbI_4.[109] $EDA_{0.1}Cs_{0.9}PbI_3$/ $EDA_{0.2}Cs_{0.8}PbI_3$ were synthesized by the previous solid chemistry route. However, the obtained mixture remained as the yellow phase after heating up to 200 °C. When the temperature was increased to 300 °C, the color changed into brown. The brown powder was carefully characterized by PXRD as shown in fig 3.13. The pattern is consistent with that of the undesired yellow

phase. So, the dark color might result from the carbonization of EDA. We verified this assumption by heating EDA, which is a white powder, up to 300 °C in the air, which gave a black powder.

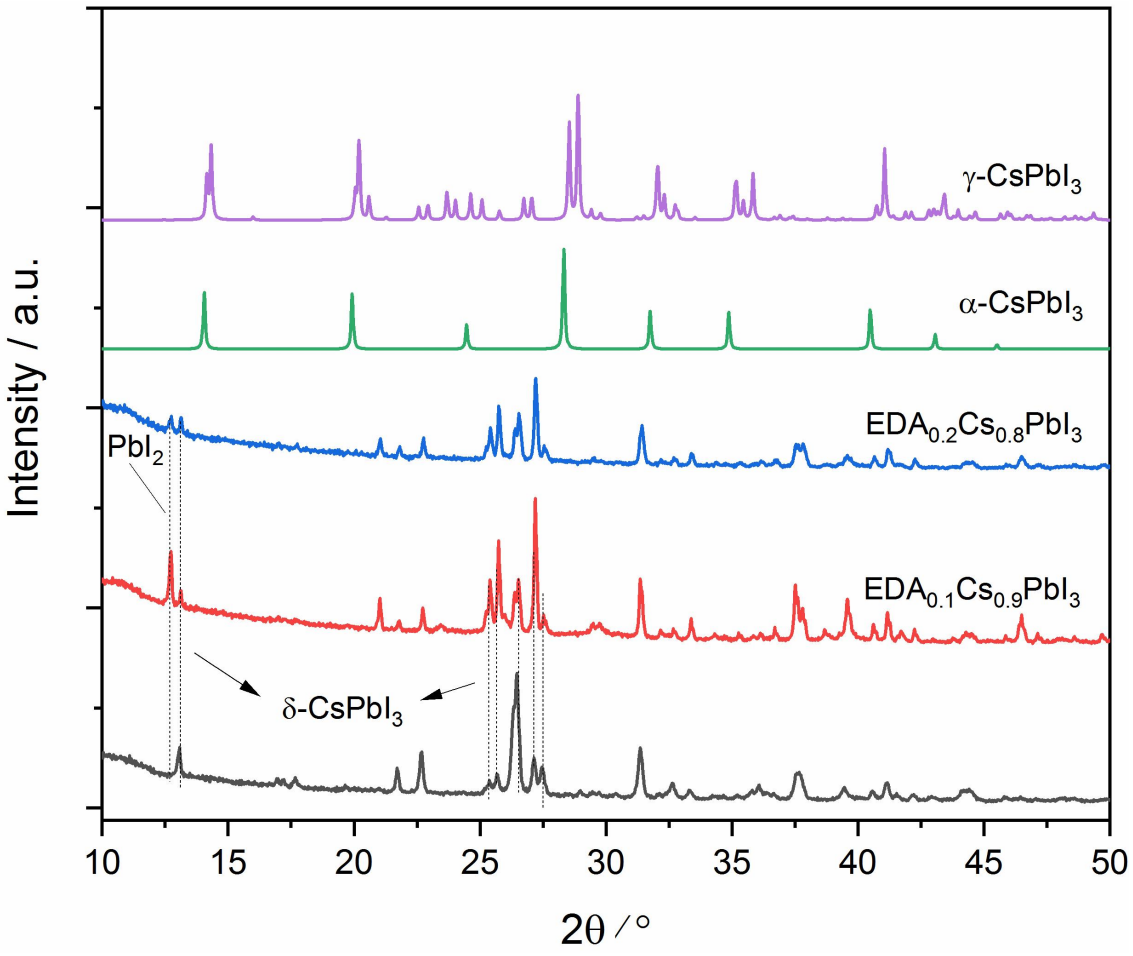

Fig. 3.13 Photographs and PXRD pattern of $EDA_{0.1}Cs_{0.9}PbI_3$/ $EDA_{0.2}Cs_{0.8}PbI_3$. For comparison, the XRD pattern for δ-$CsPbI_3$, α-$CPbI_3$ and γ-$CPbI_3$ are also shown. (CuKα radiation 1.5418 Å)

3.4.4.3 MA^+ / FA^+

The incorporation of 50% CsBr has been shown to improve the stability of $CsPbI_3$ to some extent in the last section. Therefore, we tried to further modify the composition by replacing the remaining 50% CsI with FAI/MAI as shown in Reaction Scheme 7:

$0.5CsBr+0.5\ FAI/MAI + PbI_2 \rightarrow MA_{0.5}Cs_{0.5}PbI_{2.5}Br_{0.5}\ /FA_{0.5}Cs_{0.5}PbI_{2.5}Br_{0.5}$

Reaction Scheme 7

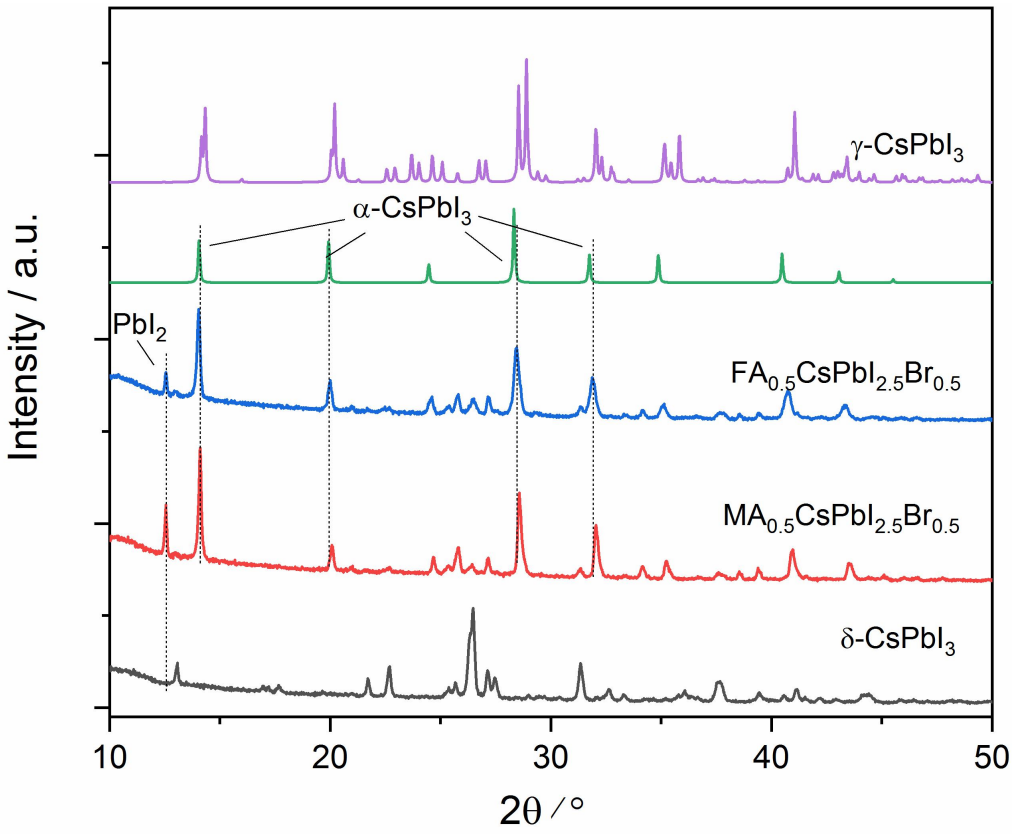

Fig. 3.14 XRD patterns of $MA_{0.5}Cs_{0.5}PbI_{2.5}Br_{0.5}$ / $FA_{0.5}Cs_{0.5}PbI_{2.5}Br_{0.5}$. For comparison, the XRD pattern for δ-$CsPbI_3$, α-$CPbI_3$ and γ-$CPbI_3$ are also shown. (CuKα radiation 1.5418 Å)

The color of MAI doped samples turned black immediately during the grinding, while the color of FAI doped sample was dark brown. Samples were heated at 350 °C for 0.5h. However, this temperature led to the carbonization or degradation of the organic cations. So, the temperature was reduced to 200 °C. After heat treatment, the color of MAI doping sample remained black, and the color of the FAI doped sample changed to black as well. PXRD measurements as shown in fig 3.14, confirms the cubic phase is the dominant composition with a small amount of yellow phase and remaining PbI_2.

Moreover, we can find that the peak of PbI_2 in the MA^+ containing sample is much stronger than that of FA^+ containing sample. This might be because MAI decomposes at 200 ^oC.

3.5 Conclusion

Although a lot of work has been reported on the successfully stabilization of $CsPbI_3$ with metal ions substitution in the glove box, the problem is still unsolved when it comes to the synthesis without solvent and the stabilization of $CsPbI_3$ in an ambient air environment. We find the incorporation of other metal cations such as Bi^{3+} and Mn^{2+} make little contribution to the stabilization of $CsPbI_3$ for the synthesis in the air. Some of the dopants seem to aid the formation of yellow phase at lower temperature and accelerate the decomposition of yellow phase into CsI and PbO at high temperature. Br^- doping can stabilize $CsPbI_3$ in air only for a few minutes to an hour, which lead to some observation of cubic phase in the PXRD pattern. Interestingly, a cubic phase dominant black powder can be obtained by the synergic contribution of Br^- and MA^+/FA^+ cations. However, there are still several issues left to be answered in the future. For example, the confirmation of successful doping of MA^+/FA^+ by other methods, such as nuclear magnetic resonance (NMR) and Auger electron spectroscopy (AES). Moreover, it meaningful to find out the lowest doping concentration of MA^+/FA^+ to maintain the black phase, aiming to reduce the usage of organic cations because of their poor thermal stability.

4. Degradation induced lattice anchoring self-passivation in $CsPbI_{3-x}Br_x$

This work is in this chapter has been published in *J. Mater. Chem. A*.

Submitted: 24th February 2020

Accepted: 30th April 2020

Information: J. Mater. Chem. A, 2020, 8, 9963 DOI: 10.1039/d0ta02210a

Authors: Jingwei Xiu, Bo Dong, Elizabeth Driscoll, Xiyuan Feng, Abubakar Muhammad, Shaoqing Chen, Zheng Du, Yudong Zhu, Zheng Zhang, Zhaoheng Tang, Zhubing He* and Peter Raymond Slater*

Author contributions: J. X., Z. H., and P. R. S. conceived the idea and wrote the manuscript. J. X., B. D., E. D., and A. M. collected the XRD data and performed the structural refinements. J. X. synthesised all the materials and performed the initial characterisation measurements and stability studies. X. F., Z. Z., and S. C. contributed to the TEM and EDX measurements. Z. D, Y. Z., and Z. T. contributed to the data analysis. Z. H. and P. R. S. supervised this project.

Highlights

The all-inorganic halide perovskite ($CsPbI_3$) holds promise for photovoltaic applications but suffers from a detrimental phase transformation to a non-perovskite phase δ-$CsPbI_3$ at low-temperature. Of the different perovskite polymorphs, there has been a wide range of studies on *γ*-$CsPbI_3$ due to its kinetic stability at near room-temperature. However, synthesis routes to this and other all-inorganic halide perovskites are still not ideal, requiring uneconomical elimination of humidity as well

as quenching from elevated temperature. Water/moisture is commonly meticulously avoided due the fact that it can accelerate the detrimental degradation of the perovskite. In our synthesis, we used an alternative approach of engineering an in situ degradation process to form a dual-functional PbI(OH) protective covering and succeeded in performing the first room-temperature synthesis of *γ*-$CsPbI_3$ under ambient humidity. The vastly improved stability benefits from both lattice anchoring and physical coverage of *γ*-$CsPbI_3$ by an ultra-thin PbI(OH) layer. The resultant γ-$CsPbI_3$ is stable for more than 2 months under ambient conditions (25 ^oC, RH 30–60%) and more than 12 hours at 175 ^oC in air without any degradation. Furthermore, we show that this novel facile method can be successfully applied to mixed halide perovskites such as $CsPbI_2Br$, and this has allowed the first experimental synthesis of the *γ*-polymorph of $CsPbI_2Br$. Thus, our work provides an efficient degradation-induced lattice-anchoring self-stabilization strategy and a new avenue to the economical synthesis of all-inorganic perovskite materials at room-temperature under ambient conditions.

4.1 Introduction

Organic-inorganic halide perovskites have attracted tremendous attention in the past decade because of their good photovoltaic performance.[110-112] However, the thermal instability resulting from the volatile nature of the organic cations (e.g., $CH_3NH_3^+$) impedes their development towards commercialization.[113,114] All-inorganic perovskites, realized by replacing the unstable organic cations with inorganic Cs^+, are promising candidates for more stable perovskite solar cells.[115] Unfortunately, *α*-$CsPbI_3$ is only stable above 325 ^oC because of the structural instability of the perovskite resulting

from the smaller size of Cs^+ cation.[2] It is firstly converted into the low-temperature β/γ perovskite phase and then to non-perovskite δ-$CsPbI_3$ finally at room-temperature as shown in fig 4.1.[2, 43, 44, 116] This phase instability of $CsPbI_3$ has attracted considerable interest in the development of strategies to achieve the formation of these low-temperature photoactive *β*/*γ* perovskite phases, particularly the γ phase.[44, 117] Single crystals of *γ*-$CsPbI_3$ have been grown via a solid-state method through quenching with a strict control over humidity. [71] Thin-films of *γ*-$CsPbI_3$ have also been widely studied in recent years.[71, 118-120] In order to reduce the synthesis temperature, HI has been introduced for the preparation of the γ-$CsPbI_3$ film so as to decrease the annealing temperature for *γ*-$CsPbI_3$ to 100ºC.[117] More recently, co-evaporation of CsI and PbI_2 onto the substrate has allowed a lower temperature annealing of 50 ºC.[120] However, the preparation of *γ*-$CsPbI_3$ at room-temperature, especially in an ambient environment (with its' associated humidity challenges), has not been reported previously. To this end, we have been examining the possibility to synthesize this phase via a solution route. Such solution-processed perovskites have various merits such as the potential commercial benefits of low-cost room-temperature preparation and scale-up. Nevertheless, this approach is not without its' challenges, especially for the preparation of *γ*-$CsPbI_3$ because of the greater inherent thermodynamic stability of the undesirable non perovskite *δ*-$CsPbI_3$ product. In particular, the presence of moisture or heating is known to accelerate the phase transformation into *δ*-$CsPbI_3$.[4, 120] Various strategies, such as reducing grain size, and composition engineering have been examined to improve the stability.[105, 119, 121] However, these routes entail their own issues, such as the introduction of potentially undesirable defects and the consequent influence on the band gap of the perovskite. Other potential strategies

include surface passivation strategies, such as via ligand passivation, which show some promise, although the uniformity and compactness of any resultant passivation layer remains a challenge to be addressed.[122]

In view of these challenges, our aim was to find a feasible solution-processed approach to prepare this all-inorganic perovskite at room-temperature in air to kick-start future advanced applications of this material (fig 4.1). We aimed to address the issue of relying on uneconomic dry synthesis environments, by designing in a surface degradation process that would lead to a uniform growth of a surface passivation layer, which would be expected to provide a high-quality surface protection coverage while preventing uncontrolled degradation throughout the particles. In our thoughts behind this strategy, we were drawn to the degradation reaction of *γ*-$CsPbI_3$ towards water, which is a universal problem for perovskite, and has led researchers to naturally avoid its' presence for the preparation of these perovskite phases. Our approach was to try to utilize this process to provide a surface degradation layer to passivate further degradation. The challenge is to achieve a uniform passivation layer, which lattice matches to the perovskite in order to prevent delamination creating fresh surface. As a common example, iron readily rusts, due to the fact that the corrosion product delaminates creating fresh surface, while Al is kinetically stabilized by a surface layer of the oxide which protects the metal from further corrosion. The aim to stabilize *γ*-$CsPbI_3$ therefore is to create a lattice matched surface decomposition product to provide a similar protective layer. In particular, it is known that water can degrade these perovskite systems, and so we explored solution routes containing water to examine whether we could induce and then cap this degradation process to form a stable protective layer.

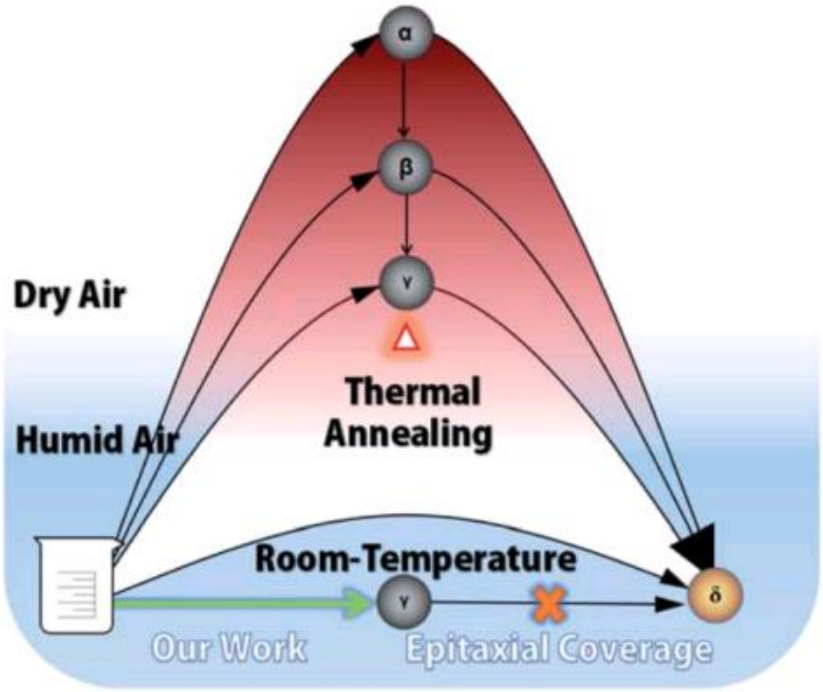

Fig 4.1 Synthesis processes and phase relations of $CsPbI_3$ in dry/humid air at low/high temperature.

4.2 Design and result

We report this new solution processed preparation route to stable *γ*-$CsPbI_3$ at room-temperature under ambient environment. By controlling the degradation process of perovskite with the presence of water, an ultra-thin single-crystalline PbI(OH) epitaxial shell is grown on the surface of *γ*-$CsPbI_3$ micro-crystals assisted by the presence of acetate and PVP. This in-situ produced PbI(OH) passivation shell provides a dense protective coverage to the perovskite, resulting for the first time in both excellent thermal stability and moisture stability of *γ*-$CsPbI_3$ in air. This method has also been successfully applied to $CsPbI_2Br$ and has allowed the preparation of the low-temperature *γ*-$CsPbI_2Br$ phase for the first time.

4.3 Synthesis

γ-$CsPbI_3$/$CsPbI_3$@PbI(OH): 2 mmol cesium iodide was dissolved in 10 ml methanol/water (vol 9:1). 0.5mmol lead acetate trihydrate was dissolved in 10ml methanol. For the preparation of $CsPbI_3$@PbI(OH), 400ul Pb^{2+} precursor solution was added into a vial with 4 ml ethanol. Ethanol is used as an anti-solvent, in order to accelerate the precipitation of the perovskite, by changing the polarity of the solvent system. The absence of ethanol leads to rapid degradation of the black phase in a few seconds owing to the strong polarity of water and methanol. *γ*-$CsPbI_3$ was obtained when 300ul Cs^+ precursor solution was injected. Stable $CsPbI_3$@PbI(OH) is obtained by addition of 200 mg PVP 4000 closely following the formation of γ-$CsPbI_3$. The $CsPbI_3$@PbI(OH) is washed with ultra-dry isopropanol (IPA) and dried in air naturally. Note: Ultra-dry solvent is not required during the synthesis and is only used for washing after synthesis.

γ-$CsPbI_2Br$/$CsPbI_2Br$@PbI(OH): $CsPbI_2Br$ was synthesized by substituting 1/3 mole ratio of CsI with CsBr. $CsPbI_2Br$@PbI(OH) was then obtained with the same method as for the preparation of $CsPbI_3$@PbI(OH).

4.4 Characterization and Discussion

4.4.1 Growth of γ-$CsPbI_3$

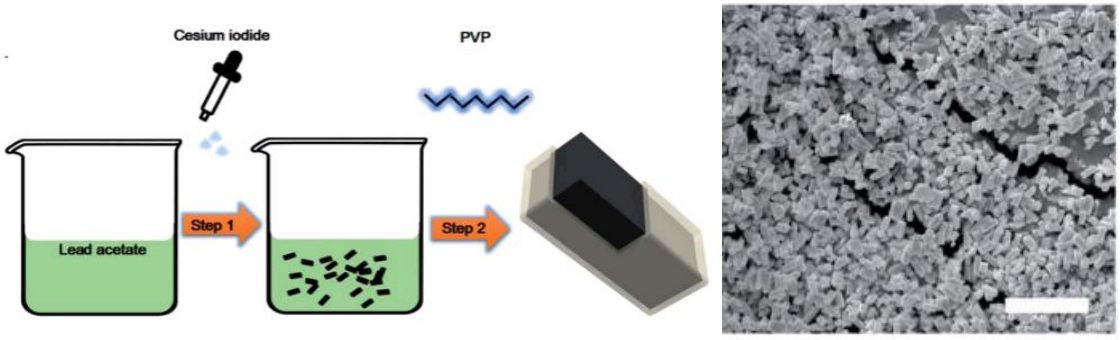

Fig 4.2 Schematic diagram for the preparation of $CsPbI_3$@PbI(OH). (left) SEM image of $CsPbI_3$@PbI(OH) on conductive carbon adhesive. Scale bar: 10 mm. (right)

Through our new approach, *γ*-$CsPbI_3$ is directly prepared via a solution route at room-temperature in an ambient environment even in the presence of high humidity, bypassing the previous need to quench high-temperature *α*-$CsPbI_3$ to obtain this phase. The perovskite is then further self-stabilized by surface degradation to prevent the conversion into the undesired non-perovskite phase *δ*-$CsPbI_3$ (Fig 4.1). When the Cs^+ and Pb^{2+} precursor solutions are added into ethanol, a black colloid appears immediately through a simple one-step reaction as shown in fig 4.3 and equation 4.1.

$$3CsI + Pb(CH_3COO)_2 \rightarrow \gamma\text{-}CsPbI_3 + 2Cs(CH_3COO) \qquad \textbf{equation 4.1}$$

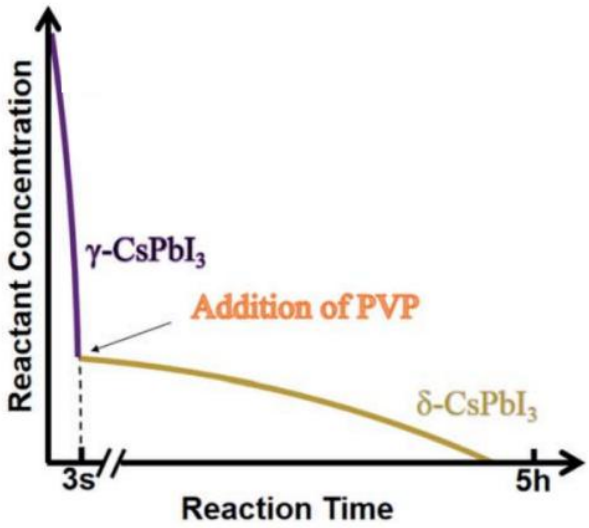

Fig 4.3 The precipitation of *γ*-$CsPbI_3$ and *δ*-$CsPbI_3$ vs. time. The addition of PVP is suggested closely following the formation of *δ*-$CsPbI_3$.

As in the prior method of rapid quenching from high temperature to "freeze in" the desired *γ*-$CsPbI_3$,[123] in our method, a similar rule is obeyed in that high reactant concentration and a rapid precipitation process, which is completed in seconds, is required to produce high quality *γ*-$CsPbI_3$ (fig 4.3) while low concentration and slow reaction speed results in significant amounts of the undesired *δ*-$CsPbI_3$ phase. Yellow phase *δ*-$CsPbI_3$ is observed from the residual reactant over a few hours after the rapid formation of the black phase *γ*-$CsPbI_3$ perovskite in our experiment. The novelty of our approach is that the reaction is performed both at room temperature and in the presence of water, with this route leading to the growth of a protective PbI(OH) lattice anchored shell coating the $CsPbI_3$ particles. The challenge, however, remained to block the concomitant growth of undesired *δ*-$CsPbI_3$, due to continued degradation, and so PVP was added to the solution after the formation of *γ*-$CsPbI_3$ to cap the degradation process as shown in step 2 in fig 4.4.

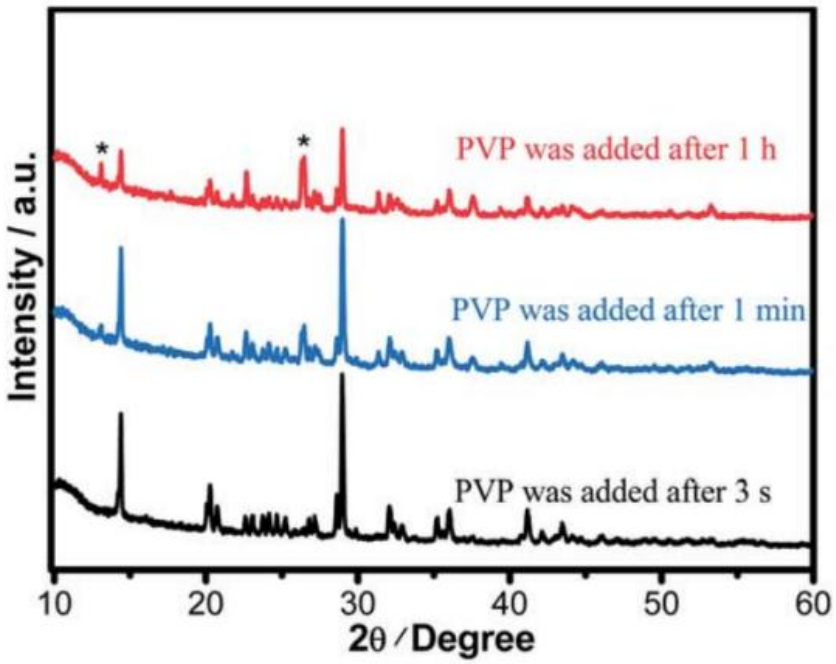

Fig 4.4 PXRD patterns of $CsPbI_3$@PbI(OH) prepared with PVP added after different time intervals. Peaks from *δ*-$CsPbI_3$ are marked with *.

We investigated addition of PVP during different times in the synthesis. The results showed that when PVP was added 1h after the initial formation of black phase γ-$CsPbI_3$, strong peaks from undesired *δ*-$CsPbI_3$ appeared in the powder X-ray diffraction (PXRD) patterns (fig 4.4); However, when PVP is added within 1 min, the intensity of the peaks from δ-$CsPbI_3$ are diminished. Furthermore, when PVP is added immediately (within 3s), peaks belonging to *δ*-$CsPbI_3$ can be avoided. The results therefore show that the addition of PVP is efficient in eliminating the gradual growth of δ-$CsPbI_3$. Structure refinement using PXRD data at room temperature confirms the formation of the orthorhombic *Pbnm* (no.62) structure of *γ*-$CsPbI_3$ with lattice parameters *a* = 8.579(1) Å, *b* = 12.472(1) Å, and *c* = 8.867(1) Å as shown in fig 4.5,

which are in agreement with previous reports.[117] For the refinement of $CsPbI_3$, We used a reported *γ*-$CsPbI_3$ structure file as a starting model. We allowed the variation unit cell parameters during the refinement to check whether our $CsPbI_3$ is same to the reported room-temperature *γ* phase. Experimental $CsPbI_3$@PbI(OH) pattern has strong perfected orientation, which cannot be solved by milling the sample, because of the damaging of protective shell during milling would result into the quick degradation of perovskite. After taking the preferred orientation into consideration during refinement, we got a good refinement result with 'R-weighted pattern' (wR) to be 6.18% as shown in table 4.1.

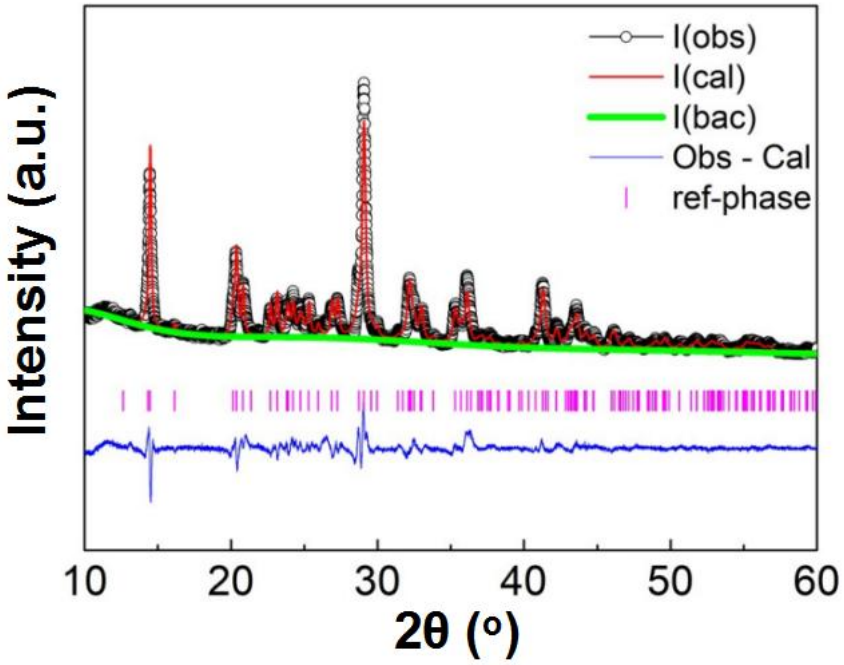

Fig 4.5 Observed, calculated and difference profiles for $CsPbI_3$@PbI(OH) from Rietveld refinement of the structure using powder XRD data. (Wavelength of X-Ray beam: 1.5418 Å)

Table 4.1 Refined structural parameters for $CsPbI_3$@PbI(OH).

Atom	*x*	*y*	*z*	Mult.	Occupancy	u_{iso}×100 (Å^2)
Pb1	0	0	0	4	1	1.7(1)
Cs1	0.4459(5)	0.25	0.0153(6)	4	1	3.6(2)
I1	0.5091(6)	0.25	0.5645(5)	8	1	2.2(2)
I2	0.1959(3)	0.0273(3)	0.3103(3)	4	1	0.9(1)

a = 8.867(1)Å, *b* = 12.472(1)Å, *c* = 8.579(1)Å, V = 948.80(7)Å^3

GOF = 2.17, wR = 6.18%

4.4.2 Formation of PI(OH)

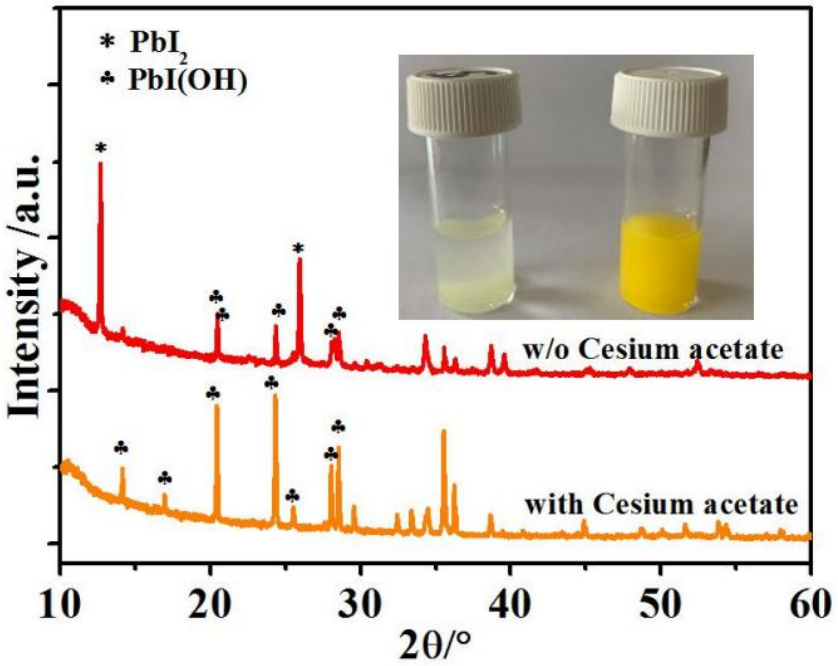

Fig 4.6 PXRD pattern of $CsPbI_3$ degraded by water with/without the presence of cesium acetate. Inset: digital photograph of the corresponding degraded products.

The key to the success of this route is the control of the degradation process to ensure both the formation and epitaxial growth of the PbI(OH) lattice anchoring shell. Here, we discuss why PbI(OH) is formed rather than other reported degradation products,

such as PbI_2.[113, 124] In particular, we believe that the acetate ligand from the precursor is important to ensure the one-step surface degradation of perovskite into pure PbI(OH). To prove this postulate, black colloids of *γ*-$CsPbI_3$ synthesized without PVP were isolated from the mother liquor and re-dispersed in 2ml ethanol with/without cesium acetate in order to study the role of acetate ligand during the degradation process. To initiate degradation, water was then added to both, which resulted in complete decomposition of the black colloids within 5 minutes. Interestingly, a pale-yellow product was formed with the presence of cesium acetate, while a yellow compound was obtained without cesium acetate, as shown in fig 4.6. The pale yellow and yellow products were confirmed to be pure PbI(OH) and the mixture of PbI(OH) and PbI_2, respectively. Thus, with the presence of acetate ligand, pure PbI(OH) is formed in one-step as shown in equation 4.2.

$$\gamma\text{-}CsPbI_3 + Cs\,(CH_3COO) + H_2O \rightarrow PbI(OH) + 2CsI + CH_3COOH \quad \textbf{equation 4.2}$$

In comparison, both PbI_2 and PbI(OH) appear from the degradation of the perovskite with the absence of the acetate ligand. We believe that the rapid formation of pure PbI(OH) is essential for the formation of a dense epitaxial shell, and that the acetate ligand works though influencing the pH of the solution, as it has been reported in the literature that PbI(OH) can be obtained from lead acetate when the pH is above 7, while PbI_2 is produced when the pH is reduced to 7 or below.[125] The subsequent addition of PVP is also crucial to cap the degradation process and ensure the formation of a uniform, dense high-quality PbI(OH) protective shell. This is illustrated by the fact that performing the synthesis of $CsPbI_3$, without adding PVP, leads to a

product that turns yellow (conversion to δ-$CsPbI_3$) once dried in air. Nevertheless, once formed in the presence of PVP and separated from solution, the $CsPbI_3$@PbI(OH) remains stable in ambient conditions even after removal of the PVP by washing with isopropanol (see later). It has been reported that the C=O group in PVP interacts with the $CsPbI_3$ surface.[21] Therefore, there is expected to be an initial chemical interaction between the fresh $CsPbI_3$ surface and PVP as it is added into the reaction. As the perovskite surface degrades due to interaction with water into PbI(OH), this initial interaction will be broken. Instead, the PVP will be absorbed again on PbI(OH) layer coordinating to the OH group, which might be expected to be a stronger interaction, and so hard to be totally removed by the washing process. The role of this surface absorbed PVP is mostly likely to be limiting the speed of degradation process and helping to contribute to the uniformity of PbI(OH) shell.

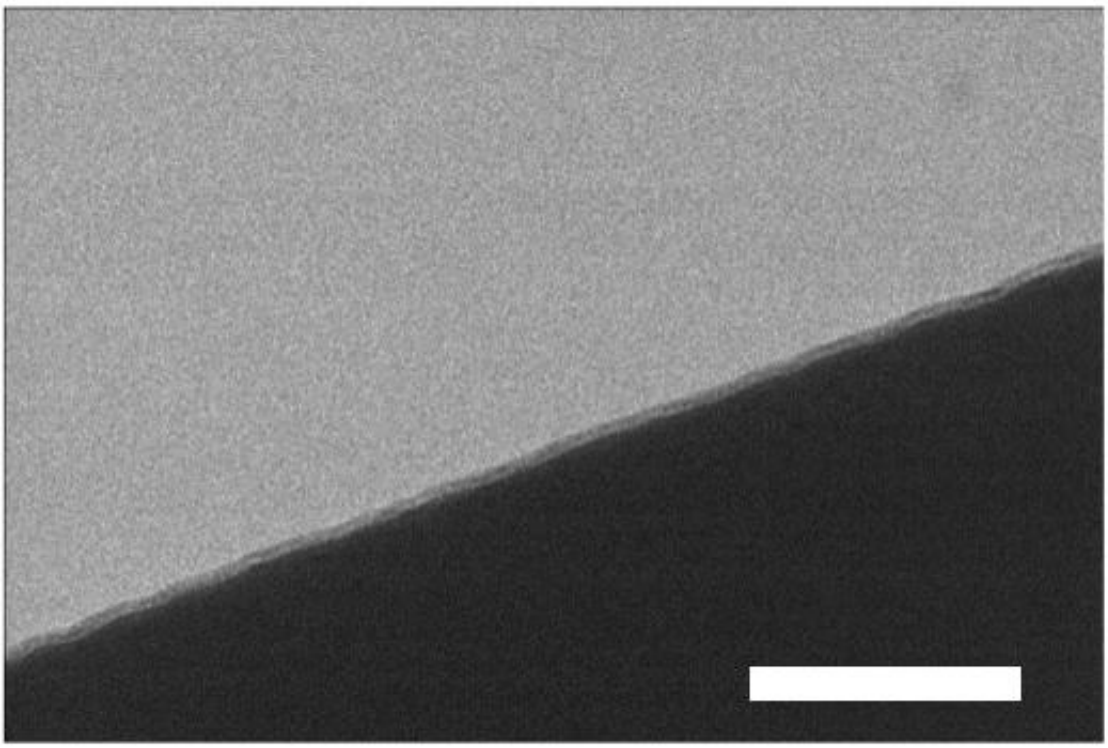

Fig 4.7 TEM image of the PbI(OH) layer (scale bar: 100 nm).

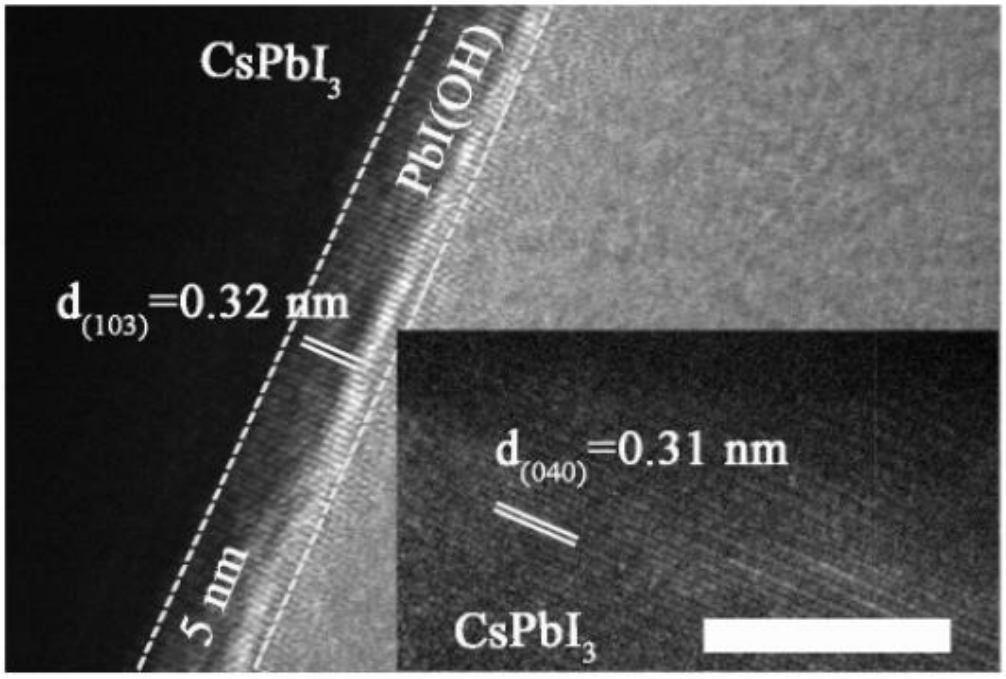

Fig 4.8 TEM image of the PbI(OH) layer and perovskite (scale bar: 100 nm).

In order to confirm the formation of a protective shell of PbI(OH), we carried out high-resolution transmission electron microscope (HRTEM) measurement to characterize this shell. The results showed that the shell is uniform and forms a continuous surface as shown in fig 4.7. HRTEM images of bulk perovskite shows the separation of the (040) planes with the spacing of 3.1 Å (fig 4.8). In the PbIOH shell, the HRTEM shows the separation of the similarly aligned (103) planes with lattice spacing of 3.2 Å, leading to small size mismatch of about 2.9% with the perovskite phase, and thus suggesting an epitaxial growth of the degradation layer.[126] Representations of these lattice planes are shown in fig 4.9 illustrating good match between the lattices.

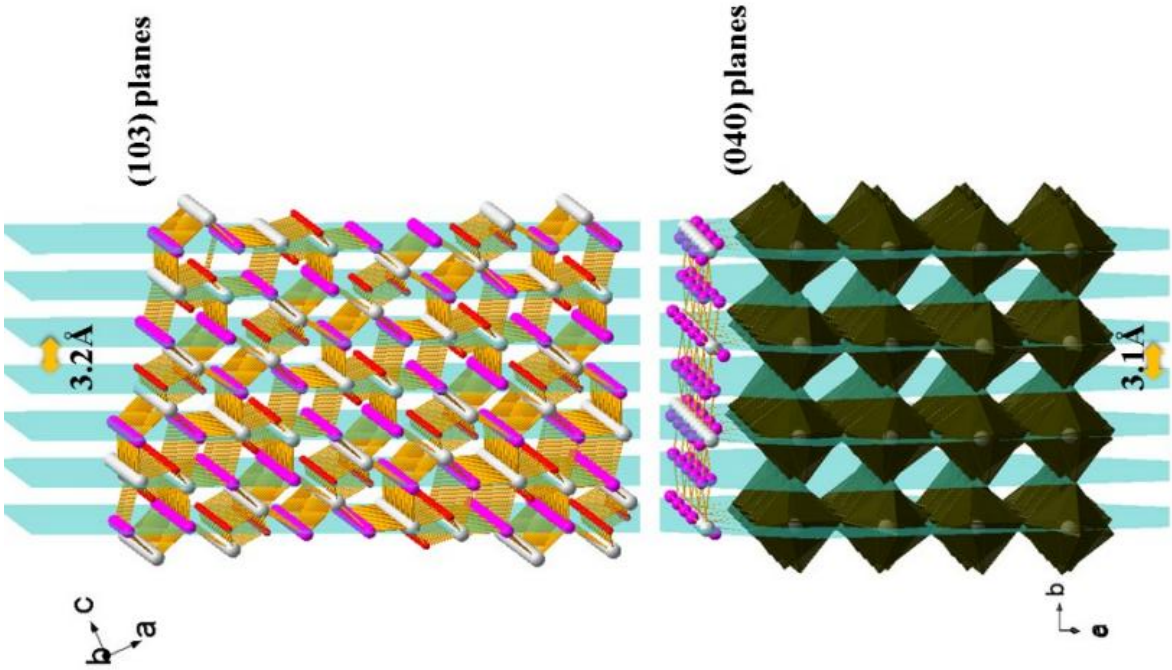

Fig 4.9 Atom distributions in (103) planes of PbI(OH) and (040) planes of perovskite. White: lead, Purple: Iodide, Red: Oxygen. A layer of atoms of perovskite presented in ball-and-stick model is shown at the interface between PbI(OH) and $CsPbI_3$.

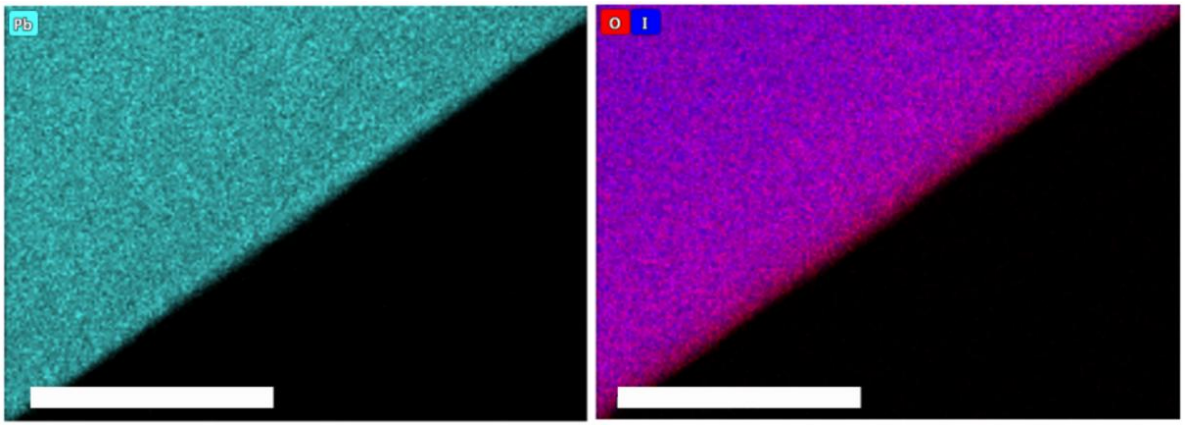

Fig 4.10 STEM-EDX map of $CsPbI_3$@PbI(OH). Left: map of Pb. Right: stacked map of O and I elements (red: O, blue: I, cyan: Pb). Scale bar: 100 nm.

The growth of the PbI(OH) layer was further investigated by energy dispersive X-ray (EDX) in the scanning transmission electron microscope (STEM). The PbI(OH) layer can be distinguished by STEM-EDX mapping of the Pb element because of the different Pb density in PbI(OH) compared to $CsPbI_3$ as shown in fig 4.10. The stacked mapping of elements O and I reveals a O-rich area at the edge of the crystal, corresponding to the PbI(OH) shell.

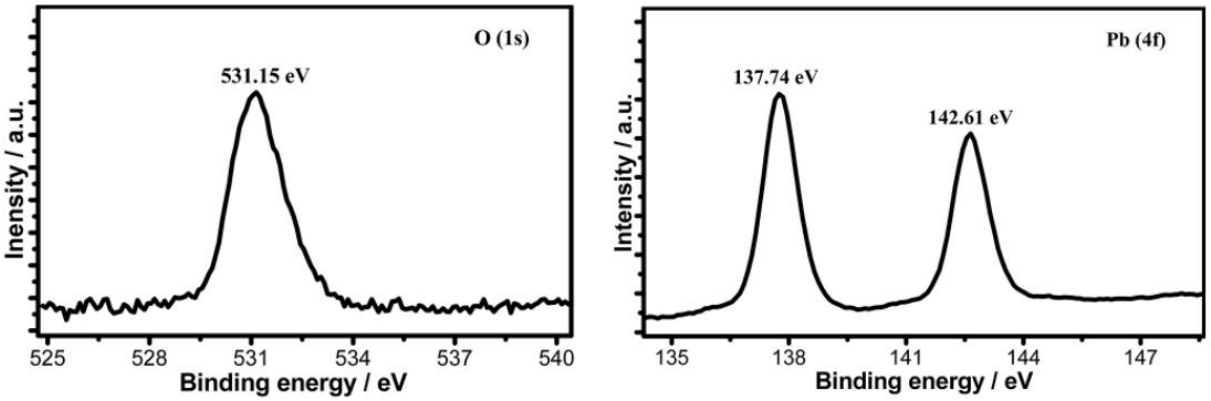

Fig 4.11 X-ray photoelectron spectrum of $CsPbI_3$@PbI(OH).

The $CsPbI_3$@PbI(OH) particles were further characterized by X-ray photo-electron spectroscopy (XPS) measurement. The XPS signal at the bonding energy of 531.15 eV, corresponding to the featured peak of O in a metal hydroxide, is assigned to PbI(OH). The Pb 4f signal in this PbI(OH) surface layer is observed at the bonding energy of 137.74 eV, while the absence of a Pb 4f signature peak belonging to $CsPbI_3$ at 137.30 eV, indicates that the surface coverage is compact so that there is no perovskite phase exposed as shown in fig 4.11.[119] Thus, these XPS results further provide strong evidence for the uniform coverage of the perovskite by the PbI(OH) shell. Elemental analysis through XPS shows an approximately 1:1 ratio of O atoms to I atoms (I:O=1.08:1), which supports the presence of a PbI(OH) shell.

4.4.3 Stability

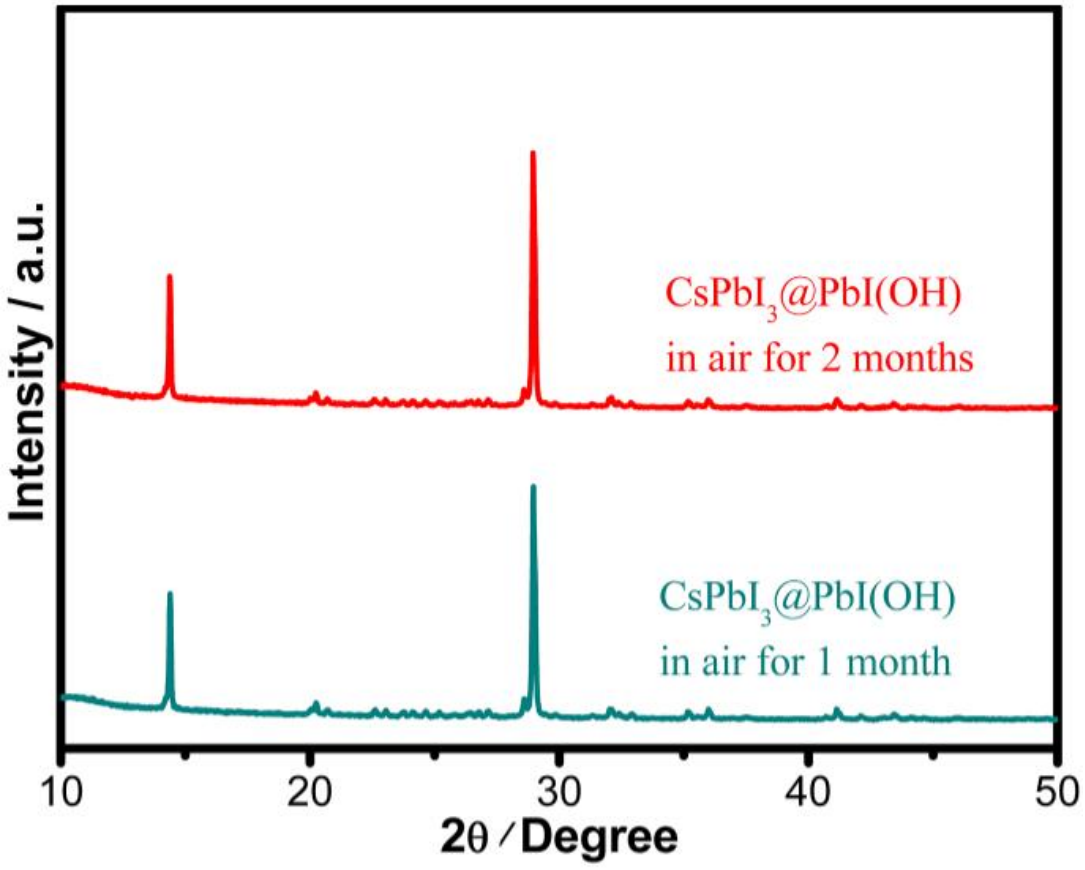

Fig 4.12 PXRD measurement of $CsPbI_3$@PbI(OH) stored in air.

In order to probe the stability in air of these $CsPbI_3$@PbI(OH) particles, and confirm the protective nature of the PbI(OH) shell, all samples that underwent stability testing underwent washing with ultra-dry isopropanol for three times to remove PVP. Significantly, even after removal of the PVP, PXRD shows that $CsPbI_3$@PbI(OH) doesn't show any degradation after keeping in ambient air (RH=30-60%) for more than 2 months as shown in fig 4.12.

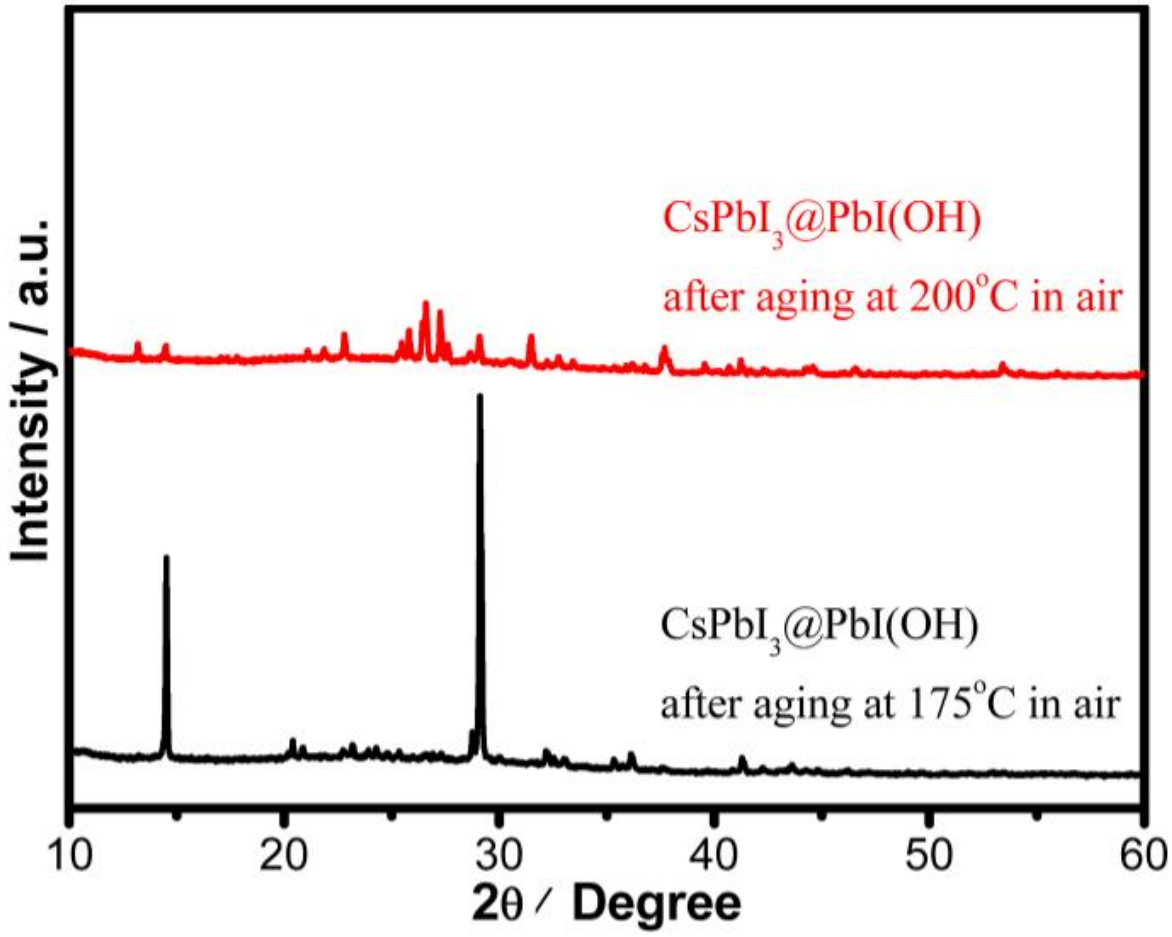

Fig 4.13 PXRD patterns of $CsPbI_3$@PbI(OH) aged at diffffferent temperatures in air showing stability up to 175 °C.

Furthermore, it shows no degradation after heating at 175 °C for 12h in air with environmental relative humidity of 60% as shown in fig 4.13. At higher temperatures (200°C), it does transform to δ-$CsPbI_3$, which can be attributed to the dehydration and hence decomposition of the PbI(OH) surface layer.[125]

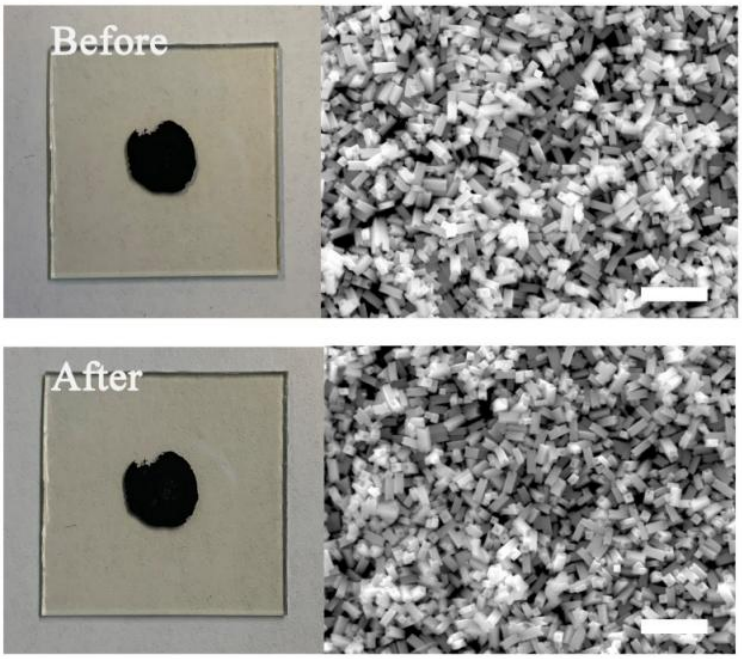

Fig 4.14 Digital photos and SEM images of $CsPbI_3$@PbI(OH) before and after stability test (heating at 175°C in air for 12h) .

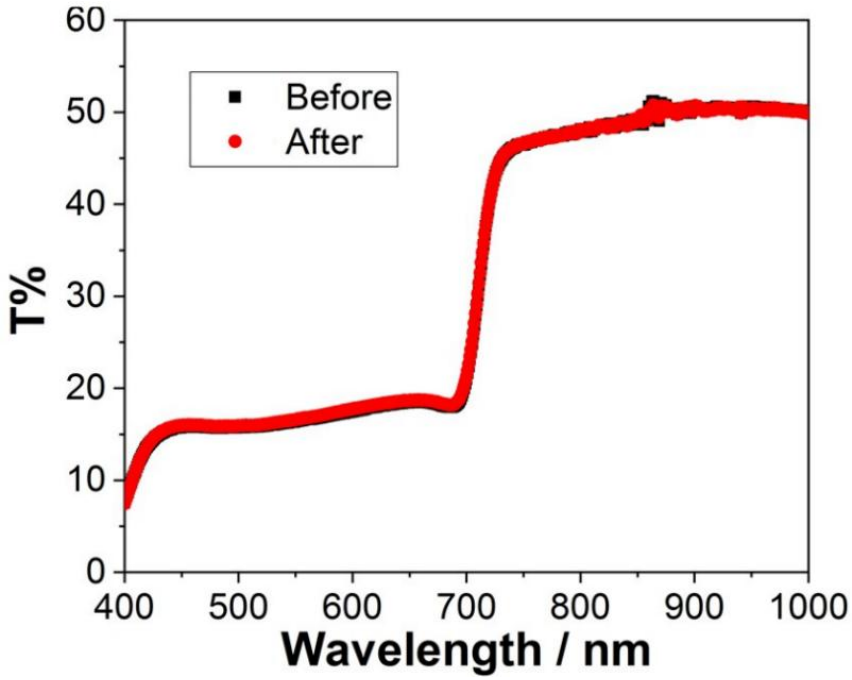

Fig 4.14 UV-Vis transmitance analysis of $CsPbI_3$@PbI(OH) film before and after stability test. The film was fabricated by spin-coating $CsPbI_3$@PbI(OH).

To further prove its excellent stability, we recorded the digital photos, SEM images and UV-Vis transmittance spectra of the sample before and after heating in air at 175 ^{o}C for 12h as shown in Fig 4.13. These showed no obvious changes triggered by degradation can be observed before and after storage as shown in fig 4.14 and 4.15.

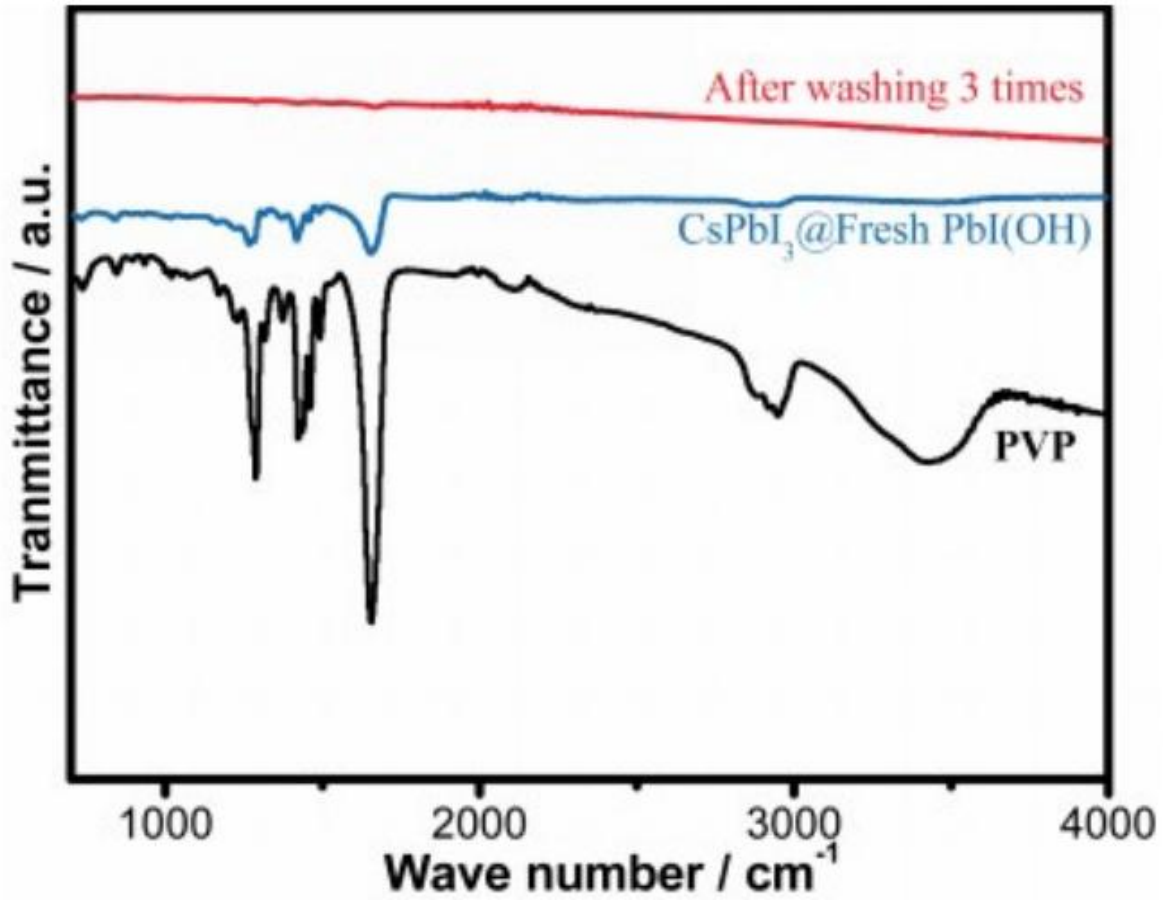

Fig 4.15 Fourier Transform Infrared Spectrum (FTIR) spectrum of PVP and *γ*-$CsPbI_3$@PbI(OH) before and after washing with isopropanol, showing removal of the PVP.

The samples were washed carefully for three times to remove residual PVP, confirmed by FTIR as shown in fig 4.15. It reveals that the origin of the improved stability is due to the PbI(OH) shell, rather than other factors, such as PVP coverage.

Rather the PVP is there to cap the initial degradation process and ensure a uniform surface coverage is obtained. Thus, our results show that this new synthesis method is efficient in the stabilization of micron-sized particles of *γ*-$CsPbI_3$ towards both moisture and heating.

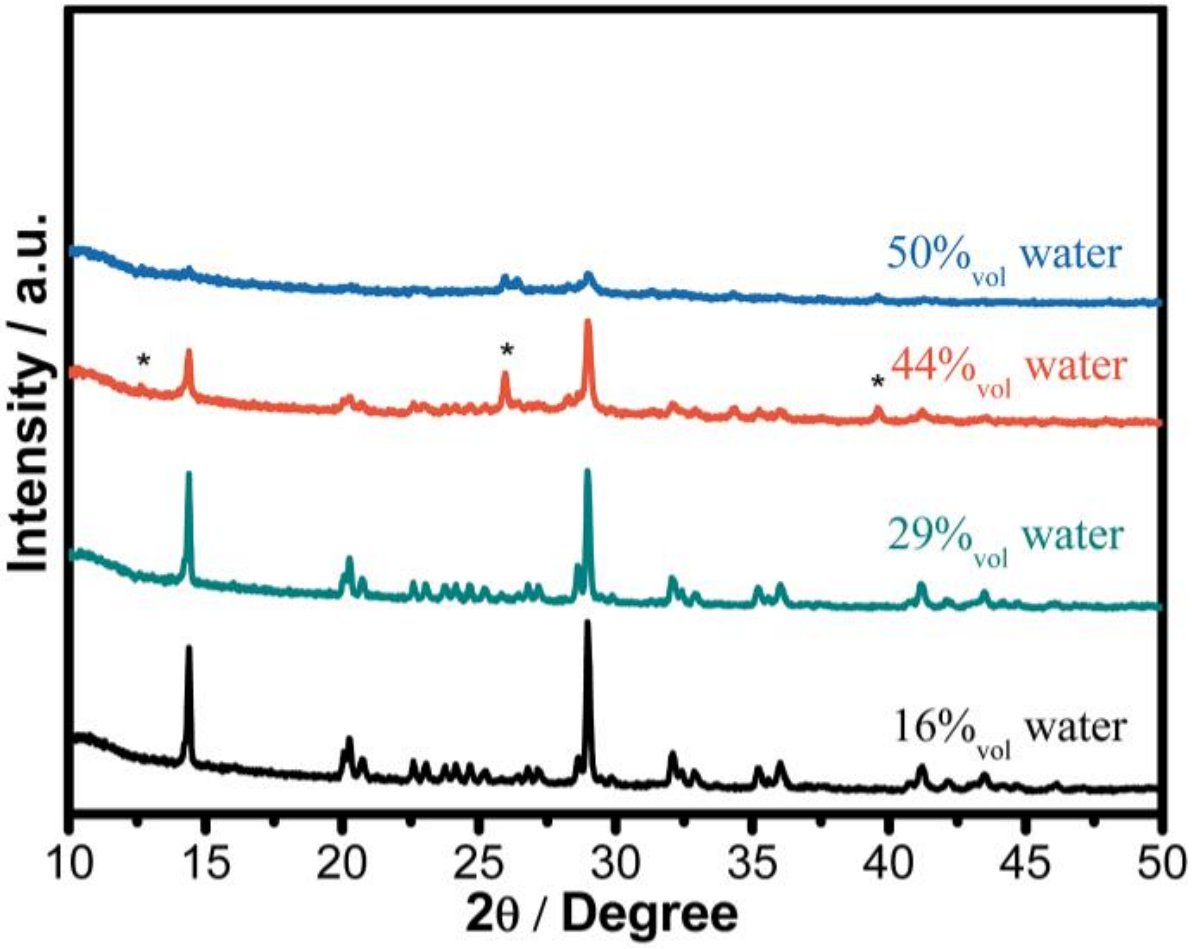

Fig. 4.17 PXRD patterns of $CsPbI_3$@PbI(OH) soaked in ethanol solution with different amounts of water, showing stability in up to 29% water. Peaks from PbI_2 are marked with *.

We have further studied the tolerance of $CsPbI_3$@PbI(OH) to the amount of water in solution and remarkably find that the perovskite is stable with water concentration as high as 29%. In these experiments, 400 ul, 800 ul, 1.6 ml, 2 ml water were added to

γ-$CsPbI_3$ in 2 ml mother liquor (containing PVP, cesium acetate). The volume concentration of water in the above solutions are calculated to be 16%, 29%, 44%, 50%. Fig 4.17 shows the PXRD of samples after soaking in the above solutions for 12h at room temperature. Remarkably, the perovskite is stable under these conditions to water concentration up to 29%. At higher water concentration, peaks belonging to PbI_2 begin to appear, indicating the decomposition of the PbI(OH) shell in such high water concentrations, with *γ*-$CsPbI_3$ completely decomposed in the 50% water solution. This high tolerance of $CsPbI_3$@PbI(OH) to water explains why our synthesis can be readily conducted in its presence.

4.4.4 $CsPbI_2Br$

We then considered whether the method could be successfully applied to the synthesis of other all-inorganic perovskite, such as $CsPbI_2Br$. $CsPbI_2Br$ has attracted considerable interest worldwide, because it has been reported to show improved stability by partial substitution of I^- with the smaller Br^- anion. Prior studies have shown the synthesis of photoactive *α*-$CsPbI_2Br$ through heating followed by quenching to room temperature to kinetically stabilise this phase. Nevertheless, the low-temperature *β*/*γ*-$CsPbI_2Br$ polymorphs are also expected to show similar properties to α-$CsPbI_2Br$, but their synthesis has proved elusive.[127] Our method has the merit of preparation at room-temperature, and so omits the need to prepare the high-temperature phase. Thus, through our room temperature solution method, we are able to prepare the low temperature γ-$CsPbI_2Br$ perovskite polymorph for the first time.

Fig 4.18 shows photographs comparing $CsPbI_3$@PbI(OH) and $CsPbI_2Br$@PbI(OH) colloidal solutions. The reddish colour of $CsPbI_2Br$@PbI(OH) confirms the introduction of Br^- into the lattice. XRD data as shown in fig 4.19 were collected and structure refinement confirmed this phase to be *γ*-$CsPbI_2Br$ with lattice parameters *a* = 8.598(1) Å, *b* = 12.224(2) Å, and *c* = 8.496(1) Å.

Fig 4.18 Photographs of $CsPbI_3$@PbI(OH) and $CsPbI_2Br$@PbI(OH) prepared in solution.

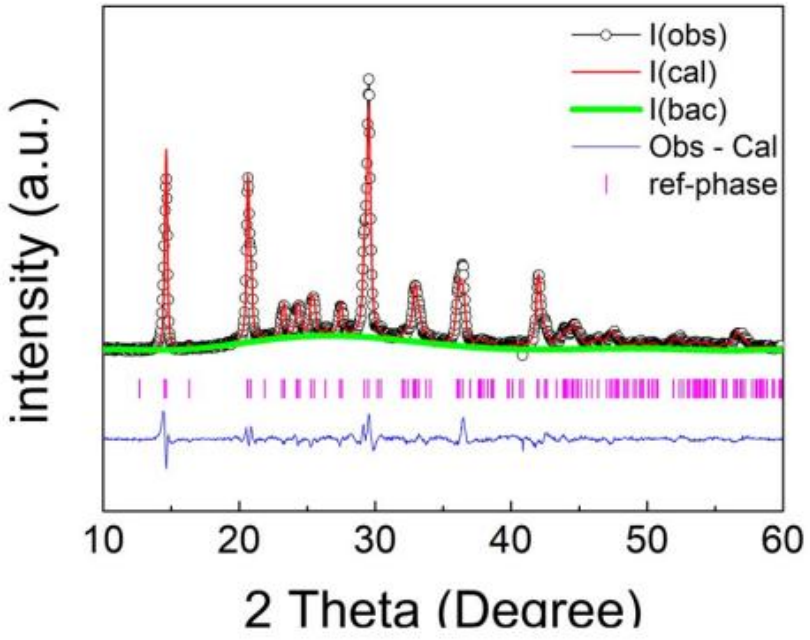

Fig 4.19 Observed, calculated and difference profiles for $CsPbI_2Br$@PbI(OH) from Rietveld refinement of the structure using powder XRD data.

For the refinement $CsPbI_2Br$, we used γ-$CsPbI_3$ strunture file for a starting model. There are two kind of I, which are I1 and I2, in starting model so that we tried the susbtitution with Br at different position. Interestingly these structural studies showed the presence of some I/Br ordering, with the Br located on the I2 site as shown in Table 4.2.

Table 4.2 Refined structural parameters for $CsPbI_2Br$@PbI(OH).

Atom	*x*	*y*	*z*	Mult.	Occupancy	$u_{iso}\times100$ (Å^2)
Pb1	0	0	0	4	1	1
Cs1	0. 4556(11)	0.25	0.0088(17)	4	1	1
I1	0.5085(15)	0.25	0.5575(14)	4	1	1
I2	0.1988(12)	0.0247(11)	0.3012(12)	8	0.52(2)	1
Br2	0.1988(12)	0.0247(11)	0.3012(12)	8	0.48(2)	1

a = 8.598(1)Å, *b* = 12.224(2)Å, *c* = 8.496(1)Å, V = 892.25(15)Å^3

GOF = 2.53, wR = 8.11%

Furthermore, TEM images confirm a similar core-shell structure for $CsPbI_2Br$@PbI(OH) as shown in fig 4.20. The protective shell contribute to the stability of $CsPbI_2Br$ in air. As observed for $CsPbI_3$, $CsPbI_2Br$ degraded into the yellow non-perovskite phase rapidly in samples when there was no PbI(OH) protective layer.

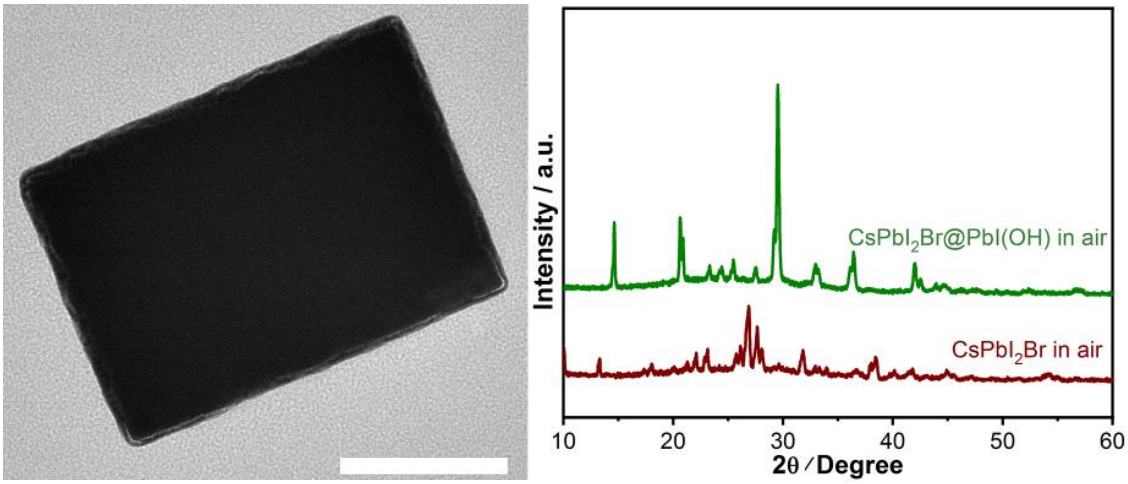

Fig 4.20 TEM image of CsPbI2Br@PbI(OH). Scale bar: 150 nm. b) PXRD patterns of $CsPbI_2Br$@PbI(OH) and g-$CsPbI_2Br$ in air, showing degradation for the latter, which does not have a PbI(OH) protective shell.

4.5 Conclusion

In summary, we have shown a facile solution approach to prepare *γ*-$CsPbI_3$ micro-crystals in an ambient environment for the first time. The rapid precipitation process of *γ*-$CsPbI_3$ ensures the production of the desired perovskite phase at room-temperature, which is then stabilized by the spontaneous degradation of the perovskite toward water, which leads to the epitaxial growth of ultra-thin and single-crystalline PbI(OH) shell on the perovskite surface. The acetate anion is believed to play a key role controlling the degradation of perovskite to ensure formation of PbI(OH), while PVP contributes to capping the process and ensuring the PbIOH shell compactness and uniformity. These coated *γ*-$CsPbI_3$ microcrystals exhibit vastly improved stability both towards moisture and heating in air, which is attributed to the lattice anchoring and uniform physical coverage of PbI(OH) shell. Our method has also been successfully extended to other inorganic perovskite with the synthesis of $CsPbI_2Br$. Benefiting from our room-temperature synthesis, $CsPbI_2Br$ forms the low-temperature *γ* perovskite phase, which represents the first experimental report of *γ*-$CsPbI_2Br$. Uniquely, our study provides a new avenue to the synthesis of stable solar perovskite materials, making use of degradation processes to form a protective stabilization layer on the perovskite. It shows that the bane of many a solar perovskite synthesis (water), can also be a boon, providing that, as in the case here, the degradation products can be tailored to induce surface stability.

5. A general approach to boost low-toxicity alkane as efficient anti-solvents for perovskite solar cells

5.1 Introduction

Anti-solvent assisted crystallization (ASAC) is one the most commonly used methods for the deposition of high-quality perovskite solar cells, where anti-solvents modulate the nucleation process of perovskite films by removing the host solvents, such as *N,N*-Dimethylformamide (DMF), Dimethyl sulfoxide (DMSO), γ-butyrrolactone (GBL).[128-130] It has been widely accepted that the criteria for the choice of high-efficient anti-solvents are: a) The anti-solvent should have good miscibility with host solvents. In other words, a good anti-solvent could interact with and wash out excess host polar solvents to accelerate the formation of seeds in raw films. b) The anti-solvent should not dissolve the reactant or break the perovskite down.[131] It is found that the polarities of common anti-solvents used in previous reports are mainly distributed between 2 and 5 as shown in fig 5.1.[132] The commonly used anti-solvents chlorobenzene (CB) and toluene (Tol) have the lowest polarities and solubility to perovskite among the reported efficient anti-solvents. However CB and Tol are toxic and introduce significant health concerns during the manufacture, as well as resultant hazards to the environment.[133] For example, CB is extremely toxic, which would damage the central nervous system, liver and kidneys of human seriously, as well as polluting the water, soil and atmosphere.[131] More importantly, the dose of anti-solvents used for the fabrication of perovskite solar cells are estimated to be 50-1000 ul/cm^2, which is more than the amount of hazardous host solvent.[134] The huge consumption of toxic solvents would therefore be potentially harmful to workers

and produce a large amount of dangerous waste at the same time, which limits the suitability for industrial production via this route. Therefore, it is urgent to explore alternative low-toxicity and efficient anti-solvents to replace toxic CB and Tol for the target of sustainability.

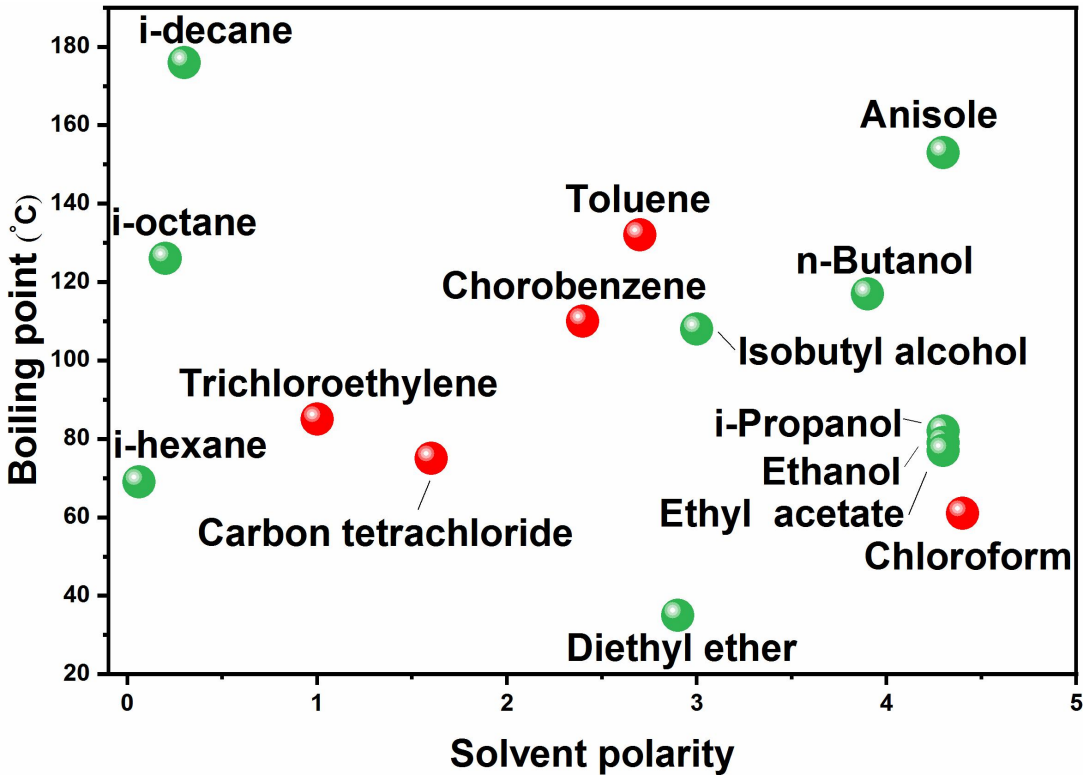

Fig 5.1 Diagram of the boiling point versus polarity of anti-solvents.[131]

Several greener anti-solvents, which are less toxic and more environmentally friendly to humans and the environment have been screened to substitute the usage of toxic anti-solvents. Interestingly, the polarities of low-toxicity anti-solvents reported in recent years, such as i-propanol, isobuthyl alcohol, n-butanol, ethanol, ethyl acetate, anisole and diethyl ether, are slightly larger than those of CB and Tol.[132] The emerging low-toxicity anti-solvents are systemically classed into alcohol-based, ester-based,

ether-based and hydrocarbon-based anti-solvents.[133] These low-toxicity solvents have polarity between 2.7 and 4.5, compared to those of CB and Tol between 2.0 and 2.7. On the one hand, the higher polarity of low-toxicity anti-solvents is good for the growth of perovskite films because these anti-solvents have good miscibility with DMF and DMSO, which can thus remove the host solvents efficiently and boost the nucleation process in the film. Unfortunately, on the other hand, the relatively high polarity brings in various issues at the same time. It is found that perovskite solar cells made with pure alcohol-based low-toxicity anti-solvents, such as i-propanol and ethanol, show very poor performance.[131, 132] High polarity results in the high solubility of organic cations. Therefore, excess FA^+ or MA^+ salt is usually added into the precursor or the anti-solvent to compensate for cations lost. Another issue is that excessive nucleation behavior and narrow dripping windows have been widely observed in ester-based and ether-based greener anti-solvents. For example, when ethyl acetate and diethyl ether are used as anti-solvents, the obtained perovskite films display small grain size, because excessive nucleation occurs during spin-coating resulting from high miscibility between high polar anti-solvents and hosts solvents. Therefore, many efforts have been tried to reduce the polarity of these low-toxicity anti-solvents, i.e. by partially doping with non-polar alkane.

Hydrocarbon-based solvents are considered to be less hazardous than their chlorinated counterparts such as chlorobenzene, dichlorobenzene and chloroform. It has been screened out as candidates for greener anti-solvents, together with ether, ester and alcohol based solvents as reported in the literature.[131] Alkanes, such as hexane (HEX), octane (OCT), and decane (DEC) are studied as a class of less hazardous Hydrocarbon-based anti-solvents in this work. But attentions need to be

put that, alkanes can still cause skin irratation and may cause drowsiness or dizziness and would be dangerous if swallowed. They are perhaps one of the best choices to overcome issues brought by the high polarity of low-toxicity anti-solvents because of their non-polar property.[135] Alkanes have already been very popular with alcohol-based, ester-based and ether-based polar low-toxicity anti-solvents as a kind of additive to achieve moderate polarity for low-toxicity anti-solvents previously. For example, Yang *et al.* reduced the dissolving of MAI by the introduction of non-polar cyclohexane into IPA, which resulted in a dense and smooth perovskite layer.[136] Yu *et al.* and Kang *et al.* reported the enlargement of grain size in perovskite films made by diethyl ether or ethyl acetate, respectively, by the introduction of non-polar HEX to prevent excessive seeds formed during spin-coating.[136, 137]

Despite alkanes showing intriguing properties in terms of reducing the dissolution of the perovskite, modulating the seeding process and slowing down the growth of perovskite, they exhibit limited performance as anti-solvents for high quality perovskite film when they are used on their own, because of a deficit of seeds produced in the films resulting from poor miscibility with DMF/DMSO. Lin *et al* achieved an efficiency of 11.7% with HEX as anti-solvent, which is far behind the development of perovskite solar cells. The deficit seeds in alkane processed perovskite films is a result of their weak miscibility with host solvents.[138] Therefore, the ideal protocol to modify alkanes as efficient anti-solvents is to increase the alkane-dmso interaction or provide artificial seeds for nucleation.

5.2 Design and results

Herein, we established several alkanes as high-efficiency low-toxicity anti-solvents for perovskite solar cells (PSC) by the decoration of perovskite nanocrystals (NCs). Alkanes have been shown to be a kind of poor anti-solvents in previous report, which result into insufficient seeds and poor morphology of perovskite films. With the cooperation of $CsPbI_3$ NCs, high-crystalline, continuous, smooth and oriented films were obtained. The function of NCs in the growth of perovskite films has been carefully characterized and discussed, and we find a perfect hetero-structure between artificial NCs and the perovskite matrix films. The high quality of perovskite films were further confirmed in NiO_x based inverted perovskite solar cells (PSC) fabricated by alkane/NCs anti-solvents, which show excellent performance, even better than devices fabricated with commonly used toxic CB.

5.3 Synthesis and preparation

5.3.1 $CsPbI_3$ NCs synthesis

The preparation of Cs-oleate was realized by mixing 0.1 g Cs_2CO_3, 1 ml oleic acid and in 3-neck flask. The mixture was stirred under vacuum at 120 ^oC and bubbled under N_2 at 150 ^oC. The Cs-oleate was stored under N_2 for use after it was totally dissolved. Then, 1 ml oleylamine,1 ml oleic acid and 10 ml octadece was mixed and degassed at 100 ^oC, after which 0.256 g PbI_2 was added and stirred under vacuum at 120 ^oC until fully dissolved. Then the temperature was raised to 170 ^oC and 1ml Cs-oleate precursor was swiftly injected into the mixture. The reaction was stoped by quenching in a ice-water bath in 5-10 s later. For the washing of NCs product, 10 ml MeOAc was added into the reaction mixture, and then the mixture was centrifuged at 10000 rpm

for 5 min. The supernatant was discarded and precipitate was dispersed in hexane, then the hexane solution was centrifuged at 8000 rpm for 3min to remove insoluble agglomerate. The supernatant was stored under dark until use.

5.3.2 NiO_x NCs synthesis

NiO_x NCs were synthesized according to the procedures reported elsewhere with some modification. Briefly, 0.1 mol $Ni(NO_3)_2 \cdot 6H_2O$ was dispersed in 20 mL of deionized water firstly. Then NaOH solution (10 M) was slowly added into the $Ni(NO_3)_2 \cdot 6H_2O$ solution with strong stirring until the pH of solution was close to 13. After being stirred for another 15 min, the colloidal precipitation was washed with deionized water three times, and dried at 80 °C overnight. The obtained green powder was then calcined at 270 °C for 2 h to obtain a dark-black powder. The NiO_x NCs inks were prepared by dispersing the obtained NiO_x NCs in deionized water/isopropanol (3/1) to obtain a concentration of 10mg/ml.

5.3.3 Device fabrication

ITO substrates were cleaned with water, acetone and isopropanol for 3 times, and then dried under N_2. The substrates were treated with UV for 15 min and then NiO_x NCs was deposited by spin coating (3000 r.p.m) and annealing at 100^{o}C for 10 minutes in air. 22.4 mg MAI, 18.2 mg CsI, 172 mg FAI, 73.4 mg $PbBr_2$ and 507 mg PbI_2 were dissolved in 1ml DMF/DMSO (4:1) and stirred at 60^{o}C for 1h. Perovskite precursor was coated onto the ITO/NiO_x substrates at a speed of 4,000 r.p.m for 35 s. During the last 20 s of the spinning process, the substrate was treated by gently with anti-solvents. The substrate was then annealed on a hot plate at 100 ^{o}C for 50 min. PEAI was spin-coated perovskite at the speed of 4000 r.p.m, following by spin-coating

a layer of PC61BM (2 wt%, 1100 r.p.m). Then, BCP were gently spin-coated (0.5 mg/ml in IPA, 4000 r.p.m, 30s) on top. Finally, 100-nm-thick Ag was deposited.

5.4 Discussion

5.4.1 Structure

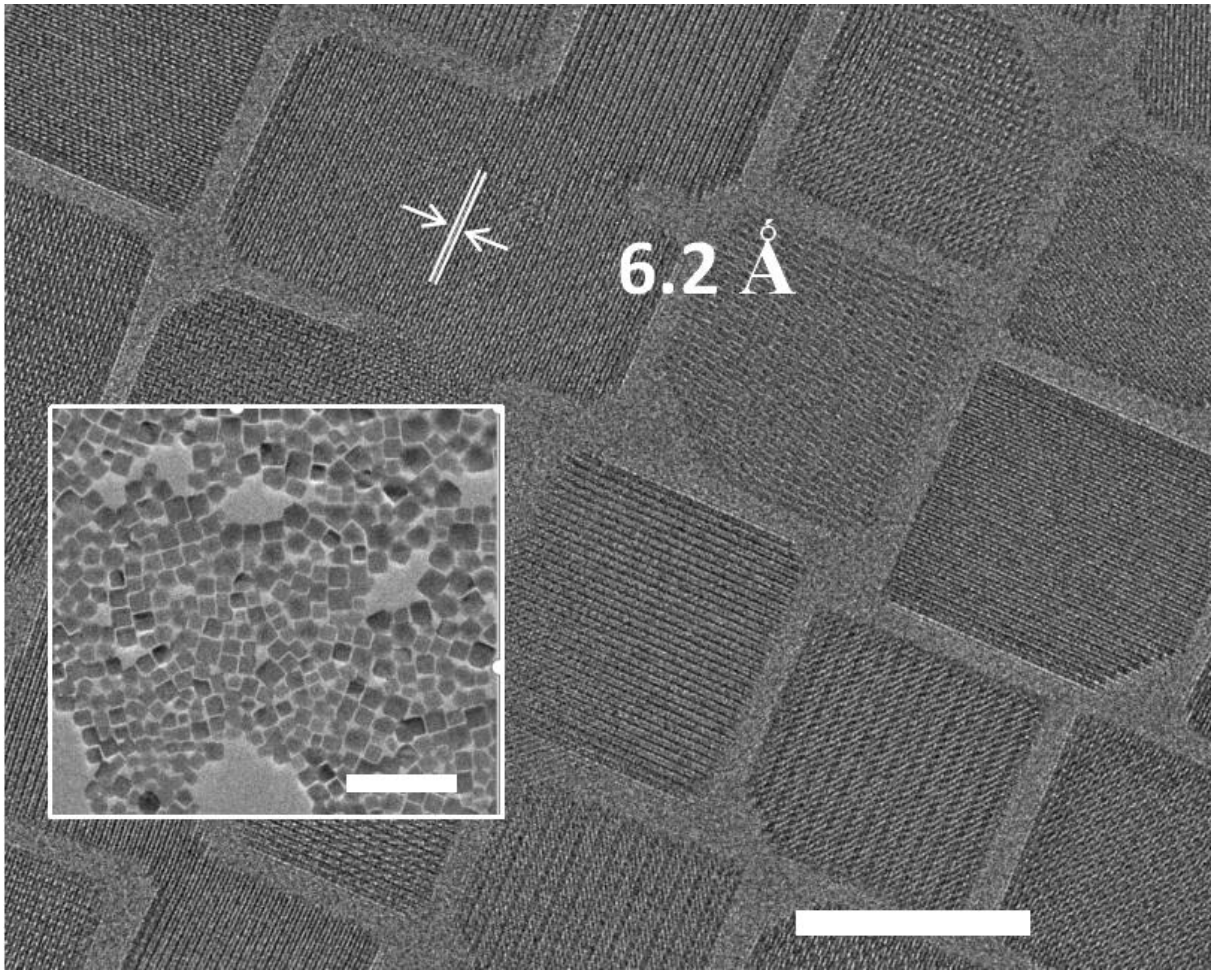

Fig 5.2 High-resolution Transmission Electron Microscope images of $CsPbI_3$ NCs. Scale Bar 20 nm. Inset: Low magnification image. Scale bar: 100 nm.

The $CsPbI_3$ NCs were characterized by PL, TEM and PXRD. Low magnification and high-resolution Transmission Electron Microscope (TEM) characterization of NCs in fig 5.2 shows that the NCs have a uniform morphology of cubes with average size of

20nm. High-resolution TEM (Hr-TEM) results shows that the $CsPbI_3$ NCs have the cubic phase with the lattice distance of 6.2 Å as reported in the literature.[139] The highly-crystalline nature of the NCs are confirmed by the sharp emitting peak at 646 nm when illuminated by laser with wavelength of 405 nm as shown in fig 5.3.[139]

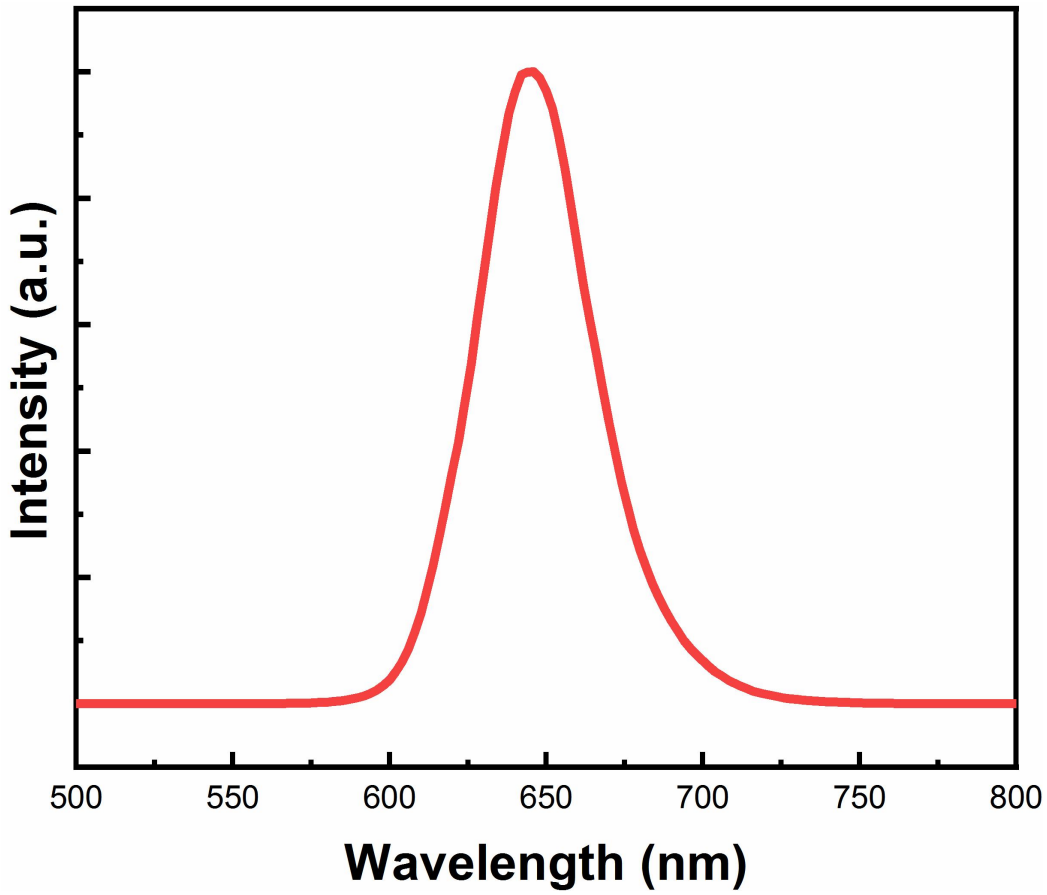

Fig 5.3 Photo-luminescence spectra of $CsPbI_3$ excited by laser with wavelength of 405 nm.

Ternary cations perovskite (Cs,FA,MA, (Cesium, $HC(NH)_2^+$, and $CH_3NH_3^+$)), which are commonly processed with toxic CB as anti-solvent for high-quality films in the past years, has been chosen as the matrix perovskite here to study the function of NCs loaded during spin-coating.[140] Moreover, this kind of matrix perovskite has similar

lattice parameters with $CsPbI_3$ as illustrated by X-ray diffraction (XRD) characterization of matrix perovskite processed by CB and $CsPbI_3$ NCs in fig 5.4. $CsPbI_3$ NCs exhibit an orientation along with (001) facet, which is coincident with the uniformly cubic morphology from TEM. The broad shape of peaks proves the nano-size nature of the NCs. The PXRD pattern of CB processed matrix perovskite shows that the films adopt a cubic phase without preferred orientation. The design of components in the cubic phase matrix perovskite follows the Goldschmidt tolerance factor rule, by careful choice of the size of cations and halide anions.[45] The similarity of the lattice parameters between $CsPbI_3$ and mixed cation perovskite results from the synergic balance between the large FA^+ and small Br^-.

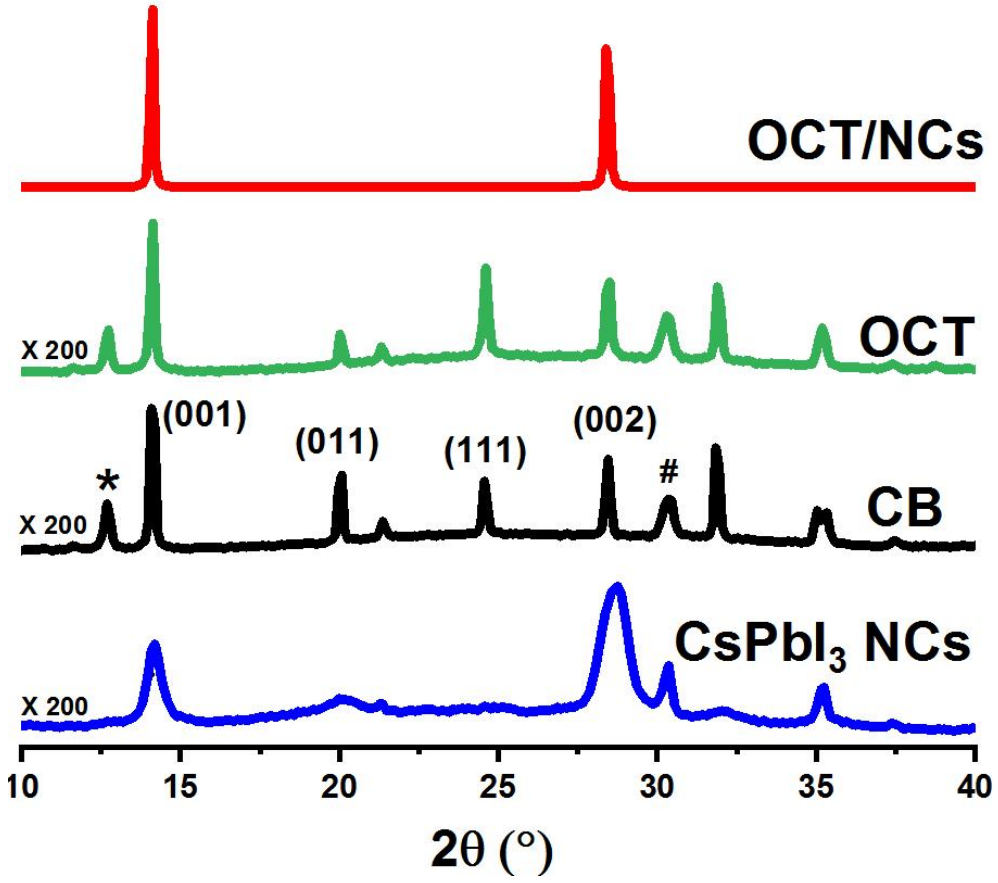

Fig 5.4 X-ray diffraction patterns of $CsPbI_3$ NCs, perovskite films processed with CB, OCT and OCT with $CsPbI_3$ NCs. Diffraction from PbI_2 and ITO was marked by * and #,

respectively. The result shows excellent crystallinity with preferred orientation in the presence of NCs.

Despite the poor morphology of perovskite films processed by pure OCT, they exhibit similar PXRD pattern with CB processed films, which might result from the assistance of annealing process. However, when $CsPbI_3$ NCs are added into OCT, excellent crystallinity with high-orientation along with (001) facets in the matrix perovskite film is observed. A similar phenomenon has also been observed perovskite film dripped by HEX and DEC as anti-solvents as shown in fig 5.5. These interesting findings drove us to explore the interaction between alkane/NCs and matrix perovskite to understand the improvements observed.

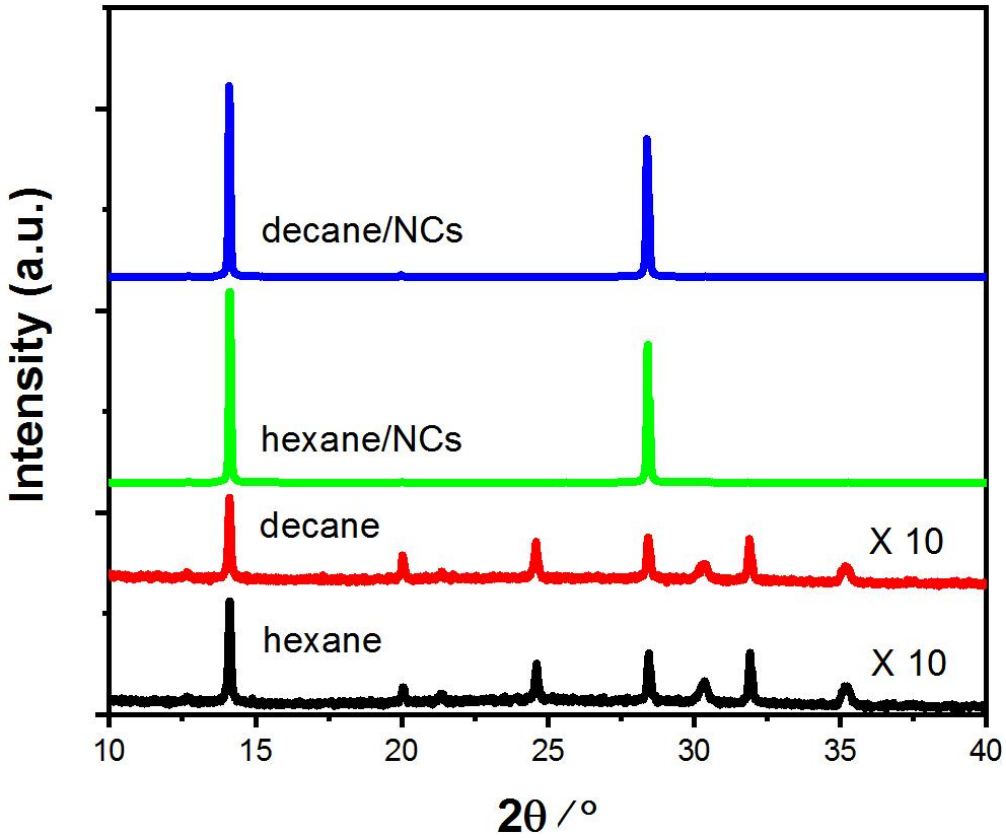

Fig 5.5 The PXRD patterns of films fabricated with hexane and decane w/ and w/o NCs as anti-solvents. The result shows excellent crystallinity with preferred orientation in the presence of NCs.

5.4.2 Growth of films

To find out the role played by NCs, we chose OCT as the representative anti-solvent for detailed study. The surface of NCs was fully covered by oleyammine and oleic acid for stabilization. Desiccation of ligand would happen to perovskite NCs in contact with polar solvents, while the individual perovskite NCs tends to self-assemble into bigger crystals at the same time after the loss of surfactant.[141] Previous works have also proven that contribution the addition of a long-chain surfactant in the precursor has profound influence to the growth of perovskite film. Therefore, it is meaningful to study the unique role played by oleyammine.

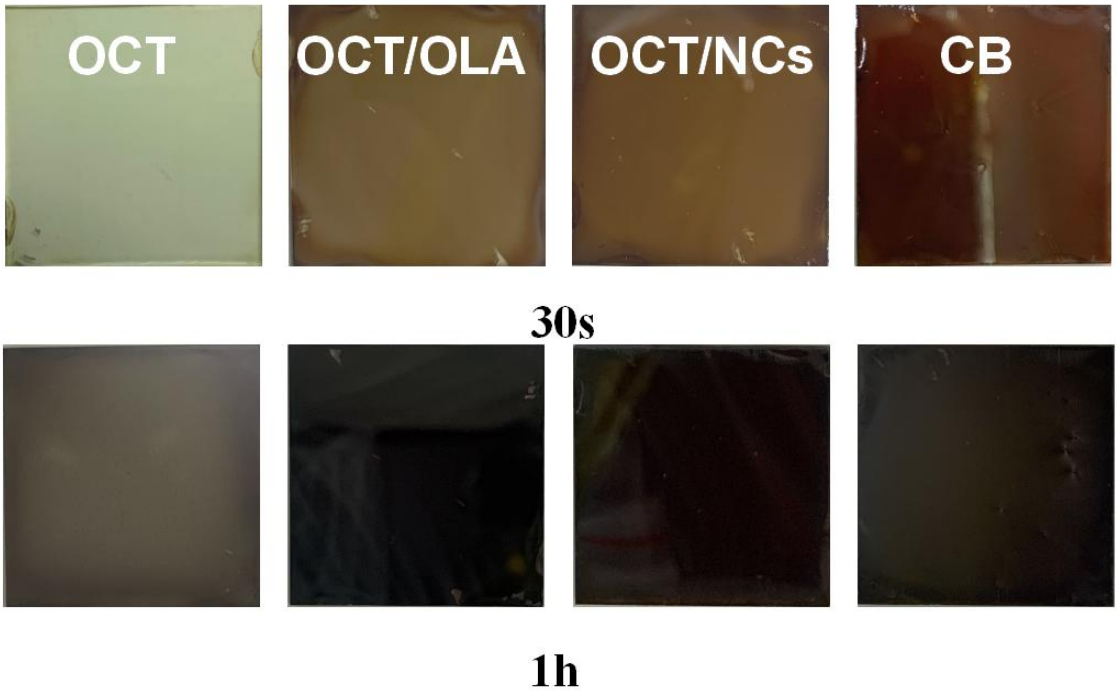

Fig 5.6 Optical photographs of raw films standing in N_2 glove box after dripping with OCT, OCT/OLA, OCT/NCs and CB.

We studied in detail wet films fabricated by CB， OCT， OCT/OLA (0.1%Vol) and OCT/NCs (1mg/ml) as anti-solvents, respectively. The results showed that films

dripped with OCT have a light-yellow color 30 s after spin-coating as shown in fig 5.6. The transparent film then turns into a black and yellow film after standing in a N_2 filled glove box for 1h. In contrast, the other films show a light brown color and turn into dark brown color finally.

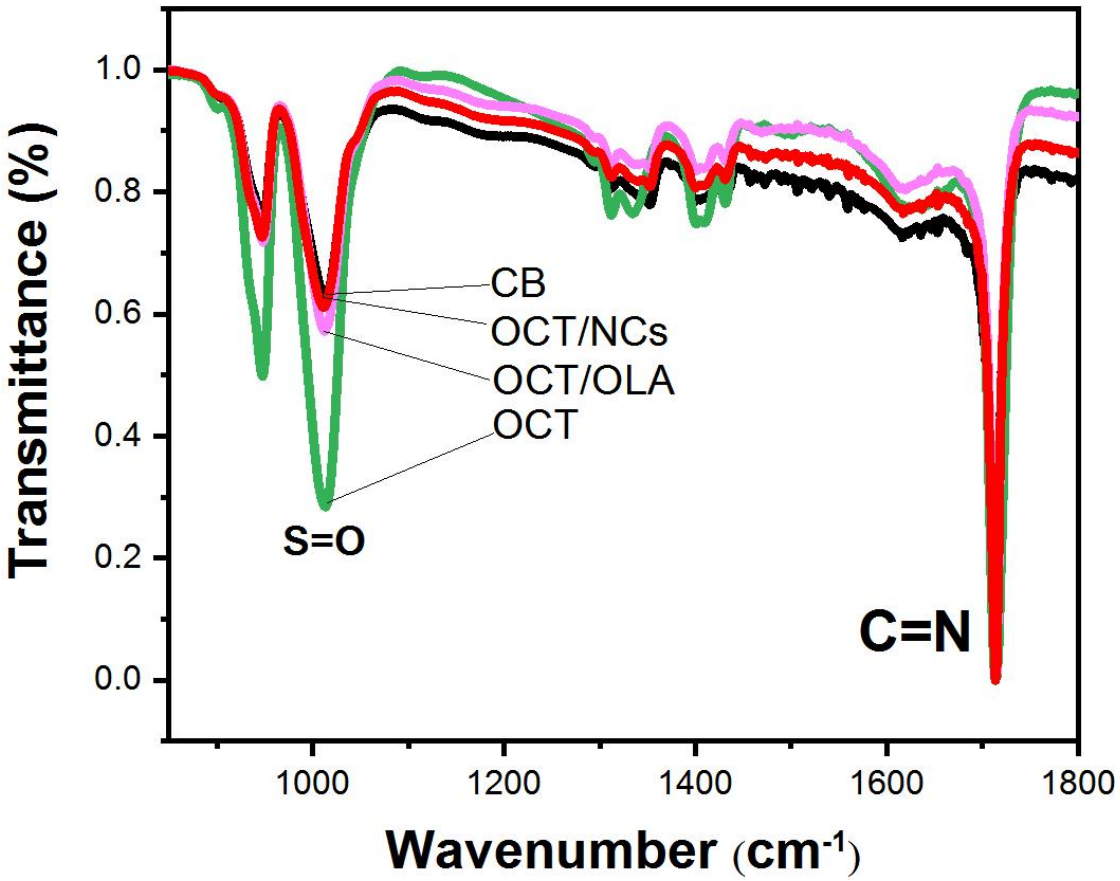

Fig 5.7 Fourier Transform Infrared spectrum of wet perovskite films after dripping with different anti-solvents. (Green: OCT, Purple: OCT/OLA, Red: OCT/OLA, Black: CB)

Fourier Transform Infrared (FTIR) characterizations were used to compare the residual amount of DMSO. Fig 5.7 shows the FTIR spectra of wet perovskite films after dripping with pure OCT, OCT with OLA, OCT with $CsPbI_3$ NCs and CB. The peak at 1717 cm^{-1} is assigned to be C=N bond from FA^+.[142] The peak at 1020 cm^{-1} is

identified as the S=O bond from DMSO molecules.[142,143] Films prepared with OCT contain the highest amount of DMSO compared to the other samples, proving the poor ability of OCT to wash off DMSO. Some residual amount of DMSO is essential for the growth of high-quality perovskite films, in particular to form the correct amount of FAI-PbI_2-xDMSO intermediate phase seeds. However, excess DMSO is detrimental to the films because of insufficient seeds and the damage of DMSO to the films, which would lead to numerous pin holes and discontinuous films, as well as the formation of non-active yellow phase after spin-coating or after annealing. The introduction of OLA or NCs into OCT reduces the amount of DMSO in wet films, indicating OLA might be responsible for the reduction of residual DMSO. CB is the strongest anti-solvent among those examined with respect to washing out DMSO，as illustrated by the lowest intensity for the S=O vibration peak.

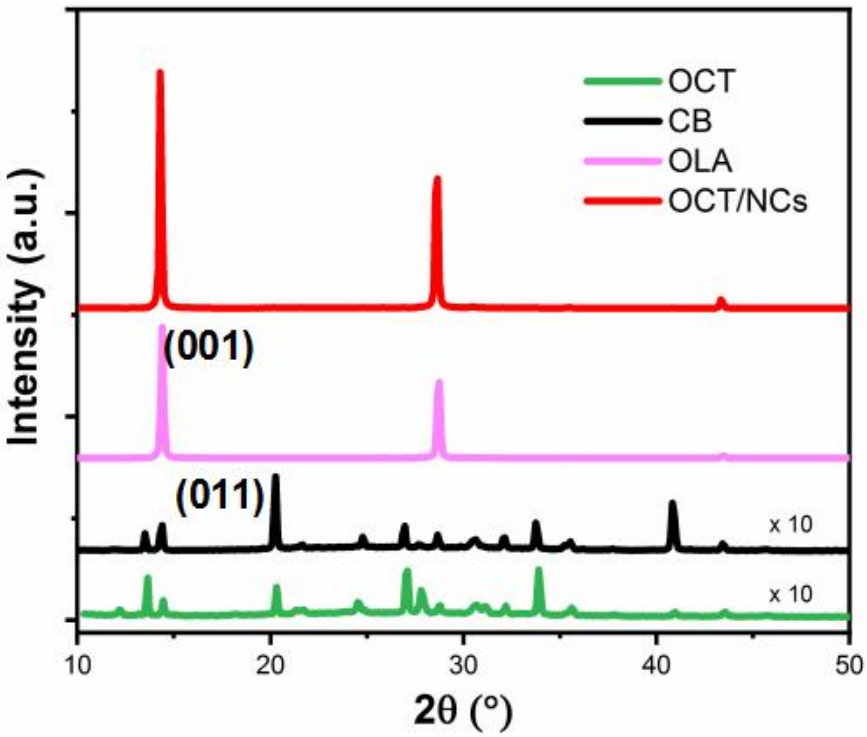

Fig 5.8 X-ray diffraction patterns of raw films without annealing (left).

Fig 5.8 shows the PXRD characterization of films after spin-coating without annealing. The amount of yellow phase formed in the wet film is greatly reduced compared with that of film processed by pure OCT. The signal of yellow phase perovskite is observed in OCT processed perovskite film, while a strong signal of PbI_2 co-existed with perovskite phases both in the OCT and CB processed films indicating that transformation into cubic phase in room temperature is incomplete. Moreover, the formed cubic phase has a different orientation, which displays the strongest XRD peak at the facet of (011) at 19.9º instead of the facet of (001). In comparison, strong orientation along with (001) facets and high diffraction intensity, are observed for both OCT/OLA and COT/NCs processed samples, which is identical to the orientation of annealed films. Ultraviolet and visible spectrum (UV-Vis), as shown in fig 5.9, gives similar results, where OCT is the worst solvent to wash DMSO out which results in the existence of yellow phase and lowest absorption from UV-Vis.

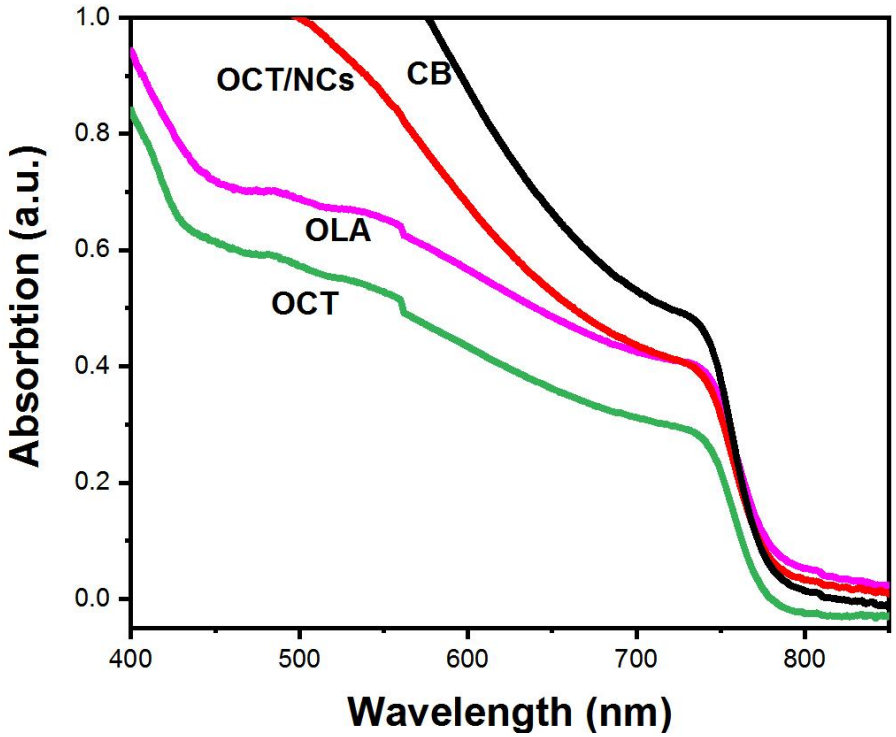

Fig 5.9 Ultraviolet and visible spectrum of raw films without annealing.

To find out how OLA can help OCT to wash off the DMSO, we calculated the molecular electrostatic potential (MEP) in fig 5.10, which has been widely used to study the intra-molecule interaction and interacting sites.[144] The red color indicates an electron-rich area which tends to form hydrogen-bond interaction. The red color indicates an electron-rich area which tends to form hydrogen-bond interactions. It is interesting that the molecular structure of OLA is in the form of a surfactant, where the $–NH_2$ end site has strong negative MEP and the opposite long-chain alkanes shows very low MEP. The $-NH_2$ group at one site is favorable for the interaction with DMSO though hydrogen-bonding, while the long-chain is mutually soluble to alkanes. Therefore, OLA acts as a surfactant in OCT anti-solvent to wash out DMSO from the spin-coated wet film, which promotes the homogeneous nucleation of perovskites and then offers effective bulky nuclei sites.

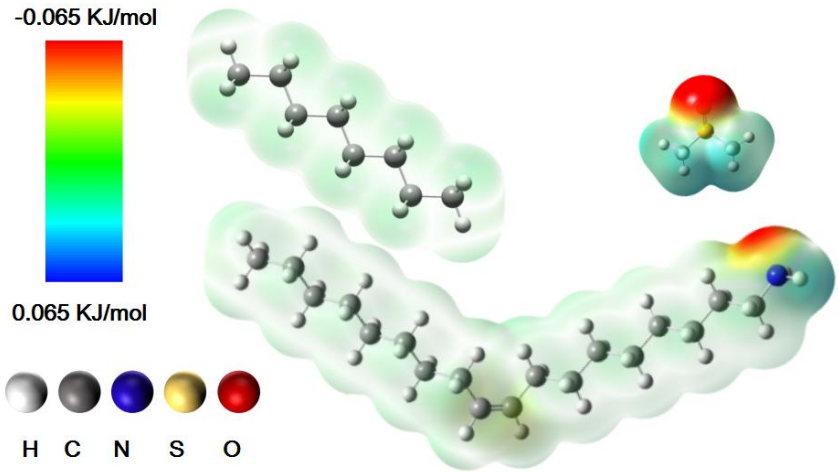

Fig 5.10 The molecular electrostatic potential of OLA and an illustration of interaction between OLA, DMSO and OCT.

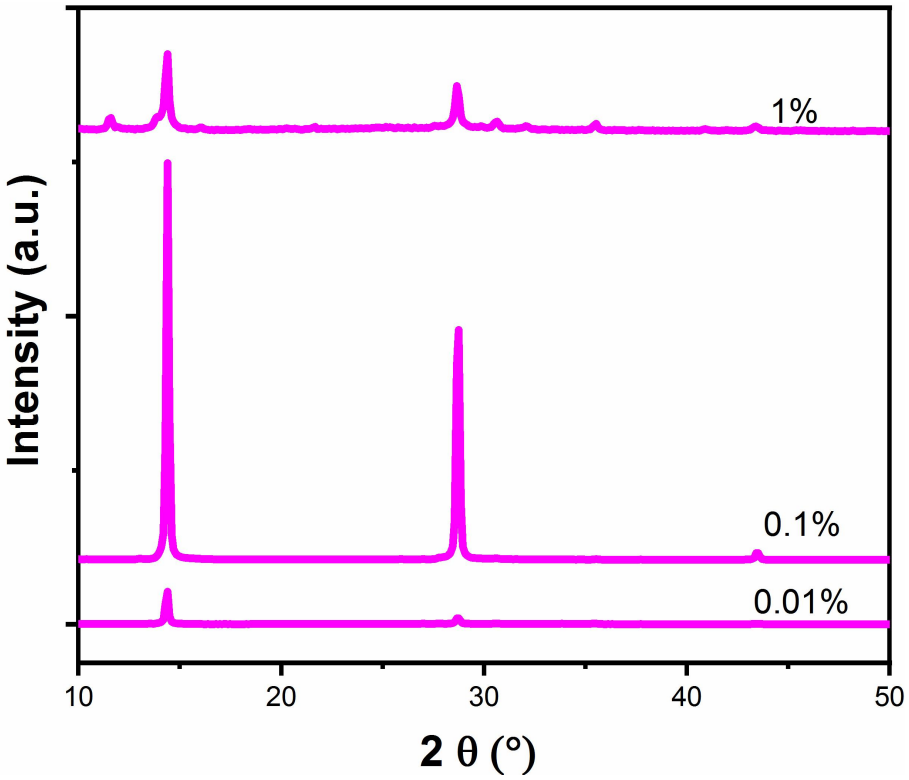

Fig 5.11 PXRD patterns of perovskite dripped by octane with different concentration of OLA.

We studied the amount of OLA needed and found that 0.01%-0.1% (Vol) of OLA in OCT is efficient enough as shown in fig 5.11. Higher concentration of OLA up to 1% would dissolve and destroy the film because OLA is a relatively strong Lewis base.

Next, we studied the changes in morphology of annealed films, formed with different kinds of anti-solvents, during the annealing process. The films prepared with octane, as well as hexane and decane, display discontinuous morphology with lots of holes at the boundary island domain as shown in fig 5.12.

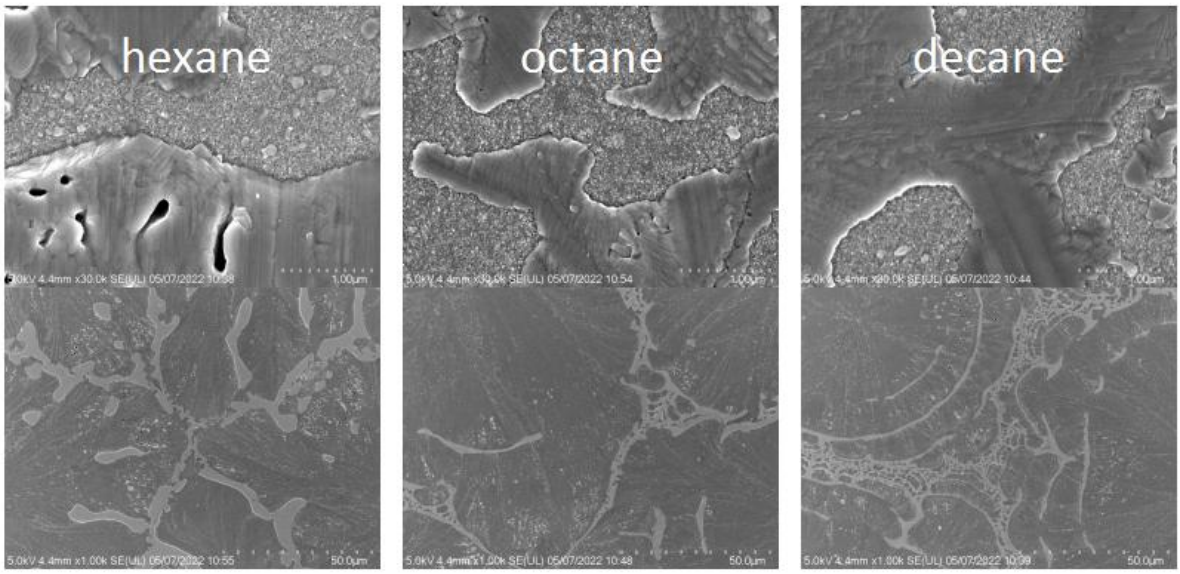

Fig 5.12 SEM images of perovskite films prepared by hexane, octane and decane as anti-solvents, showing the discontinious morphologies. (Dark color area with line texture on surface and high roughness is corresponding to perovskite layer. Light color area with relative smoother surface means the exposure of ITO substrate.)

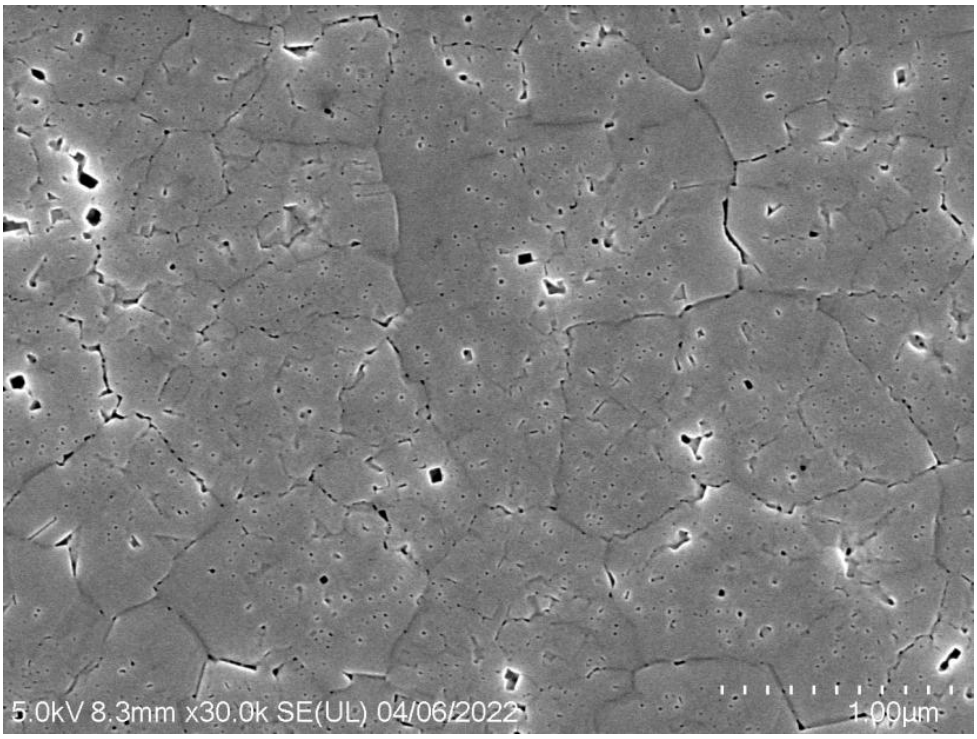

Fig 5.13 SEM image of perovskite film fabricated with octane/oleyammine(0.1%Vol).

The film prepared with OLA shows poor morphology with lots of holes at the boundary island domain as shown in fig 5.13. However, the films prepared with OCT/NCs.show continuous and dense morphology as favored for perovskite solar cells. We compared the perovskite film formation process using OCT/NCs with the process for the most commonly used CB as shown in fig 5.14. The films prepared by OCT/NCs display a larger grain size than that of CB treated. The smaller grain size in film processed with CB results from the excess seeding during spin-coating, which has been proven by the lowest concentration of residual DMSO as shown by FTIR, as well as darkest color and highest absorption proved by UV-vis spectrum of films before annealing in fig 5.7 and 5.9.

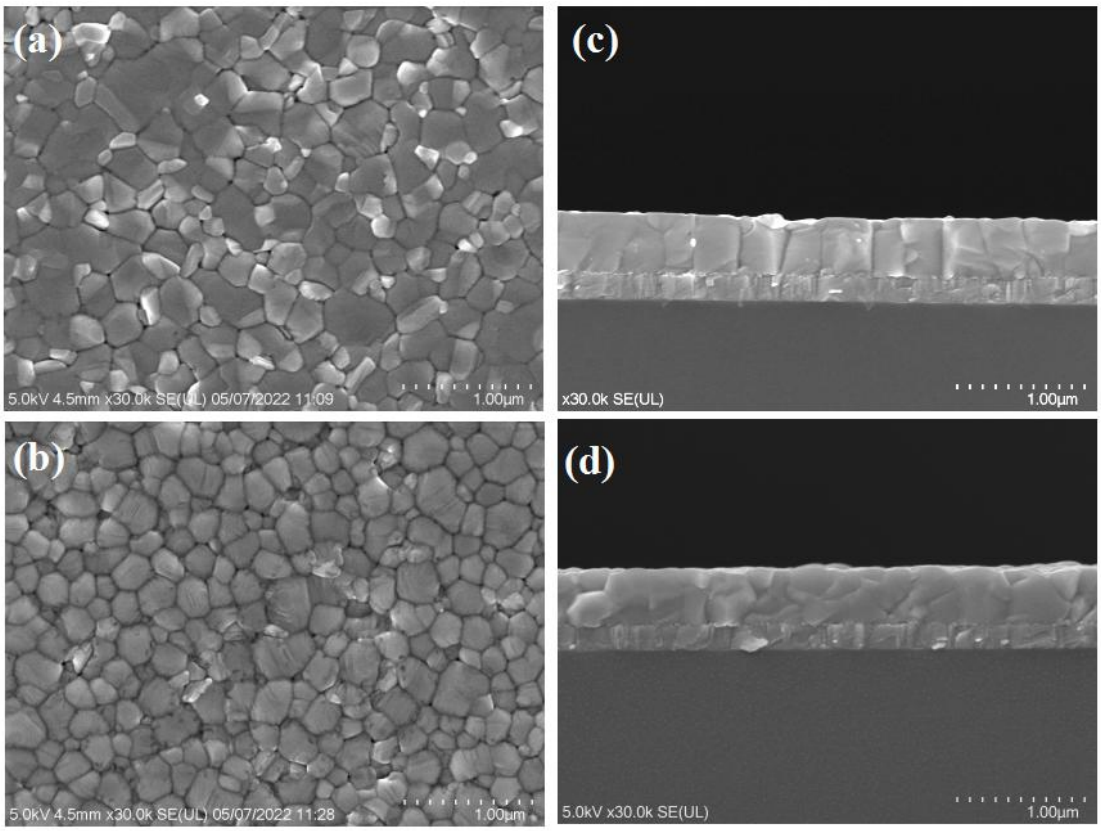

Fig 5.14 Top-view Scanning Electron Microscope images of a) OCT/NCs and b) CB processed perovskite. Cross-section Scanning Electron Microscope images of c) OCT/NCs and d) CB processed perovskite.

The cross-sectional SEM images (fig 5.14) show that grains in the film treated with OCT/NCs grow perpendicular to the substrate, which is favorable for carriers transport in perovskite solar cells as well. The perpendicular growth is further confirmed by the GIWAX result as shown in fig 5.15. GIWAX results reveal that OCT/NCs processed film shows higher crystallinity than that of CB processed film. Moreover, the bolded red zones in images show the perpendicularly oriented growth of OCT/NCs processed film with the function of NCs. In comparation, CB processed film shows poor orientation in q_z direction, which is the direction of carriers transport in devices.

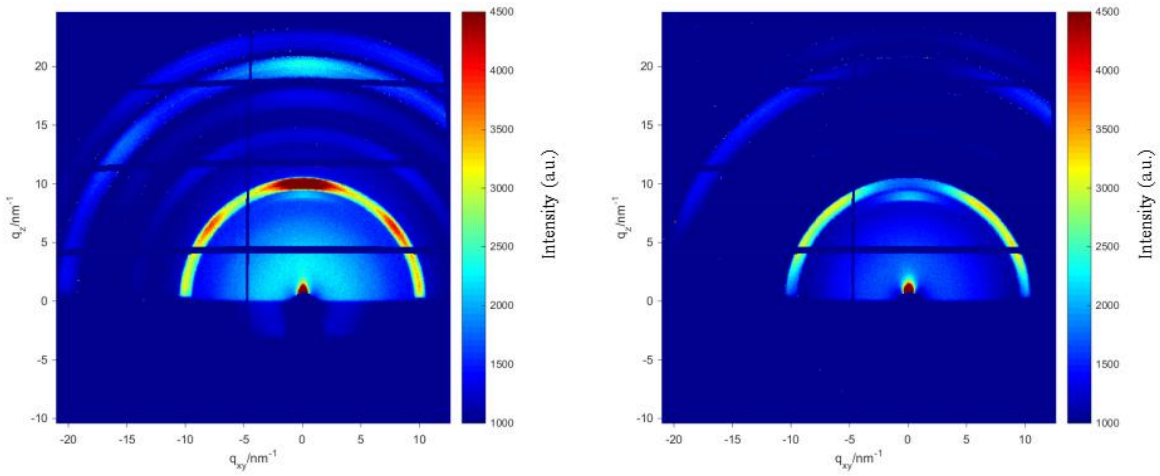

Fig 5.15 GIWAX measurement of a) OCT/NCs and b) CB processed perovskite.

Moreover, the top surfaces of OCT/NCs process films are flat and crystalline. In comparation, CB treated grains show a round top surface. AFM measurements show that the roughness is reduce from 12 nm to 9 nm, when CB was replaced by OCT/NCs as anti-solvents as shown in fig 5.16. The roughness was calculated by AFM software with root mean square (RMS) method using the image data (9 um^2, Number of points:147456). The decreasing roughness is thought to result from the orientated growth of the film with uniformly exposed facets.

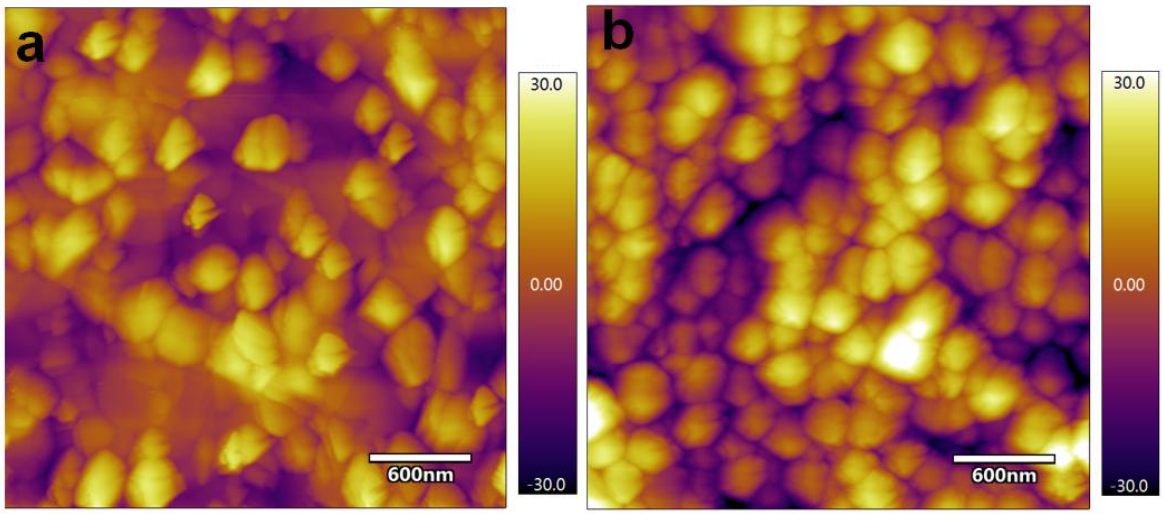

Fig 5.16 Atomic Force Microscope images of a) OCT/NCs and b) CB processed perovskite.

5.4.3 Perovskite hetero-structure

The results indicate that NCs play an important role in supplying seeds in wet films because the films fabricated both by OCT and OCT with OLA shows poor morphology attributed to insufficient seeds. Never the less the mechanism still needs to be explained. Post literature has shown that NCs, such as PbS quantum dots, carbon QDs and ZnS NCs, are good candidates as artificial seeds because of their ability for dispersion in anti-solvent or precursor.[126, 145] For example, Sargents *et al.* reported the addition of PbS NCs along with CB anti-solvent and they found strong lattice anchoring between PbS core and $MAPbI_3$ matrix helps to stabilize the perovskite. Among them, perovskite NCs are thought to be one of the most ideal candidates as artificial seeds for perovskite films because they have the same structure and chemical constituents as the perovskite matrix. The kinetics of NCs as seeds to boost the growth of high-quality films can be explained by the change in Gibbs free energy. There are two periods of growth process. The first step is the nucleation process, for

which a critical free energy G* has to be overcome, the crystal grows spontaneously in the second

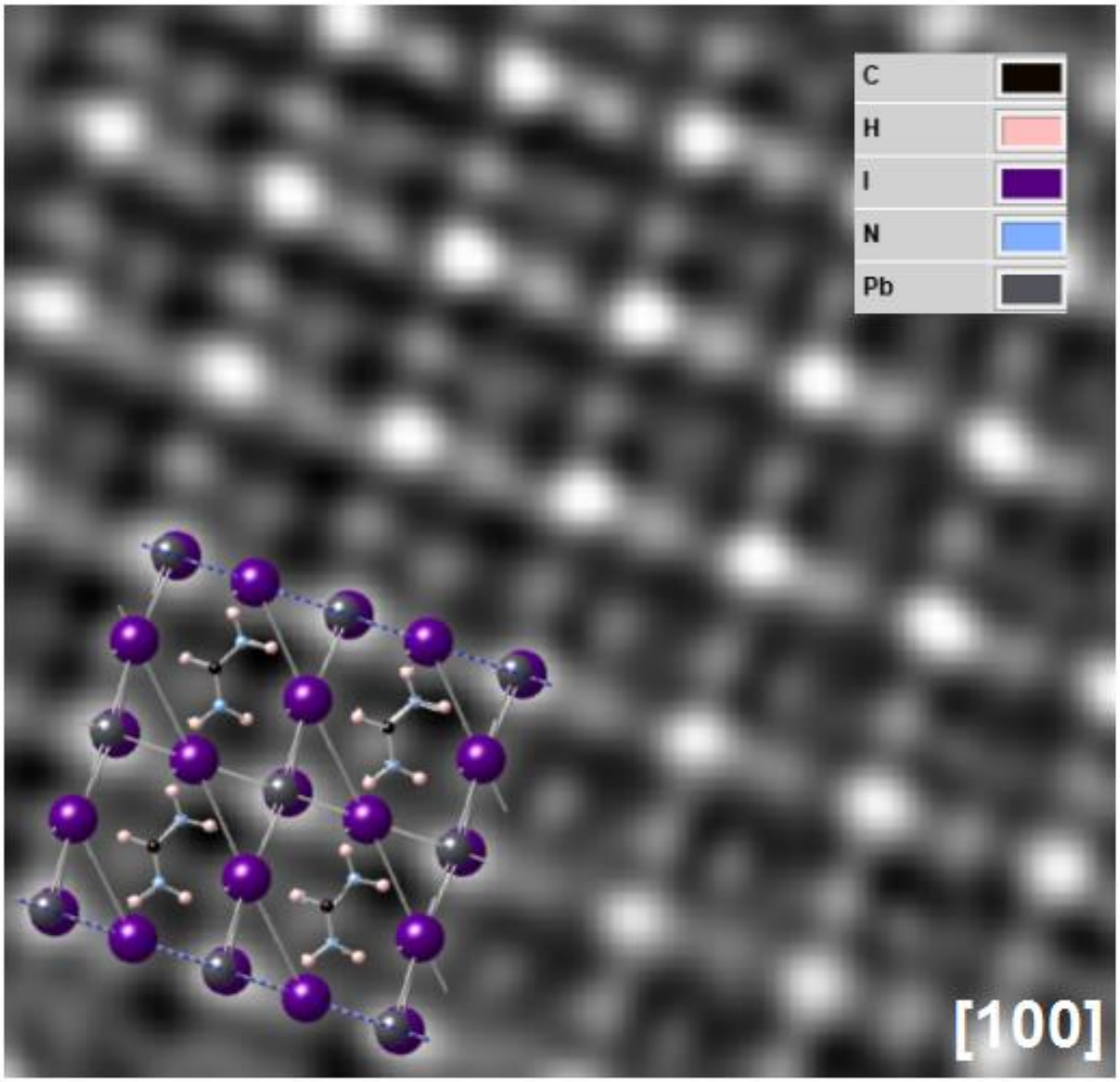

Fig 5.17 Cryo-EM images of matrix perovskite with atom resolution. $FAPbI_3$ is in a cubic phase and have a *Pm*3*m* space group. Similar to $CsPbI_3$, $FAPbI_3$ has a Pb-I octahedra network with FA^+ cations filled in the void.

period.[146] Heterogeneous nucleation is favorable over homogeneous nucleation during the growth of perovskite films, wherein the nucleation barrier is reduced at the liquid–solid interface.[147, 148] The addition of artificial seeds accelerate the crystallization by overcoming the formation of nuclei process. There have been several works reported about the use of perovskite NCs as an additive along with common anti-solvent such as CB. For example, Osmar and Zhu et al. explored the passivation function of NCs to perovskite solar cell, which mainly resulted from the dissociated ligands from NCs.[149] However, the intriguing function of NCs as artificial seeds hasn't been definitely proven until now because of concerns about dissolving of NCs. This is shown now for the first time in this world, where we reveal the structural interaction of artificial perovskite seeds with the matrix perovskite films. To achieve this goal, the samples were studied by Cryo-electron microscopy (Cryo-EM), which has been widely used for electron sensitive materials.[150] It has been well studied that high dose electrons irradiation would damage the perovskite, which will be decomposed into PbI_2 finally.[151] In our test, we adopted a safe dose of less than 30 $e^-/Å^2$. Fig 5.17 shows Cryo-EM images of matrix perovskite with atom-level resolution.

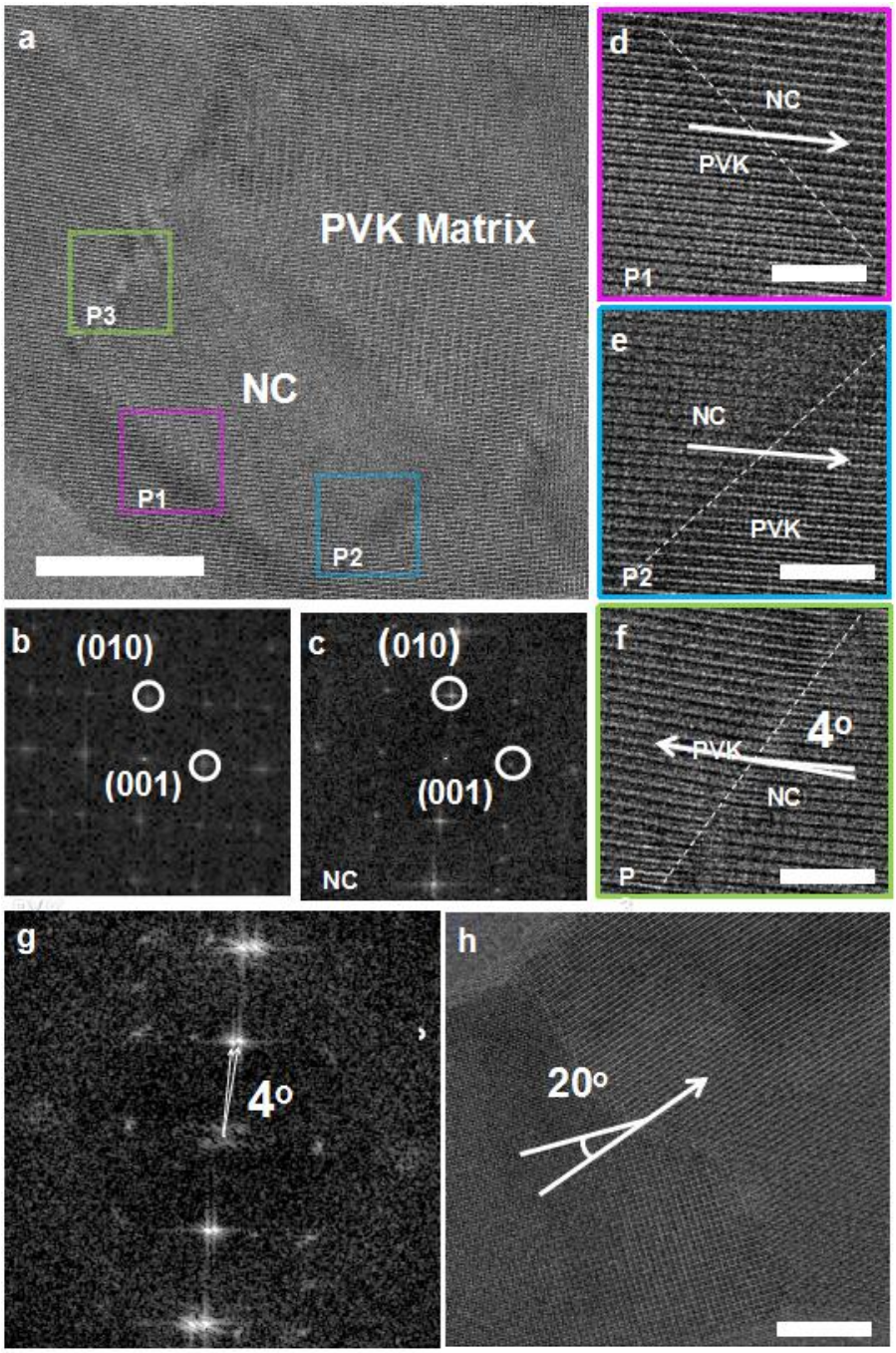

Fig 5.18 a) High-resolution transmission electron microscopy (HrTEM) images of a $CsPbI_3$ NC embed in perovskite matrix. Fast Fourier transform of HRTEM images corresponding to the area of b) matrix perovskite and b) $CsPbI_3$ NCs. d) HrTEM images of grain boundary between matrix perovskite and NC corresponding to the areas of d) P1, e) P2, f) P3. g) Fast Fourier transform of HRTEM images of area P3. h)

High-resolution transmission electron microscopy images of grain boundary without NCs.

Fig 5.18a shows the TEM image of NCs embedded in matrix triple-cation perovskite. The NC is assembled by two NCs because of the dissolution of ligands. The bare surface of NCs with high surface energy is favorable for the growth of matrix perovskite on them. Fast Fourier transform (FFT) images of the matrix perovskite and NC shows that both of them remain as the cubic phase as show in fig 5.18b and c. It can be found that the matrix perovskite is epitaxial grown on NC in areas of P1 and P2, showing perfect lattice anchoring as shown in fig 5.18 d and e. However, there is a slight deviation of crystal orientation of about 4° at the boundary of a NC as shown in fig 5.18f. FFT image of boundary area (fig 5.19g) confirms the deviation of crystal orientation. Fig 5.18h shows the TEM image of a common grain boundary with a large deviation up to 20^{o}. Grain boundaries are detrimental to the performance of perovskite, which would introduce trap states and reduce short-circuit current density. We found that the deviation of the grains' orientation creates strong strain between grains boundaries as shown in fig 5.19. The strain at grain boundary is proven by the changes of lattice stripes in TEM images. The ordered lattice stripes (yellow square) inside crystal is slowly distorted when it comes to grain boundary (red circle) because of the strong interaction of two grains with different crystal orientation. The detrimental stain also leads to serious atom disorder as shown in the green area. Therefore, the boundary of NCs and matrix perovskite is expected to be free of traps triggered by orientation differences because of their excellent epitaxial growth.

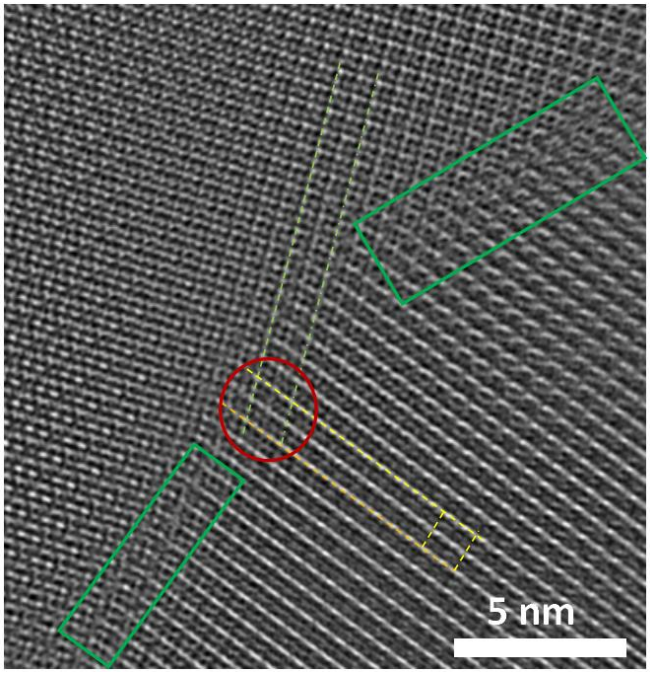

Fig 5.19 Enlarged HRTEM image of grain boundary. Disorder (green) and distortion (red) at grain boundary are observed. The adjacted grains were grown in different orientation (yellow).

5.4.4 Performance of the solar cell

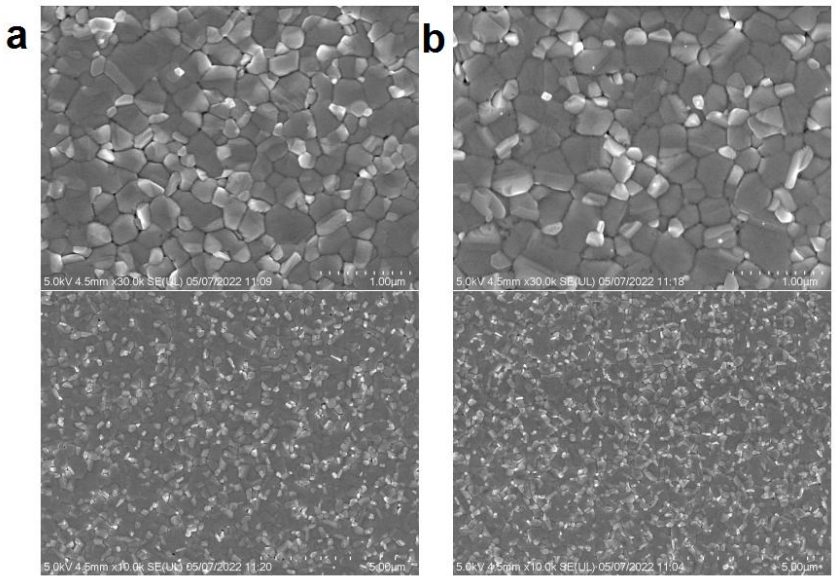

Fig 5.20 SEM images of perovskite films prepared by a) hexane, b) decane as anti-solvents under the magnification of 30k (top) and 1k (bottom).

The films prepared with HEX/NCs and DEC/NCs were also proven to be dense and continuous as shown in fig 5.20. Therefore, we compared the performance of devices prepared by different kinds of anti-solvents. Fig 5.21 shows the performance distribution of devices fabricated by different kinds of anti-solvents under AM1.5G simulated solar illumination. The devices with pure alkanes as anti-solvents show very low efficiencies resulting from the poor quality of the perovskite layers. The performances of CB treated devices have a mean power conversion efficiency of 21.1% with a standard deviation of 0.52. In contrast, the performances of OCT/NCs processed devices have a mean power conversion efficiency of 22.2% with a standard deviation of 0.39. Therefore, OCT/NCs processed device shows higher efficiencies and narrower statistical distribution, benefited from the large grain size, preferred orientation and low surface roughness of perovskite layer.

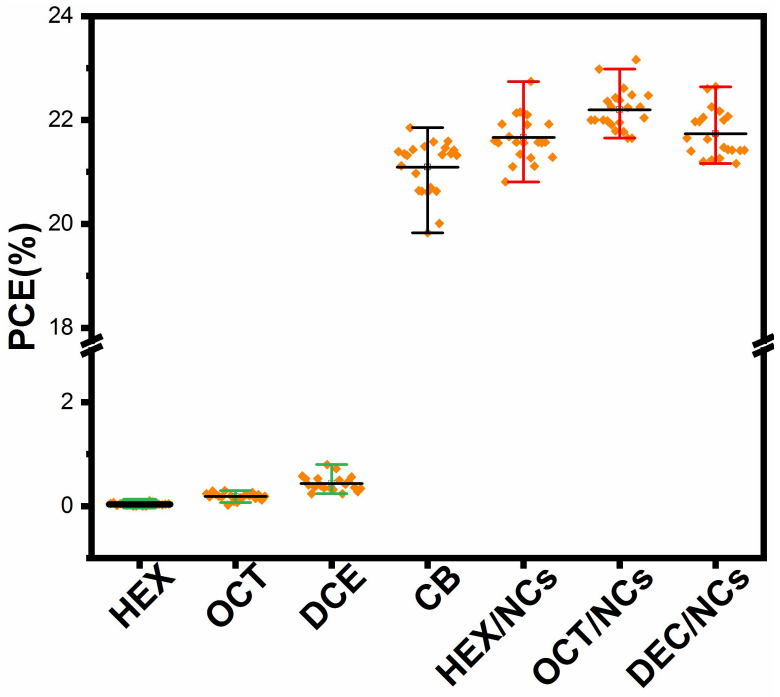

Fig 5.21 Power conversion efficiency distribution of devices fabricated by different

kinds of anti-solvents, showing the range and mean value of the data.

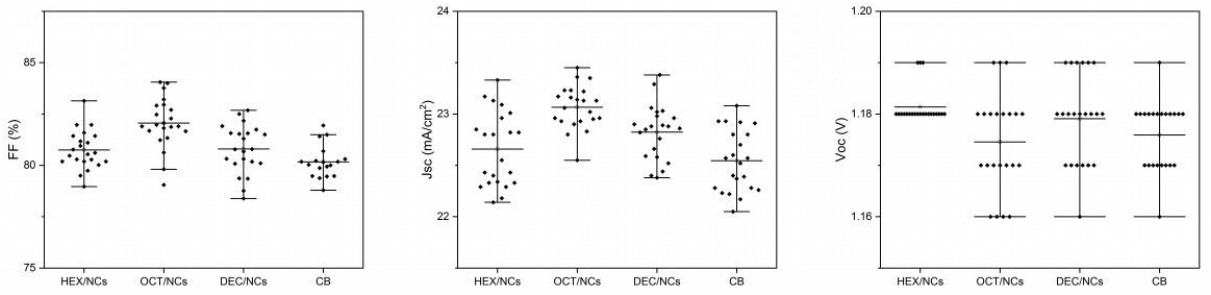

Fig 5.22 Distribution of J_{sc}, FF and V_{oc} of devices fabricated by different kinds of anti-solvents, showing the range and mean value of the data.

As we can see from fig 5.22, the enhancement of performance is mainly resulting from the improvement of fill factor (FF) and short-circuit current density (J_{sc}). The best CB process device achieved an efficiency of 21.6% (V_{oc}=1.18V, J_{sc}=22.9 mA/cm^2, and FF=80.06% as shown in fig 5.23. OCT/NCs processed devices shows the highest performance with average efficiency of 22.2%. The best-performing OCT/NCs processed devices achieved the PCE of 23.1% (V_{oc}=1.18V, J_{sc}=23.35mA/cm^2, and FF=84.05%) with a low hysteresis.

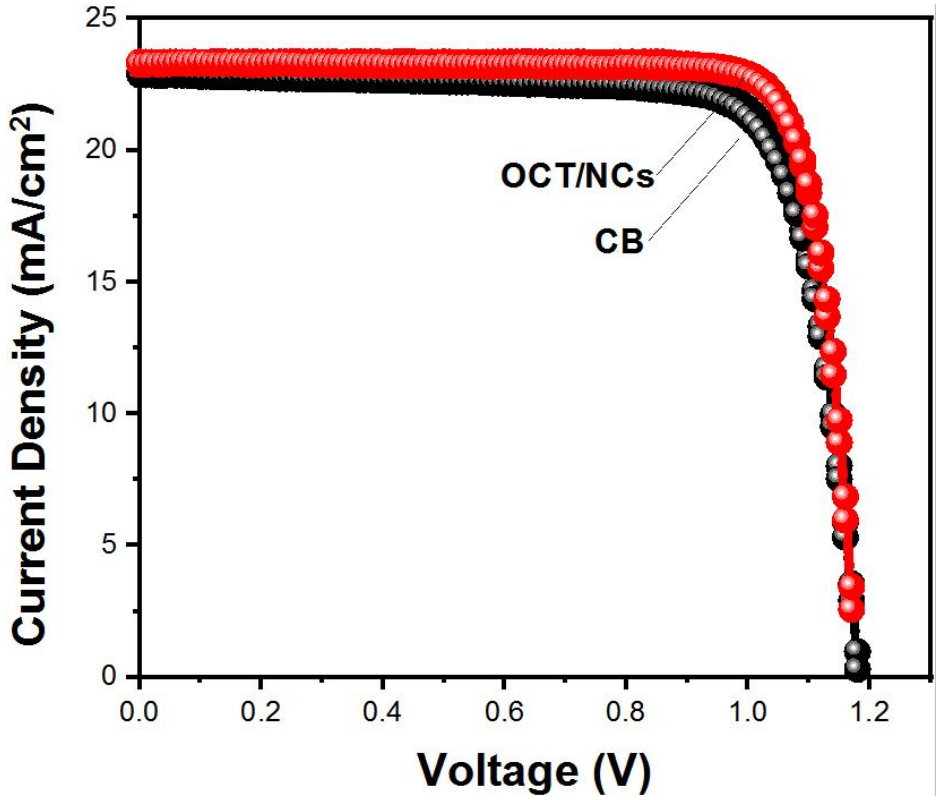

Fig 5.23 J-V curve of champion devices fabricated by CB and OCT/NCs.

The improvement of FF and J_{sc} benefits from the enhanced quality of the perovskite layer and reduced recombination centers. We also conducted time-resolved photoluminescence (TRPL) and steady photoluminescence (PL) characterization to study the ultrafast carrier dynamics and carrier recombination in perovskite films as shown in fig 5.24. The carriers' lifetime of perovskite films fabricated by OCT/NCs and CB are fitted to be 361.3 ns and 288.4 ns, indicating reduced numbers of non-radiative recombination centers in OCT/NCs processed films as shown in table 5.1. It is also coincident with the enhancement of photo-luminescence (PL) Intensity and blue shift of OCT/NCs treated films.

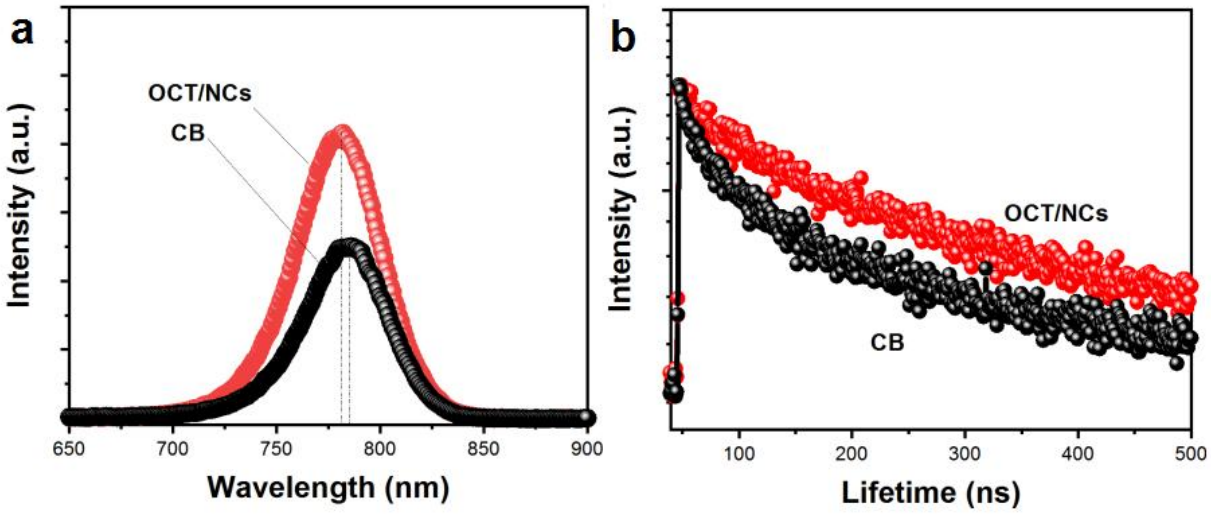

Fig 5.24 Results of time-resolved photoluminescence and steady photoluminescence.

Table 5.1 The fitted carrier lifetime of perovskite films obtained from the TRPL measurements.

Samples	B_1 [%]	τ_1 [ns]	B_2 [%]	τ_2 [ns]	$\tau_{average}$[ns]	R-Squared
CB	72.5±0.03	43.0±0.002	27.5±0.002	442.8±6	288.4	0.994
OCT/NCs	42.9±0.01	75.9±0.03	57.1±0.07	681.0±8	361.3	0.996

The blue shift of PL is further confirmed by UV-vis absorption spectrum, where OCT/NCs exhibits a sharper absorption edge, indicating a higher crystallinity as shown in fig 5.25.[128, 152, 153]

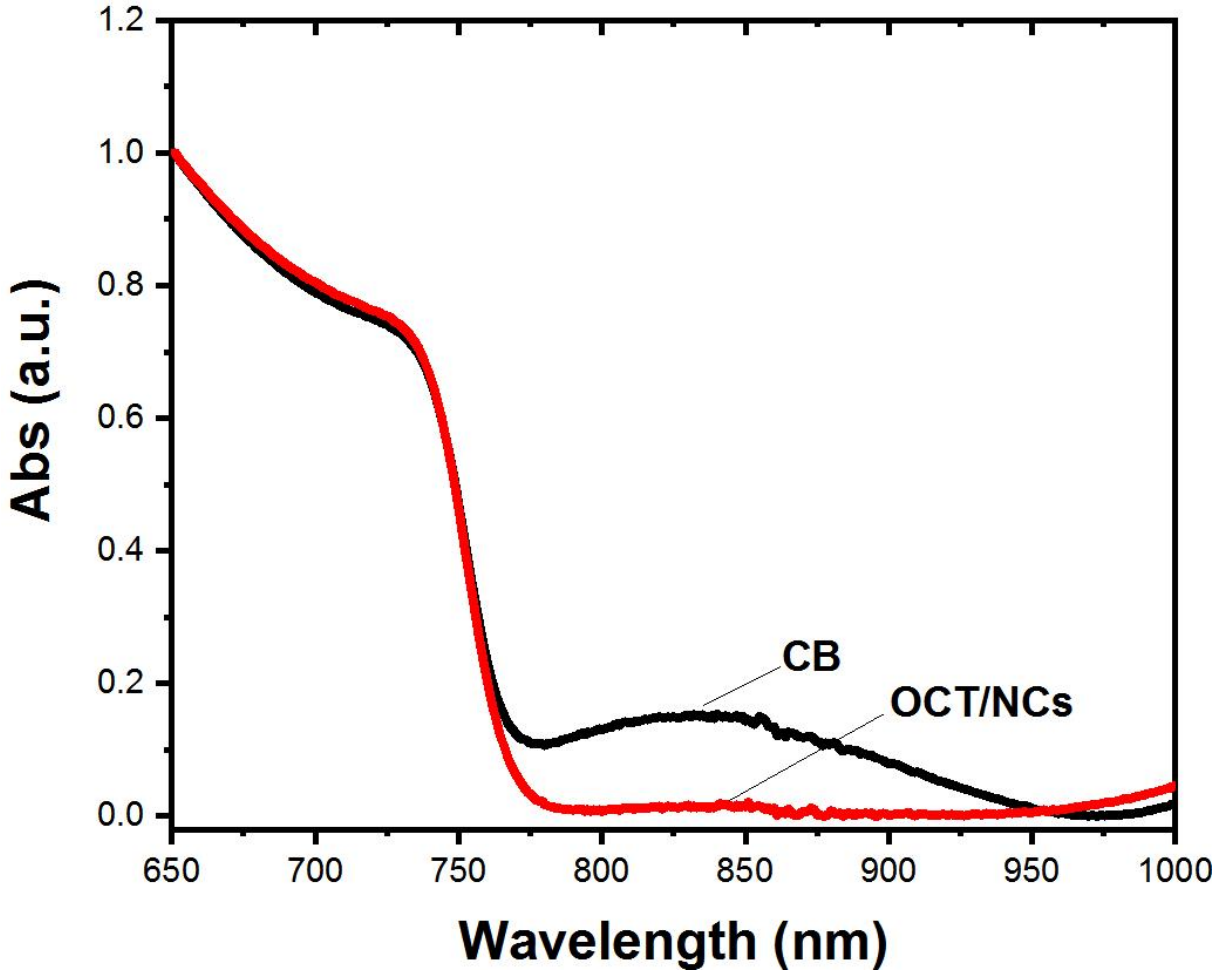

Fig 5.25 Ultraviolet and visible spectrum of CB and OCT/NCs process perovskite films.

To understand the charge recombination and transport in devices, we conducted transient photovoltage (TPV) and transit photo-current (TPC) measurements by irradiating the devices with a pulsed laser under open-circuit and short-circuit conditions.[153, 154] The recombination times obtained from the curves of photovoltage decay for devices fabricated by CB and OCT/NCs are 0.74 ms and 0.9 ms, respectively, indicating the reduced amount of recombination centers in OCT/NCs processed device as shown in fig 5.26a. At the same time, charge extracting times are evaluated by TPC measurements as shown in fig 5.26b. The decay times of

photocurrent for devices fabricated by CB and OCT/NC are 0.5 μs and 0.24 μs, respectively. The fast decay for charge extraction in TPC measurement indicates the reduction of charge recombination and the retarding of the recombination time, which is consistent with the high performance of OCT/NCs processed devices.

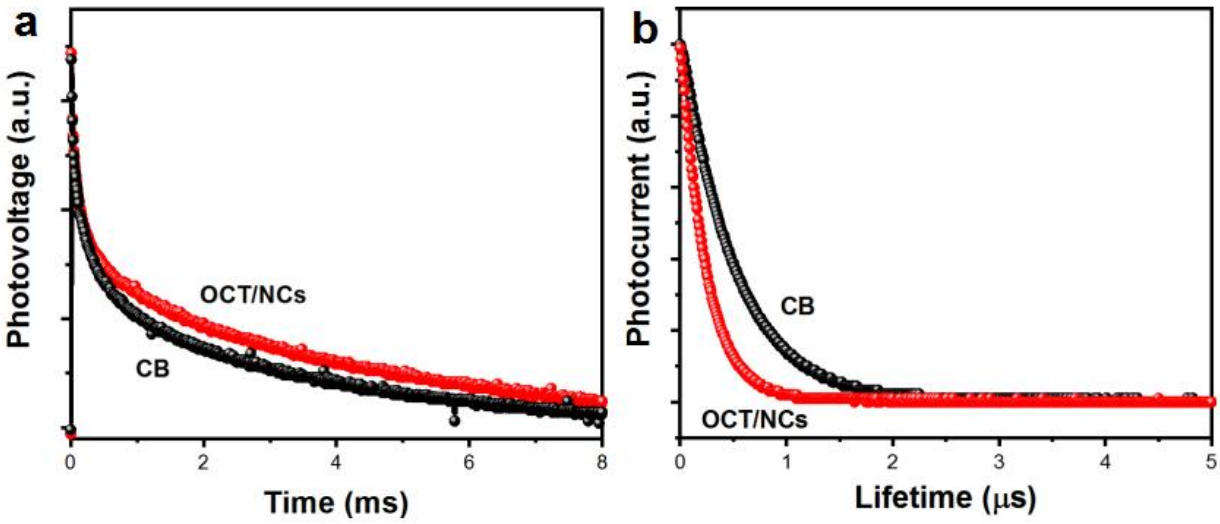

Fig 5.26 a) Transient photovoltage (TPV) decay and b) Transient photocurrent (TPC) decay of devices.

Moreover, electrochemical impedance spectroscopy (EIS) measurement has been further adopted to look more closely at carrier recombination. The low-frequency region is assigned to the recombination resistance (R_{rec}).[153] The larger R_{rec} of OCT/NCs devices indicates a lower recombination than CB processed devices as shown in fig 5.27.

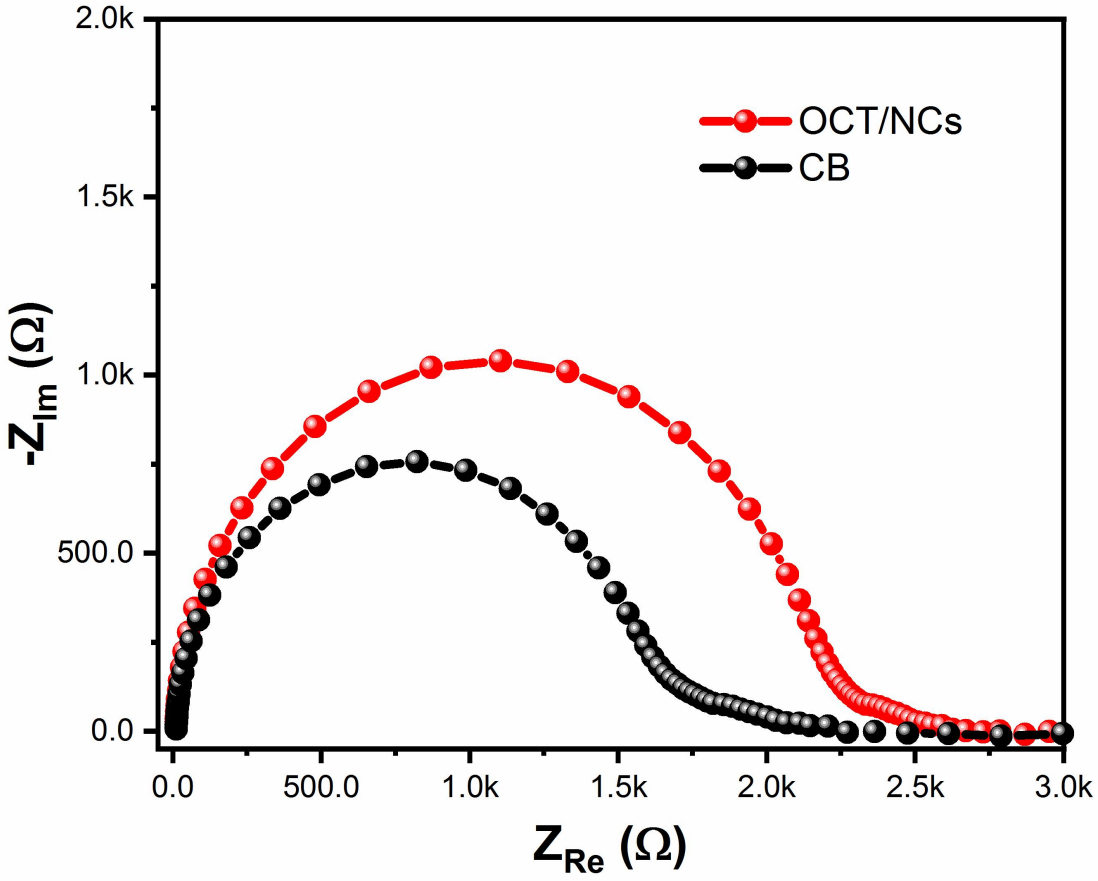

Fig 5.27 Nyquist plots of the PSCs based on CB and OCT/NCs processed devices, obtained with a bias of 0.98 V in the frequency range of 1 MHz to 0.1 Hz in dark.

The larger grain size and higher crystallinity of NCs anchored perovskite films are also expected to contribute to the stability of the perovskite. Moreover, the lattice anchoring effect has been proven to be an efficient way to enhance the phase stability of perovskite. Therefore, we compared the long-term PSC stability by MPP tracking measurements in ambient environment for encapsulated devices. The OCT/NCs processed device show much improved stability compared with the control CB devices as shown in fig 5.28.

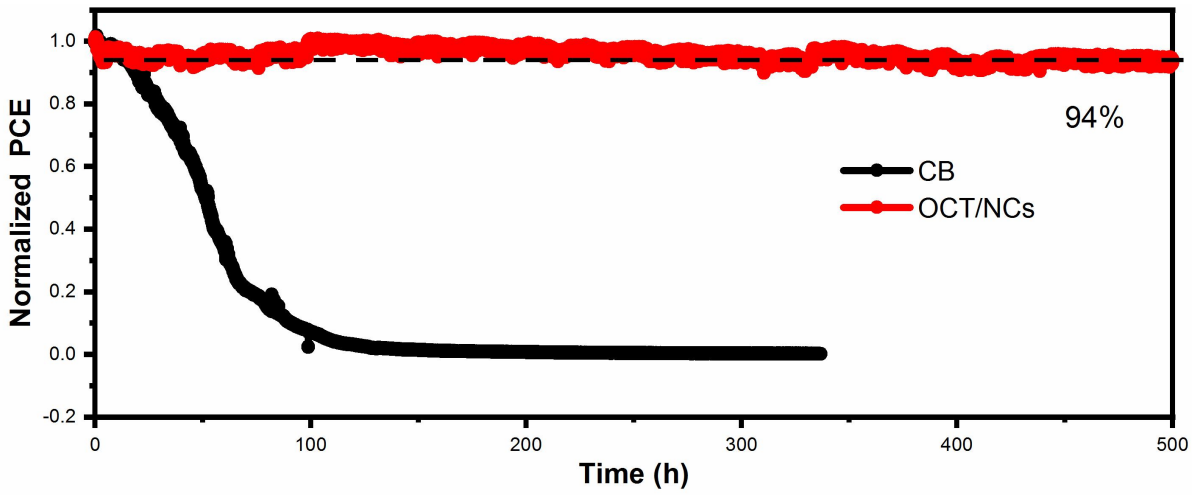

Fig 5.28 MPP-TD stability test of sealed devices in air atmosphere,showing vastly improved performance for the OCT/NCs processed films.

We also conducted PXRD measurements to study the stability of the perovskite layers relative to high-temperature and environmental moisture. The perovskite fabricated with different anti-solvents were heated in an inert atmosphere glove box for 3h and 6h at 100ºC. As a result, the signal of PbI_2 at 12.7º in CB processed films becomes a dominated phase in the PXRD pattern, which is triggered by the loss of volatile MA^+ above 80 ºC as shown in fig 5.29. However, the other peaks belong to the perovskite films show little changes, indicating the degradation of perovskite into PbI_2 is mainly happened on the surface of perovskite grains. In contrast, OCT/NCs processed perovskite films show excellent stability for the same thermal treatments.

Similar tests to study the moisture stability were conducted by placing the samples in ambient air with humidity between 60%-80% up to 48h as shown in fig 5.30, which reveals that the OCT/NC processed films are more robust than the control films to humidity.

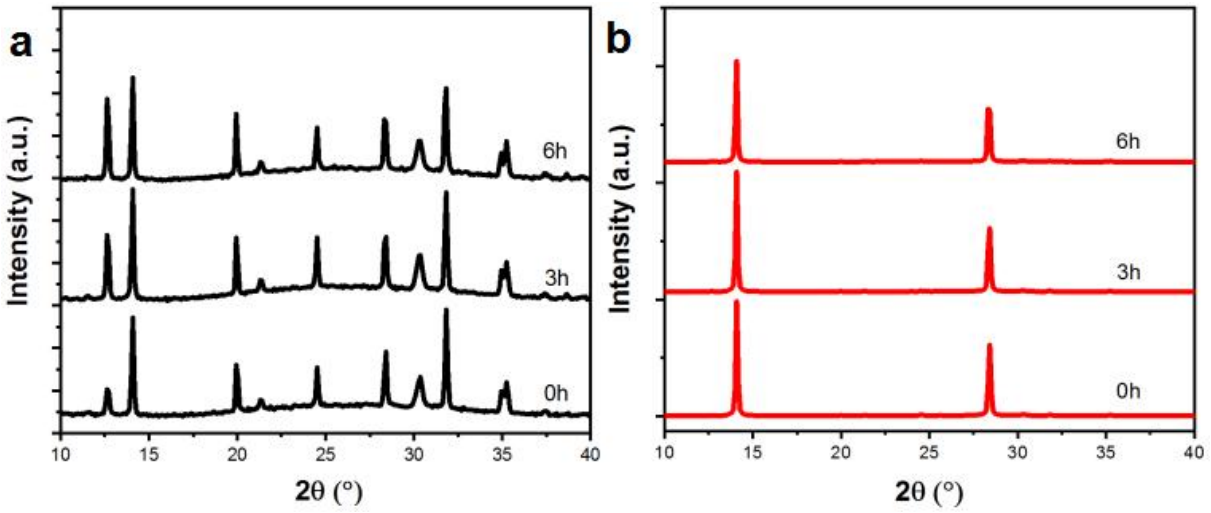

Fig 5.29 XRD pattern of (a) CB and (b) OCT/NCs processed perovskite films after annealing at 100°C in glove box for different time, showing the improvd stabilty for OCT/NCs processed perovskite films.

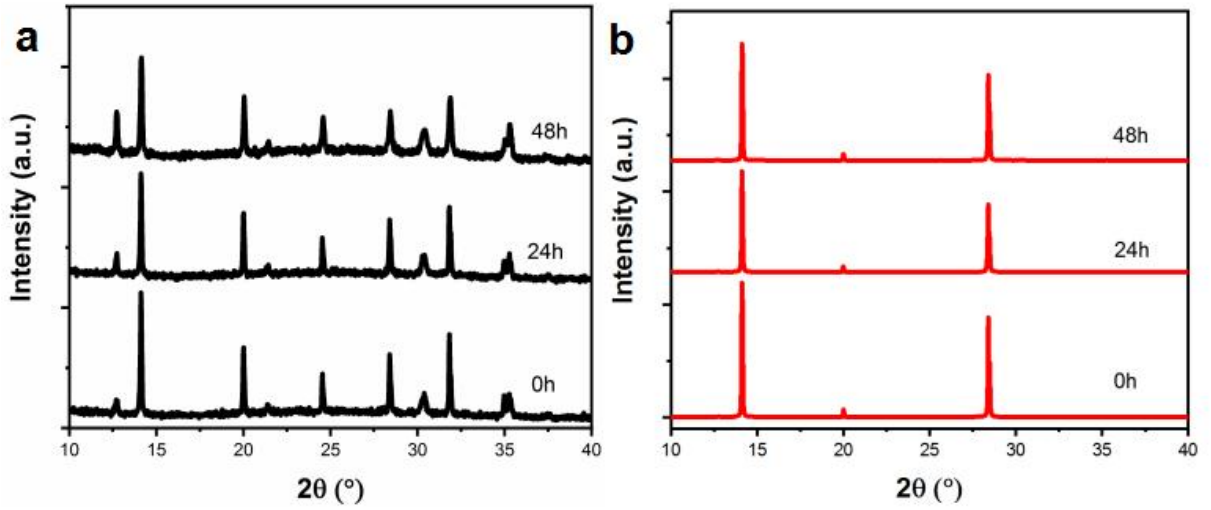

Fig 5.30 XRD pattern of (a) CB and (b) OCT/NCs processed perovskite films toward humidity by storage in air for different time, showing the improvd stabilty for OCT/NCs processed perovskite films.

5.5 Conclusions

The toxic substances used for the fabrication of perovskite solar cell has become a concern during the large scale commercialization process of perovskite solar cells.

Various low-toxicity anti-solvents have been studied in recent years, aiming to reduce the hazards to humans and the environment during large-scale industrial production.

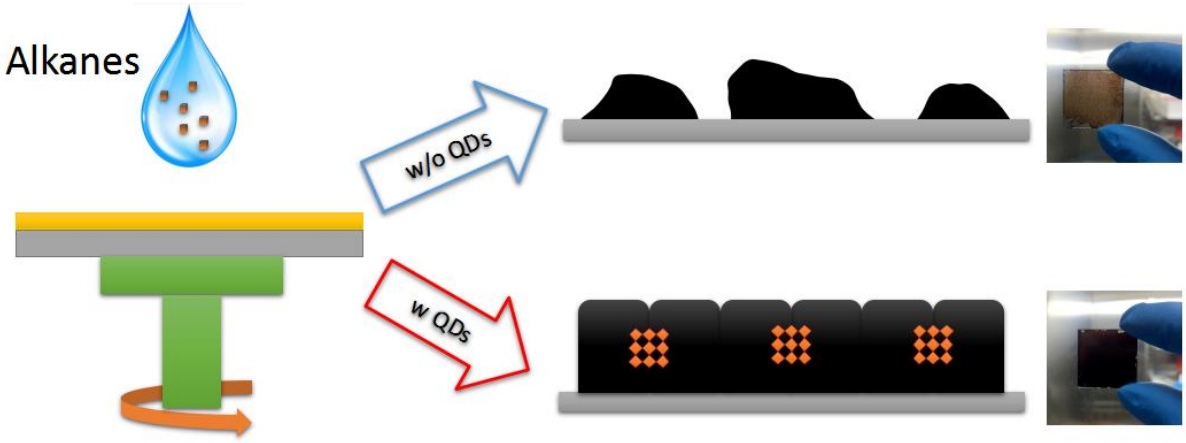

Fig 5.30 Demonstration of perovskite films fabricated by alkanes w/o and w/ $CsPbI_3$ NCs and optical photos of corresponding perovskite films.

However, limited low-toxicity solvents, such as EA, anisole and so on, are proven to be efficient to reduce the dependence on the widely used toxic CB and Tol. One of the most essential reasons is that the low-toxicity anti-solvent couldn't satisfy the strict requirement of self-nuclei formation process in high-quality perovskite films. To overcome this obstacle and establish more choices for low-toxicity anti-solvents, we reduce the dependence of perovskite films to self-nuclei formation process, by adding perovskite NCs as artificial seeds. In order to extend anti-solvents studies to alkanes, represented by hexane, octane and decane, are a class of low cost and low-toxicity non-polar solvents widely used in industry and daily life, but are inadequate on their own as proper anti-solvents because of their poor ability to boost the nuclei creation process in perovskite films. When $CsPbI_3$ NCs are added along with the alkane anti-solvents, the NCs could compensate the insufficient self-nuclei creation behavior

and result in a highly crystalline and dense film as shown in fig 5.30. Cryo-TEM results show that the matrix triple-cation perovskite film is epitaxially grown on NC seeds perfectly. Moreover, we find that OLA ligands dissociated from NCs surfaces work as surfactant in alkanes to wash off the DMSO and boost the self-nuclei process of the perovskite film. Devices prepared by low-toxicity alkanes with NCs are also compared with that prepared by commonly used CB. Benefiting from the larger grain size, better orientation, lower surface roughness and lower concentration of recombination centers, alkane/NCs processed devices show higher efficiency and better stability than traditional CB processed devices. More importantly, our method might open up a road map to explore more low-toxicity solvents as efficient anti-solvents for perovskite solar cells, and so bring greener commercialism a step closer.

6. Conclusions and further work

Although a lot of work has been reported on the successful stabilization of $CsPbI_3$ with metal ions substitution in the glove box, the problem is still unsolved when it comes to the synthesis without solvent and the stabilization of $CsPbI_3$ in ambient environment. We find the incorporation of other metal cations such as Bi^{3+} and Mn^{2+} make little contribution to the stabilization of $CsPbI_3$.Some of them seems to aid the formation of yellow phase at lower temperature and accelerate the decomposition of yellow phase into CsI and PbO at high temperature. Br^- doping is able to stabilize $CsPbI_3$ in air only for a few minutes, which lead to very weak signals of cubic phase in PXRD pattern. Interestingly, a cubic phase dominant black powder can be obtained by the synergic contribution of Br^- and MA^+/FA^+ cations. Neverless the results generally showed poor progress though the use of a studied solid state reaction route.Consequently, we moved to investigate solution reaction routine.

In this respect, we have shown a facile solution approach to prepare γ-$CsPbI_3$ micro-crystals in an ambient environment for the first time. The rapid precipitation process of γ-$CsPbI_3$ ensures the production of the desired perovskite phase at room-temperature, which is then stabilized by the spontaneous degradation of the perovskite toward water, which leads to the epitaxial growth of ultra-thin and single-crystalline PbI(OH) shell on the perovskite surface. The acetate anion is believed to play a key role controlling the degradation of perovskite to ensure formation of PbI(OH), while PVP contributes to capping the process and ensuring the PbIOH shell compactness and uniformity. These coated γ-$CsPbI_3$ microcrystals exhibit vastly improved stability both towards moisture and heating in air, which is attributed to the lattice anchoring and uniform physical coverage of PbI(OH) shell. Our

method has also been successfully extended to other inorganic perovskite with the synthesis of $CsPbI_2Br$. Benefiting from our room-temperature synthesis, $CsPbI_2Br$ forms the low-temperature *γ* perovskite phase, which represents the first experimental report of *γ*-$CsPbI_2Br$. Uniquely, our study provides a new avenue to the synthesis of stable solar perovskite materials, making use of degradation processes to form a protective stabilization layer on the perovskite. We have also tried to apply this approach to creat a passivation layer on top of perovskite films for solar cell. A huge challange is that the perovskite is poly-crysatlline, so that it is very hard to make sure the degradation happens on each grain uniformly. Further work could look to extend this approach into other compositions, as well as the other areas where a surface passivation layer may be formed to stablize new materials.

The toxic substances used for the fabrication of perovskite solar cell have become a concern during the large-scale commercialization process of perovskite solar cells. Various low-toxicity anti-solvents have been studied in recent years, aiming to reduce the hazards to humans and the environment during large-scale industrial production. However, limited low-toxicity solvents, such as EA and anisole, are proven to be efficient to reduce the dependence on the widely used toxic CB and Tol. One of the key reasons is that the low-toxicity anti-solvent couldn't satisfy the strict requirement of self-nuclei formation process in high-quality perovskite films. To overcome this obstacle and establish more choices for low-toxicity anti-solvents, we reduce the dependence of perovskite films to self-nuclei formation process, by adding perovskite NCs as artificial seeds. This then allows the use of alkanes, represented by hexane, octane and decane, as alternative low cost and low-toxicity non-polar solventsby overcoming their poor abilities to boost the nuclei creation process in perovskite films.

When $CsPbI_3$ NCs are added along with the alkane anti-solvents, the NCs could compensate the insufficient self-nuclei creation behavior and result in a highly crystalline and dense film. Cryo-TEM results show that the matrix triple-cation perovskite film is epitaxially grown on NC seeds perfectly. Moreover, we find that OLA ligands dissociated from NCs surface work as surfactant in alkane to wash off the DMSO and boost the self-nuclei process of the perovskite film. Devices prepared using low-toxicity alkane antisolvents with NCs were also compared with that prepared by commonly used CB. Benefiting from the larger grain size, better orientation, lower surface roughness and lower concentration of recombination centers, alkane/NCs processed devices show higher efficiency and better stability than traditional CB processed devices. More importantly, our method might open up a road map to explore more greener solvents as efficient anti-solvents for perovskite solar cells, and so bring greener commercialism a step closer. Further work in this area may extend this approach to Sn solar perovskite films, in order to overcome the toxic Pb.

7. References

1. A. K. Jena, A. Kulkarni and T. Miyasaka, *Chem. Rev.*, 2019, **119**, 3036-3103.
2. R. J. Sutton, M. R. Filip, A. A. Haghighirad, N. Sakai, B. Wenger, F. Giustino and H. J. Snaith, *ACS Energy Lett.*, 2018, **3**, 1787-1794.
3. Y. Fu, *Adv. Mater.*, 2022, **34**, 2108556.
4. A. Marronnier, G. Roma, S. Boyer-Richard, L. Pedesseau, J. M. Jancu, Y. Bonnassieux, C. Katan, C. C. Stoumpos, M. G. Kanatzidis and J. Even, *Acs Nano*, 2018, **12**, 3477-3486.
5. Y. Hassan, Y. Song, R. D. Pensack, A. I. Abdelrahman, Y. Kobayashi, M. A. Winnik and G. D. Scholes, *Adv. Mater.*, 2016, **28**, 566-573.
6. Z. Qiu, A. Mei, Y. Hu, Y. Rong and H. Han, *Appl. Phys. Lett.*, 2021, **119**, 250503.
7. Y. Jiang, E. J. Juarez-Perez, Q. Ge, S. Wang, M. R. Leyden, L. K. Ono, S. R. Raga, J. Hu and Y. Qi, *Mater. Horiz.*, 2016, **3**, 548-555.
8. W. Tian, H. Zhou and L. Li, *Small*, 2017, **13**, 1702107.
9. G. Tang, P. You, Q. Tai, A. Yang, J. Cao, F. Zheng, Z. Zhou, J. Zhao, P. K. L. Chan and F. Yan, *Adv. Mater.*, 2019, **31**, 1807689.
10. N.-G. Park, *Mater. Today*, 2015, **18**, 65-72.
11. B. Tang, Y. Hu, H. Dong, L. Sun, B. Zhao, X. Jiang and L. Zhang, *Angew. Chem.*, 2019, **131**, 16280-16286.
12. D. Wei, F. Ma, R. Wang, S. Dou, P. Cui, H. Huang, J. Ji, E. Jia, X. Jia and S. Sajid, *Adv. Mater.*, 2018, **30**, 1707583.
13. W. Kim, S. K. Kim, S. Jeon, J. Ahn, B. K. Jung, S. Y. Lee, C. Shin, T. Y. Seong, S. Jeong and H. S. Jang, *Adv. Funct. Mater.*, 2022, 2111409.

14. A. Ray, B. Martín-García, A. Moliterni, N. Casati, K. M. Boopathi, D. Spirito, L. Goldoni, M. Prato, C. Giacobbe and C. Giannini, *Adv. Mater.*, 2022, 2106160.

15. J. Pan, Z. Zhao, F. Fang, L. Wang, G. Wang, C. Liu, Q. Huang, J. Sun, Y. Huang and L. Mao, *Adv Opt. Mater.*, 2022, 2102569.

16. J. Wei, L. Tao, L. Li, M. Yan, C. Wang, W. Sun, D. Yang and Y. Fang, *Adv Opt. Mater.*, 2022, **10**, 2102320.

17. P. Jia, L. Qin, D. Zhao, Y. Tang, B. Song, J. Guo, X. Li, L. Li, Q. Cui and Y. Hu, *Adv. Funct. Mater.*, 2021, **31**, 2107125.

18. Q. Zhou, L. Liang, J. Hu, B. Cao, L. Yang, T. Wu, X. Li, B. Zhang and P. Gao, *Adv. Energy Mater.*, 2019, **9**, 1802595.

19. B. W. Boote, H. P. Andaraarachchi, B. A. Rosales, R. Blome-Fernández, F. Zhu, M. D. Reichert, K. Santra, J. Li, J. W. Petrich, J. Vela and E. A. Smith, *ChemSusChem*, 2019, **20**, 2647-2656.

20. A. R. Chakhmouradian and P. M. Woodward, *Phys. Chem. Minerals*, 2014, **41**, 387-391.

21. L. Hu, W. Zhao, W. Duan, G. Chen, B. Fan and X. Zhang, *Micromachines*, 2022, **13**, 457.

22. S. Shukla, S. Shukla, L. J. Haur, S. S. Dintakurti, G. Han, A. Priyadarshi, T. Baikie, S. G. Mhaisalkar and N. Mathews, *ChemSusChem*, 2017, **10**, 3804-3809.

23. X. Du, R. Qiu, T. Zou, X. Chen, H. Chen and H. Zhou, *Adv Mater. Interfaces*, 2019, **6**, 1900413.

24. Q. Chen, J. Luo, R. He, H. Lai, S. Ren, Y. Jiang, Z. Wan, W. Wang, X. Hao and Y. Wang, *Adv. Energy Mater.*, 2021, **11**, 2101045.

25. W. F. Yang, F. Igbari, Y. H. Lou, Z. K. Wang and L. S. Liao, *Adv. Energy Mater.*, 2020, **10**, 1902584.

26. S. Gu, R. Lin, Q. Han, Y. Gao, H. Tan and J. Zhu, *Adv. Mater.*, 2020, **32**, 1907392.

27. C. Li, Z. Song, D. Zhao, C. Xiao, B. Subedi, N. Shrestha, M. M. Junda, C. Wang, C. S. Jiang and M. Al. Jassim, *Adv. Energy Mater.*, 2019, **9**, 1803135.

28. T. Mahmoudi, W. Y. Rho, M. Kohan, Y. H. Im, S. Mathur and Y.-B. Hahn, *Nano Energy*, 2021, **90**, 106495.

29. E. Mosconi, B. Merabet, D. Meggiolaro, A. Zaoui and F. De Angelis, *The J. Phys. Chem. C*, 2018, **122**, 14107-14112.

30. R. Ali, G. J. Hou, Z. G. Zhu, Q.-B. Yan, Q. R. Zheng and G. Su, *J. Mater. Chem. A*, 2018, **6**, 9220-9227.

31. H. Zhang, H. Wang, S. T. Williams, D. Xiong, W. Zhang, C. C. Chueh, W. Chen and A. K. Y. Jen, *Adv. Mater.*, 2017, **29**, 1606608.

32. H. Shankar, A. Jha and P. Kar, *Mater. Adv*, 2022, **3**, 658-664.

33. Z. Chen, H. He, Z. Wen, Z. Cui, S. Mei, D. Yang, X. Wei, W. Zhang, F. Xie and B. Yang, *Mater. Sci. Eng. B*, 2021, **273**, 115426.

34. B. Su, G. Zhou, J. Huang, E. Song, A. Nag and Z. Xia, *Laser & Photonics Rev.*, 2021, **15**, 2000334.

35. S. Zhang, M.-C. Tang, N. V. Nguyen, T. D. Anthopoulos and C. A. Hacker, *ACS Appl. Electron. Mater.*, 2021, **3**, 2277-2285.

36. Y. Li, D. Song, J. Meng, J. Dong, Y. Lu, X. Huo, A. Maqsood, Y. Song, S. Zhao and B. Qiao, *J. Mater. Sci*, 2020, **55**, 9787-9794.

37. D. Wang, D. Wu, D. Dong, W. Chen, J. Hao, J. Qin, B. Xu, K. Wang and X. Sun, *Nanoscale*, 2016, **8**, 11565-11570.

38. S. Shi, Y. Li, X. Li and H. Wang, *Mater.Horiz.*, 2015, **2**, 378.

39. Q. A. Akkerman and L. Manna, *ACS Energy Lett.*, 2020, **5**, 604-610.

40. H. Dong, C. Zhang, X. Liu, J. Yao and Y. S. Zhao, *Chem. Soc. Rev.*, 2020, **49**, 951-982.

41. W. Li, Z. Wang, F. Deschler, S. Gao, R. H. Friend and A. K. Cheetham, *Nature Rev. Mater.*, 2017, **2**, 16099.

42. Y. Fu, H. Zhu, J. Chen, M. P. Hautzinger, X. Y. Zhu and S. Jin, *Nature Rev. Mater.*, 2019, **4**, 169-188.

43. B. Wang, N. Novendra and A. Navrotsky, *J. Am. Chem. Soc.*, 2019, **141**, 14501-14504.

44. Y. Wang, M. I. Dar, L. K. Ono, T. Zhang, M. Kan, Y. Li, L. Zhang, X. Wang, Y. Yang and X. Gao, *Science*, 2019, **365**, 591-595.

45. V. M. Goldschmidt, *Naturwissenschaften*, 1926, **14**, 477-485.

46. W. S. Subhani, K. Wang, M. Du and S. F. Liu, *Nano energy*, 2019, **61**, 165-172.

47. Y. Fu, M. P. Hautzinger, Z. Luo, F. Wang, D. Pan, M. M. Aristov, I. A. Guzei, A. Pan, X. Zhu and S. Jin, *ACS central sci.*, 2019, **5**, 1377-1386.

48. H. Meyers and H. Myers, *Introductory solid state physics*, CRC press, 1997.

49. D. W. Snoke, *Solid state physics: Essential concepts*, Cambridge University Press, 2020.

50. J. D. Patterson and B. C. Bailey, *Solid-state physics: introduction to the theory*, Springer Science & Business Media, 2007.

51. T. M. Brenner, D. A. Egger, L. Kronik, G. Hodes and D. Cahen, *Nat. Rev. Mater.*, 2016, **1**, 1-16.

52. H. S. Jung and N. G. Park, *Small*, 2015, **11**, 10-25.

53. W. Gao, X. Gao, T. A. Abtew, Y. Y. Sun, S. Zhang and P. Zhang, *Phys. Rev. B*, 2016, **93**, 085202.

54. T. Umebayashi, K. Asai, T. Kondo and A. Nakao, *Phys. Rev. B*, 2003, **67**, 155405.

55. A. Amat, E. Mosconi, E. Ronca, C. Quarti, P. Umari, M. K. Nazeeruddin, M. Grätzel and F. De Angelis, *Nano Lett.*, 2014, **14**, 3608-3616.

56. W. Ahmad, J. Khan, G. Niu and J. Tang, *Solar RRL*, 2017, **1**, 1700048.

57. G. Xing, N. Mathews, S. S. Lim, N. Yantara, X. Liu, D. Sabba, M. Grätzel, S. Mhaisalkar and T. C. Sum, *Nat. Mater.*, 2014, **13**, 476-480.

58. P. T. Lai, H. C. Lin, Y. T. Chuang, C. Y. Chen, W. K. Cheng, G. -H. Tan, B. W. Hsu, L. Yang, S. C. Lou and L. J. Chien, *ACS Appl. Mater. & Interfaces*, 2022.

59. J. Wu, L. Wang, A. Feng, S. Yang, N. Li, X. Jiang, N. Liu, S. Xie, X. Guo and Y. Fang, *Adv. Funct. Mater.*, 2022, **32**, 2109149.

60. S. Basak, O. Bar On and J. Scheuer, *Opt. Mater. Exp.*, 2022, **12**, 375-382.

61. Y. Wu, B. Huang, Z. Meng, S. Zhang and S. Wu, *Chem. Eng. J.*, 2022, **432**, 134409.

62. D. Zhang, Q. Zhang, B. Ren, Y. Zhu, M. Abdellah, Y. Fu, B. Cao, C. Wang, L. Gu and Y. Ding, *Nature Photonics*, 2022, **16**, 284-290.

63. E. Smecca, Y. Numata, I. Deretzis, G. Pellegrino, S. Boninelli, T. Miyasaka, A. La Magna and A. Alberti, *PCCP*, 2016, **18**, 13413-13422.

64. G. E. Eperon, S. D. Stranks, C. Menelaou, M. B. Johnston, L. M. Herz and H. J. Snaith, *Science*, 2014, **7**, 982-988.

65. J. Carrillo, A. Guerrero, S. Rahimnejad, O. Almora, I. Zarazua, E. Mas-Marza, J. Bisquert and G. Garcia-Belmonte, *Adv. Energy Mater.*, 2016, **6**, 1502246.

66. F. X. Xie, D. Zhang, H. Su, X. Ren, K. S. Wong, M. Grätzel and W. C. Choy, *Acs Nano*, 2015, **9**, 639-646.

67. J. Gong, P. Guo, S. E. Benjamin, P. G. Van Patten, R. D. Schaller and T. Xu, *J. Eng. Chem*, 2018, **27**, 1017-1039.

68. Z. Yao, W. Zhao and S. F. Liu, *J. Mater. Chem. A*, 2021, **9**, 11124-11144.

69. Z. Gu, Z. Huang, C. Li, M. Li and Y. Song, *Sci. Adv.*, 2018, **4**, eaat2390.

70. L. Meng, Z. Wei, T. Zuo and P. Gao, *Nano Energy*, 2020, **75**, 104866.

71. D. B. Straus, S. Guo, A. M. Abeykoon and R. J. Cava, *Adv. Mater.*, 2020, **32**, 2001069.

72. Z. Xiao, W. Meng, J. Wang and Y. Yan, *ChemSusChem*, 2016, **9**, 2628-2633.

73. Zhao, B. Zhao, S. F. Jin, S. Huang, N. Liu, J. Y. Ma, D. J. Xue, Han, Q. Han, J. Ding, Y. Feng, J. S. Hu, *J. Am. Chem. Soc.* 2018, **140** (37), 11716-11725.

74. R. J. Sutton, M. R. Filip, A. A. Haghighirad, N. Sakai, B. Wenger, F. Giustino and H. J. Snaith, *ACS Energy Lett.*, 2018, **3**, 1787-1794.

75. Q. Ye, F. Ma, Y. Zhao, S. Yu, Z. Chu, P. Gao, X. Zhang and J. You, *Small*, 2020, **16**, 2005246.

76. M. Li, X. Zhang, P. Wang and P. Yang, *The J. Phys. Chem. C*, 2021, **125**, 7109-7118.

77. J. K. Sun, S. Huang, X. Z. Liu, Q. Xu, Q. H. Zhang, W. J. Jiang, D. J. Xue, J. C. Xu, J. Y. Ma and J. Ding, J. Am. CHEM. 2018, **140**, 11705-11715.

78. R. Chen, Y. Hui, B. Wu, Y. Wang, X. Huang, Z. Xu, P. Ruan, W. Zhang, F. Cheng and W. Zhang, *J. Mater. Chem. Soc.*, 2020, **8**, 9597-9606.

79. E. M. Sanehira, A. R. Marshall, J. A. Christians, S. P. Harvey, P. N. Ciesielski, L. M. Wheeler, P. Schulz, L. Y. Lin, M. C. Beard and J. M. Luther, *Sci. Adv.*, 2017, **3**, eaao4204.

80. G. E. Eperon, G. M. Paterno, R. J. Sutton, A. Zampetti, A. A. Haghighirad, F. Cacialli and H. J. Snaith, *J. Mater. Chem. A*, 2015, **3**, 19688-19695.

81. W. Ke, I. Spanopoulos, C. C. Stoumpos and M. G. Kanatzidis, *Nat. Commun.*, 2018, **9**, 4785.

82. J. Navas, A. Sánchez-Coronilla, J. J. Gallardo, N. Cruz Hernández, J. C. Piñero, R. Alcántara, C. Fernández-Lorenzo, D. M. De los Santos, T. Aguilar and J. Martín-Calleja, *Nanoscale*, 2015, **7**, 6216-6229.

83. J. K. Nam, M. S. Jung, S. U. Chai, Y. J. Choi, D. Kim and J. H. Park, *J. Phys. Chem. Lett.*, 2017, **8**, 2936-2940.

84. J. P. Correa-Baena, A. Abate, M. Saliba, W. Tress, T. J. Jacobsson, M. Grätzel, A. J. E. Hagfeldt and E. *Science*, 2017, **10**, 710-727.

85. L. Meng, J. You, T. F. Guo and Y. Yang, *Acc. Chem. Res.*, 2016, **49**, 155-165.

86. C. Zuo, H. J. Bolink, H. Han, J. Huang, D. Cahen and L. Ding, *Adv. Sci.*, 2016, **3**, 1500324.

87. H. S. Kim and N. G. Park, *J. Phys. Chem. Lett.*, 2014, **5**, 2927-2934.

88. P. Ru, E. Bi, Y. Zhang, Y. Wang, W. Kong, Y. Sha, W. Tang, P. Zhang, Y. Wu, W. Chen, X. Yang, H. Chen and L. Han, *Adv. Energy Mater.*, 2020, **10**, 1903487.

89. W. Chen, L. Xu, X. Feng, J. Jie and Z. He, *Adv. Mater.*, 2017, **29**, 1603923.

90. N. Arora, M. I. Dar, A. Hinderhofer, N. Pellet, F. Schreiber, S. M. Zakeeruddin and M. Grätzel, *Science*, 2017, **358**, 768-771.

91. Y. Xia and S. Dai, *J. Mater. Sci-Mater. El.*, 2021, **32**, 12746-12757.

92. Y. Kim, E. H. Jung, G. Kim, D. Kim, B. J. Kim and J. Seo, *Adv. Energy Mater.*, 2018, **8**, 1801668.

93. W. H. Nguyen, C. D. Bailie, E. L. Unger and M. D. McGehee, *J. Am. Chem. Soc.*, 2014, **136**, 10996-11001.

94. Q. Jiang, X. Zhang and J. You, *Small*, 2018, **14**, 1801154.

95. R. Long, W. H. Fang and O. V. Prezhdo, *The J. Phys. Chem. C*, 2017, **121**, 3797-3806.

96. C. Quarti, F. De Angelis and D. Beljonne, *Chem. Mater.*, 2017, **29**, 958-968.

97. C. H. Chiang and C. G. Wu, *Nat. Photonics*, 2016, **10**, 196-200.

98. Y. Zhou, J. Chen, O. M. Bakr and H. T. Sun, *Chem. Mater.*, 2018, **30**, 6589-6613.

99. A. L. Abdelhady, M. I. Saidaminov, B. Murali, V. Adinolfi, O. Voznyy, K. Katsiev, E. Alarousu, R. Comin, I. Dursun and L. Sinatra, *J. Phys. Chem Lett.*, 2016, **7**, 295-301.

100. Y. Hu, F. Bai, X. Liu, Q. Ji, X. Miao, T. Qiu and S. Zhang, *ACS Energy Lett.*, 2017, **2**, 2219-2227.

101. C. Liu, W. Li, H. Li, H. Wang, C. Zhang, Y. Yang, X. Gao, Q. Xue, H. L. Yip and J. Fan, *Adv. Energy Mater.*, 2019, **9**, 1803572.

102. Q. A. Akkerman, D. Meggiolaro, Z. Dang, F. De Angelis and L. Manna, *ACS Energy Lett.*, 2017, **2**, 2183-2186.

103. W. van der Stam, J. J. Geuchies, T. Altantzis, K. H. W. van den Bos, J. D. Meeldijk, S. Van Aert, S. Bals, D. Vanmaekelbergh and C. de Mello Donega, *J. Am. Chem. Soc.*, 2017, **139**, 4087-4097.

104. G. Pan, X. Bai, D. Yang, X. Chen, P. Jing, S. Qu, L. Zhang, D. Zhou, J. Zhu and W. Xu, *Nano Lett.*, 2017, **17**, 8005-8011.

105. A. K. Jena, A. Kulkarni, Y. Sanehira, M. Ikegami and T. Miyasaka, *Chem. Mater.*, 2018, **30**, 6668-6674.

106. S. Xiang, W. Li, Y. Wei, J. Liu, H. Liu, L. Zhu and H. Chen, *Nanoscale*, 2018, **10**, 9996-10004.

107. L. Dimesso, M. Wussler, T. Mayer, E. Mankel and W. Jaegermann, *AIMS Mater. Sci.*, 2016, **3**, 737-755.

108. C. F. J. Lau, M. Zhang, X. Deng, J. Zheng, J. Bing, Q. Ma, J. Kim, L. Hu, M. A. Green, S. Huang and A. Ho-Baillie, *ACS Energy Lett.*, 2017, **2**, 2319-2325.

109. T. Zhang, M. I. Dar, G. Li, F. Xu, N. Guo, M. Gratzel and Y. Zhao, *Sci. Adv.*, 2017, **3**, e1700841.

110. J. Burschka, N. Pellet, S. J. Moon, R. Humphry-Baker, P. Gao, M. K. Nazeeruddin and M. J. N. Grätzel, *Nature*, 2013, **499**, 316.

111. H. Tan, A. Jain, O. Voznyy, X. Lan, F. P. G. De Arquer, J. Z. Fan, R. Quintero-Bermudez, M. Yuan, B. Zhang and Y. J. S. Zhao, *Science*, 2017, **355**, 722-726.

112. W. S. Yang, B.-W. Park, E. H. Jung, N. J. Jeon, Y. C. Kim, D. U. Lee, S. S. Shin, J. Seo, E. K. Kim and J. H. J. S. Noh, *Science*, 2017, **356**, 1376-1379.

113. J. A. Christians, P. A. Miranda Herrera and P. V. Kamat, *J. Am. Chem. Soc.*, 2015, **137**, 1530-1538.

114. B. Conings, J. Drijkoningen, N. Gauquelin, A. Babayigit, J. D'Haen, L. D'Olieslaeger, A. Ethirajan, J. Verbeeck, J. Manca and E. Mosconi, *Adv. Energy Mater.*, 2015, **5**, 1500477.

115. Y. Wang, T. Zhang, M. Kan and S. Zhao, 2018, *J. Am. Chem. Soc.,* **140**, 12345-12348.

116. J. A. Steele, H. Jin, I. Dovgaliuk, R. F. Berger, T. Braeckevelt, H. Yuan, C. Martin, E. Solano, K. Lejaeghere and S. M. Rogge, *Science*, 2019, **365**, 679-684.

117. B. Zhao, S. F. Jin, S. Huang, N. Liu, J. Y. Ma, D. J. Xue, Q. Han, J. Ding, Q. Q. Ge, Y. Feng and J. S. Hu, *J. Am. Chem. Soc.*, 2018, **140**, 11716-11725.

118. J. Zhang, D. Bai, Z. Jin, H. Bian, K. Wang, J. Sun, Q. Wang and S. Liu, *Adv. Energy Mater.,* 2018, **8**, 1703246.

119. H. Zhao, J. Xu, S. Zhou, Z. Li, B. Zhang, X. Xia, X. Liu, S. Dai and J. Yao, *Adv. Funct. Mater.*, 2019, 1808986.

120. P. Becker, J. A. Márquez, J. Just, A. Al-Ashouri, C. Hages, H. Hempel, M. Jošt, S. Albrecht, R. Frahm and T. Unold, *Adv. Energy Mater.*, 2019, **9**, 1900555.

121. E. M. Sanehira, A. R. Marshall, J. A. Christians, S. P. Harvey, P. N. Ciesielski, L. M. Wheeler, P. Schulz, L. Y. Lin, M. C. Beard and J. M. Luther, *Sci. Adv.*, 2017, **3**, eaao4204.

122. B. Li, Y. Zhang, L. Fu, T. Yu, S. Zhou, L. Zhang and L. Yin, *Nat. Commun.*, 2018, **9**, 1076.

123. D. B. Straus, S. Guo and R. J. Cava, *J. Am. Chem. Soc.*, 2019, 9b06055.

124. G. Yuan, C. Ritchie, M. Ritter, S. Murphy, D. E. Gómez and P. Mulvaney, *J. Phys. Chem. C*, 2017, **122**, 13407-13415.

125. J. Dennis, H. Henisch and P. Cherin, *J. Electrochem. Soc.*, 1965, **112**, 1240-1241.

126. Y. Chen, Y. Lei, Y. Li, Y. Yu, J. Cai, M. H. Chiu, R. Rao, Y. Gu, C. Wang and W. Choi, *Nature*, 2020, **577**, 209-215.

127. Y. Chen, T. Shi, P. Liu, W. Xie, K. Chen, X. Xu, L. Shui, C. Shang, Z. Chen, H.-L. Yip, G. Zhou and X. Wang, *J. Mater. Chem. A*, 2019, **7**, 20201-20207.

128. Z. Li, B. Li, X. Wu, S. A. Sheppard, S. Zhang, D. Gao, N. J. Long and Z. Zhu, *Science*, 2022, **376**, 416-420.

129. S. Tan, T. Huang, I. Yavuz, R. Wang, T. W. Yoon, M. Xu, Q. Xing, K. Park, D. K. Lee, C. H. Chen, R. Zheng, T. Yoon, Y. Zhao, H. C. Wang, D. Meng, J. Xue, Y. J. Song, X. Pan, N. G. Park, J. W. Lee and Y. Yang, *Nature*, 2022, **605**, 268-273.

130. M. Zhang, Z. Wang, B. Zhou, X. Jia, Q. Ma, N. Yuan, X. Zheng, J. Ding and W. H. Zhang, *Solar RRL*, 2018, **2**, 1700213.

131. M. T. Hoang, F. Ünlü, W. Martens, J. Bell, S. Mathur and H. Wang, *Green Chem.*, 2021, **23**, 5302-5336.

132. T. Bu, L. Wu, X. Liu, X. Yang, P. Zhou, X. Yu, T. Qin, J. Shi, S. Wang, S. Li, Z. Ku, Y. Peng, F. Huang, Q. Meng, Y. B. Cheng and J. Zhong, *Adv. Energy Mater.*, 2017, **7**, 1700576.

133. M. Wang, Q. Fu, L. Yan, J. Huang, Q. Ma, M. Humayun, W. Pi, X. Chen, Z. Zheng and W. Luo, *Chem. Eng. J.*, 2020, **387**, 123966.

134. S. Ghosh, S. Mishra and T. Singh, *Adv. Mater. Interfaces*, 2020, **7**, 2000950.

135. J. Sun, F. Li, J. Yuan and W. Ma, *Small Methods*, 2021, **5**, 2100046.

136. H. Chen, Z. Wei, H. He, X. Zheng, K. S. Wong and S. Yang, *Adv. Energy Mater.*, 2016, **6**, 1502087.

137. H. B. Lee, M. K. Jeon, N. Kumar, B. Tyagi and J. W. Kang, *Adv. Funct. Mater.*, 2019, **29**, 1903213.

138. N. Lin, J. Qiao, H. Dong, F. Ma and L. Wang, *J. Mater. Chem. A*, 2015, **3**, 22839-22845.

139. A. Swarnkar, A. R. Marshall, E. M. Sanehira, B. D. Chernomordik, D. T. Moore, J. A. Christians, T. Chakrabarti and J. M. Luther, *Science*, 2016, **354**, 92-95.

140. Q. Hu, W. Chen, W. Yang, Y. Li, Y. Zhou, B. W. Larson, J. C. Johnson, Y. H. Lu, W. Zhong and J. Xu, *Joule*, 2020, **4**, 1575-1593.

141. A. Jana, A. Meena, S. A. Patil, Y. Jo, S. Cho, Y. Park, V. G. Sree, H. Kim, H. Im and R. A. Taylor, *Prog. Mater. Sci.*, 2022, **129**, 100975.

142. Z. Yang, W. Zhang, S. Wu, H. Zhu, Z. Liu, Z. Liu, Z. Jiang, R. Chen, J. Zhou, Q. Lu, Z. Xiao, L. Shi, H. Chen, L. K. Ono, S. Zhang, Y. Zhang, Y. Qi, L. Han and W. Chen, *Sci. Adv.*, 2021, **7**, eabg3749.

143. C. Chen, Z. W. Zhou, Y. Jiang, Y. C. Feng, Y. Fang, J. Y. Liu, M. J. Chen, J. M. Liu, J. W. Gao, and S. P. Feng, *ACS Appl. Mater. Interfaces*, 2022, **14**, 17348−17357.

144. W. Zhang, Y. Li, X. Liu, D. Tang, X. Li and X. Yuan, *Chem. Eng. J.*, 2020, **379**, 122298.

145. Z. Ning, X. Gong, R. Comin, G. Walters, F. Fan, O. Voznyy, E. Yassitepe, A. Buin, S. Hoogland and E. H. Sargent, *Nature*, 2015, **523**, 324-328.

146. Y. Zhao, H. Tan, H. Yuan, Z. Yang, J. Z. Fan, J. Kim, O. Voznyy, X. Gong, L. N. Quan, C. S. Tan, J. Hofkens, D. Yu, Q. Zhao and E. H. Sargent, *Nature Commun.*, 2018, **9**, 1607.

147. S. S. Li, C. H. Chang, Y. C. Wang, C. W. Lin, D. Y. Wang, J. C. Lin, C. C. Chen, H. S. Sheu, H. C. Chia, W. R. Wu, U. S. Jeng, C. T. Liang, R. Sankar, F. C. Chou and C. W. Chen, *Enerr. & Environ. Sci.*, 2016, **9**, 1282-1289.

148. J. W. Gibbs, *Am. J. Sci.*, 1878, **s3-16**, 441-458.

149. W. Yang, R. Su, D. Luo, Q. Hu, F. Zhang, Z. Xu, Z. Wang, J. Tang, Z. Lv, X. Yang, Y. Tu, W. Zhang, H. Zhong, Q. Gong, T. P. Russell and R. Zhu, *Nano Energy*, 2020, **67**, 104189.

150. D. Zhang, Y. Zhu, L. Liu, X. Ying, C.-E. Hsiung, R. Sougrat, K. Li and Y. Han, *Science*, 2018, **359**, 675-679.

151. Y. Li, W. Zhou, Y. Li, W. Huang, Z. Zhang, G. Chen, H. Wang, G.-H. Wu, N. Rolston, R. Vila, W. Chiu and Y. Cui, *Joule*, 2019, **3**, 2854-2866.

152. M. Zhang, S. Dai, S. Chandrabose, K. Chen, K. Liu, M. Qin, X. Lu, J. M. Hodgkiss, H. Zhou and X. Zhan, *J. Am. Chem. Soc.*, 2018, **140**, 14938-14944.

153. D. Li, W. Kong, H. Zhang, D. Wang, W. Li, C. Liu, H. Chen, W. Song, F. Gao, A. Amini, B. Xu, S. Li and C. Cheng, *ACS Appl. Mater. & Interfaces*, 2020, **12**, 20103-20109.

154. S. Jeong, S. Seo, H. Yang, H. Park, S. Shin, H. Ahn, D. Lee, J. H. Park, N. G. Park and H. Shin, *Adv. Energy Mater.*, 2021, **11**, 2102236.